Universitá degli Studi Di Pisa

Dipartimento di Fisica

Corso di Laurea Magistrale
Fisica delle Interazioni Fondamentali

Development of CMB detectors to search for *B*-mode polarization in the LSPE experiment

Relatore:
Prof. Alessandro BALDINI

Candidato:
Davide VACCARO

ANNO ACCADEMICO 2014-2015

To Salvatore, Loredana, Valentina.

Contents

Look up at the stars and not down at your feet. Try to make sense of what you see, and wonder about what makes the universe exist. Be curious.

Stephen Hawking

The deepest solace lies in understanding
This ancient unseen stream
A shudder before the beautiful

Nightwish, Shudder Before the Beautiful

Chapter 1

Overview

The great advances in technology of the last decades have allowed cosmological observations to be very sensitive probes of the evolution history of the universe. A wide variety of experiments have provided measurements to test models of expansion of the universe, models of formation of the large scale structures that are currently observed, and to measure the cosmological parameters of the standard ΛCDM cosmological model, such as expansion rate, curvature, content of baryonic matter, dark matter and dark energy, as well as the nature of perturbations in the universe.

Modern cosmology is based on the cosmological principle, which states that on sufficiently large scales the universe is isotropic and homogeneous. This implies that the properties of the universe and the laws of physics have to be the same, no matter the direction of observation and the position of the observer. The cosmological principle is supported by many experimental observations, among which the Cosmic Microwave Background (CMB).

The first detection of CMB has to be traced back in 1941, when Andrew McKellar reported an average bolometric temperature of the interstellar medium of 2.3 K [1], but it was in 1964 that Penzias and Wilson detected a relic radiation in the cosmos, with a temperature of approximately 3 K [2], which was interpreted as a signature of the Big Bang.

Today we know that the CMB is a thermal radiation which follows a black-

body spectrum (see Figure 1.1) with a temperature $T = 2.7255$ K $\pm$ 0.0006 K. This radiation is interpreted as a relic of the early universe, approximately 380'000 years after the Big Bang, when the photons last scattered the electrons of the cosmic primordial plasma. Currently the key CMB observable is

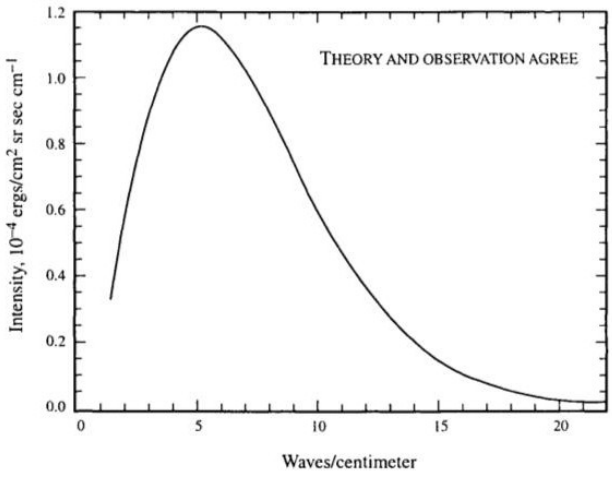

Figure 1.1: Intensity of cosmic microwave radiation as a function of wavenumber as seen by the Far InfraRed Absolute Spectrophotometer (FIRAS) [3], an instrument on the COBE satellite. The uncertainties of the experimental points are smaller than the thickness of the theoretical curve.

the angular variation in temperature and polarization correlations. The cosmological information is contained in power spectra (see Figure 1.3), defined as the Fourier transform of the two-point correlation function, as explained in Chapter 2. Precise measurements of temperature anisotropies by a variety of ground-, balloon-based and satellite experiments have led to a stunning confirmation of the ΛCDM cosmological model. In combination with other astrophysical data, the CMB anisotropy measurements place quite precise constraints on a number of cosmological parameters, and have launched us into an era of precision cosmology.

CMB anisotropies arise at a level of 10^{-5} K, over a wide range of angular scales. These anisotropies are usually expressed by using a spherical har-

monic expansion of the CMB sky:

$$T(\theta, \phi) = \sum_{l,m} a_{lm} Y_{lm}(\theta, \phi). \tag{1.1}$$

Increasing l means going to lower angular scales, requiring then higher angular resolution to measure the corresponding anisotropies.
The mean temperature of the CMB can be considered the monopole component of the expansion 1.1. The first and largest anisotropy is the dipole ($l = 1$) with amplitude of roughly 3 mK. The dipole is interpreted to be the

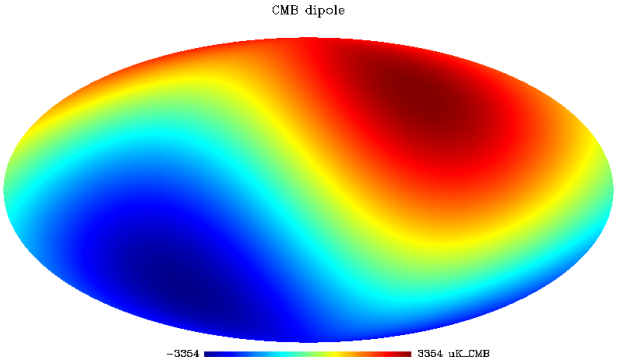

Figure 1.2: CMB dipole component ($l = 1$) as simulated in the pre-launch Planck Sky Model. [4]

result of the Doppler shift due to the Earth's motion relative to the almost perfectly isotropic blackbody radiation field. Higher multipoles temperature variations ($l \geq 2$) are interpreted as being mostly the result of perturbations in the density of the Early universe, which now we see as they were at the epoch of last scattering, when the CMB decoupled from matter.
CMB is expected to have non-zero polarization, because of the Thomson scattering processes between the electrons and photons which occurred before recombination of matter. The polarization pattern can be decomposed using the Q and U Stokes parameters [5]; however, a more intuitive and physical decomposition is the one obtained splitting the polarization pattern into a part that comes from a divergence (called $E-$mode) and a part with a curl (called $B-$mode), in analogy with the E and B fields in electrostatics.

The almost perfect isotropy and homogeneity of the CMB brings to what is known as *horizon problem*. This problem is solved postulating a period of abrupt, exponential expansion of the universe, long before the time of decoupling, so that two points in the sky which were before in causal contact, after this phase were disconnected. This period is called *inflation*. In the inflationary model, the anisotropies that we observe today in the CMB, both in temperature and polarization, are believed to be due to perturbations to the metric generated by quantum fluctuations of the inflaton field. This perturbations can be divided into *scalars* and *tensors*. Inflationary scalar perturbations give only $E-$modes, while tensors generate both $E-$modes and $B-$modes. The determination of a non-zero $B-$mode signal then is a way to measure the gravity wave contribution, which generate deriving the energy scale of inflation.

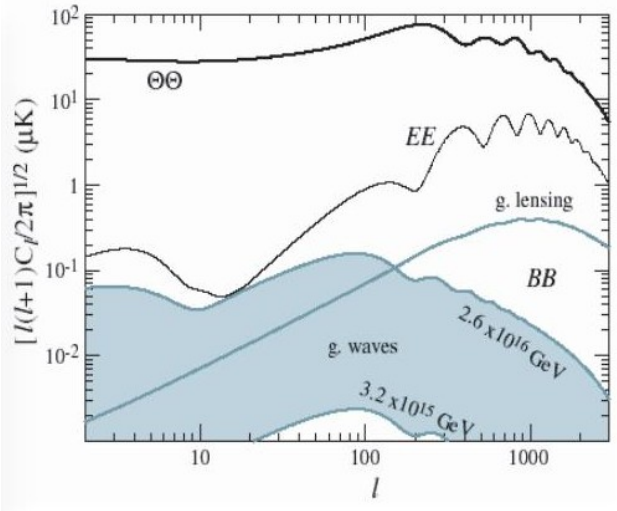

Figure 1.3: Expected scalar CMB power spectra in temperature ($\Theta\Theta$) and E-mode polarization (EE) compared with expected B-mode power spectrum (BB) due to gravitational lensing and gravitational waves. The B-mode signal is predicted using a range of inflationary energy scales. [6]

In Figure 1.3 the expected E-mode and B-mode CMB polarization signals are shown. Inflationary models predict the E-mode power spectrum to be at least one order of magnitude smaller than the power in the temperature

anisotropies power spectrum. The B-mode signal is expected to be at least one more order of magnitude smaller.

To detect such small cosmological signals the use of single detectors (such as bolometers) is not suitable, since the noise contribution achieved is comparable to or less than the expected photon noise limit, due to the discrete nature of light, approaching thus a fundamental limit. Next generation experiments can then achieve the necessary sensitivity only through large arrays of multiplexed bolometric sensors, which are nowadays the standard in this field of application.

The most promising detector technology in this field is the transition-edge sensor (TES) bolometer [7, 8]. To achieve the required sensitivity, bolometric detectors are typically operated at temperatures below 1 K. Readout of large arrays of cryogenic detectors is a major instrumental challenge. In order to reduce the wiring complexity, the cost of per-channel readout components and the heat load delivered to the coldest stages by readout wiring, the readout of these arrays is *multiplexed* [9].

There are two multiplexing techniques: time domain and frequency domain multiplexing. In time domain multiplexing (TDM), a single readout channel is sequentially switched between each member of a set of n detectors. In frequency domain multiplexing (FDM), detectors are sinusoidally biased, so that they are separated in frequency space. In this way, a single readout channel simultaneously reads n detectors.

The readout is performed using a superconducting quantum interference device (SQUID) [10], whose characteristics and performances well suit the detection system described above.

Several experiments have been performed through the decades to characterize the anisotropies of CMB. So far, $B-$mode polarization caused by primordial gravity waves has not yet been detected.

The Large Scale Polarization Explorer (LSPE) [11] is an Italian balloon-borne mission aimed at measuring the polarization of CMB at large angular scales (low l), where primordial $B-$modes are expected. To accomplish this result,

the development of multi-mode detectors, unique in Europe, is currently in progress. The launch of LSPE is forecast for 2017-2018, and its results could be the basis for a future satellite-borne mission.

This thesis is outlined in the following way:
Chapter 2 will describe in more detail how the fluctuations in the CMB can give us information about the very early universe.
Chapter 3 will discuss the state of the art of CMB experiments, in particular regarding the recent Planck [12] data release and the Large Scale Polarization Explorer (LSPE).
Chapter 4 will explain the theory of the Transition-Edge Sensor bolometer and show the results of a simulation we realized to illustrate its working principles, the expected signal and the contamination from cosmic rays.
Chapter 5 will describe the FDM technique and the R&D activity I performed, at the INFN Laboratories of Pisa and Genoa and at the NEST Laboratories in Pisa, for the development of the high-Q superconducting LC filters necessary for FDM. This Chapter also features the description of the test facility realized at the INFN Laboratories of Pisa and the result of preliminary tests of the first prototypes.
Chapter 6 will describe the principles of operation of the dc SQUID and its preliminary tests.

Further advances in cosmology strongly motivate the high efforts put in planning and building CMB polarization experiments, such as the LSPE mission described in Chapter 3. The LSPE launch is not near yet; this thesis is focused on the preliminary R&D activities for the development of the detectors, as described in the last three chapters. This kind of activity is one of the few present in Europe, the only competitor being NASA in the USA.

Chapter 2

Theory and motivations

In this Chapter a theoretical characterization of the CMB and its anisotropies is given, describing the processes which have led to their generation. Cosmological inflation is introduced as a solution to the horizon and flatness problems, followed by a more formal description of the perturbations to the smooth, uniform universe. Finally, the power spectrum of CMB temperature anisotropies will be defined, exploiting it to build the power spectrum of CMB polarization anisotropies, which will be decomposed in an "electric" irrotational component (E) and a "magnetic" curl component (B), explaining why the latter is fundamental to acquire knowledge on fundamental physics processes.

Modern cosmology is based on two observational facts: a) the universe is expanding and b) on scales larger than roughly 300 milions light years the matter distribution is homogeneous and isotropic (cosmological principle).
The strongest evidence of a universe in expansion comes from the measurements of redshifted spectral lines of atoms from distant galaxies. The shift is defined as:

$$z = \frac{\Delta\nu}{\nu} = \frac{v}{c}. \tag{2.1}$$

At first order z might be interpreted as a Doppler effect, originated by the moving away of the galaxies, with a velocity proportional to the distance, as can be seen from Figure 2.1.

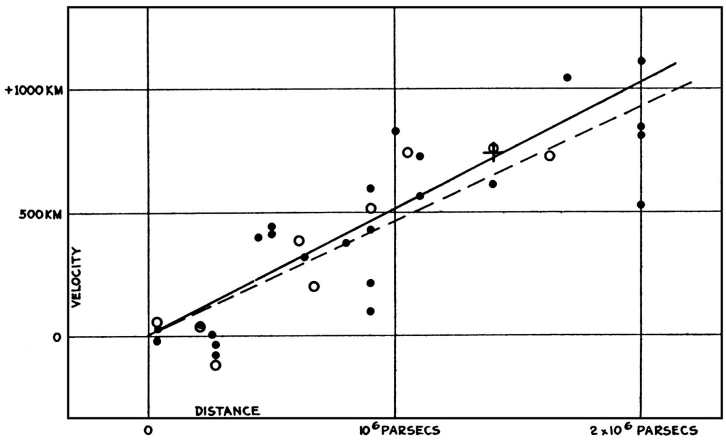

Figure 2.1: Hubble diagram, representing velocities of distant galaxies (km sec^{-1}) vs distance (Mpc). Solid (dashed) line is the best fit to the filled (open) points which are corrected (uncorrected) for the sun's motion. [13]

This is summarized by the Hubble's law:

$$v = H_0 d, \tag{2.2}$$

where H_0 is the present value of the Hubble's constant: $H_0 \simeq 70$ km s^{-1} Mpc^{-1} [5]. However, at higher order it can be seen that this redshift is due to the expansion of the universe, more than a Doppler effect, and thus the Hubble's constant depends on time.
It is useful to express this dependency as:

$$H(t) = \frac{1}{a}\frac{da}{dt} \tag{2.3}$$

where $a \equiv a(t)$ is the scale factor between physical and comoving distance, and t is the proper time of an observer in the comoving reference frame. In this way the Hubble rate $H(t)$ is a measure of how rapidly the scale factor changes, determined by measuring the velocities of distant galaxies and dividing by their distance from us.
Friedmann, Robertson and Walker derived the metric for an expanding universe with arbitrary geometry, just on the basis of the cosmological principle:

$$ds^2 = dt^2 - a^2(t)\left(\frac{1}{1-kr^2}dr^2 + r^2 d\Omega^2\right), \tag{2.4}$$

where $k = 0$, +1 and -1 for flat, positively curved and negatively curved universe, respectively. Experimental observations [14, 15] show that $k = 0$ within one part in 10^{60} (flatness problem). For a flat universe, the scale factor $a(t)$ evolves according to the Friedmann-Lemaitre equation:

$$\frac{k}{a^2} + H^2(t) = \frac{8\pi G}{3}\rho + \frac{\Lambda}{3}, \tag{2.5}$$

where ρ is the energy density appearing in the energy-momentum tensor and Λ is the cosmological constant. The Friedmann-Lemaitre equation is obtained solving the Einsten equation, which puts in relation the metric and the energy content of the universe:

$$R_{\mu\nu} - \frac{1}{2}g_{\mu\nu}R = 8\pi G T_{\mu\nu}, \tag{2.6}$$

where $R_{\mu\nu}$ is the Ricci tensor, R is the Ricci scalar, $g_{\mu\nu}$ is the metric tensor, G is the Newton's constant and $T_{\mu\nu}$ is the energy-momentum tensor. Solving the Friedmann-Lemaitre equation brings to $\rho a^3 =$ constant and $a(t) \propto t^{2/3}$ for matter domination, $\rho a^4 =$ constant and $a(t) \propto t^{1/2}$ for radiation domination, $\rho =$ constant and $a(t) \propto e^{\sqrt{\Lambda/3}t}$ for Λ domination.
These few information are essential to understand the evolution of the universe and the generation of perturbations during early times. Further details about general relativity and the Friedmann-Lemaitre equation can be found in Appendix A.

2.1 Origin of the CMB

In its early stages the universe was hot and dense, so that interactions among particles occurred at a much higher rate than today. These frequent interactions kept the various species which constituted the universe in equilibrium. As the universe expanded, interaction rates dropped down and reactions could no longer occur rapidly enough to preserve equilibrium. Out of equilibrium processes were determinant for formation of the light elements during Big Bang nucleosynthesis, recombination of electrons and protons into

neutral hydrogen and, possibly, the production of dark matter in the early universe [16]. More details on recombination of matter and decoupling of photons will be given here, since it is during these processes that anisotropies in CMB pattern were born.

2.1.1 The universe at equilibrium

Let us consider an expanding universe in thermodynamical equilibrium. The particles phase-space distribution function is:

$$f_i(p) = \left(e^{\frac{E_i-\mu_i}{T}} \pm 1\right)^{-1}, \tag{2.7}$$

where +1/-1 holds for fermions/bosons, respectively. μ_i is the chemical potential for the i-th particle and $E_i = \sqrt{\vec{p_i}^2 + m_i^2}$. It should be noted that these distributions do not depend on the position $\vec{x}$ or on the direction of the momentum, but just on its magnitude: this is a feature of the unperturbed smooth universe; when dealing with perturbations and anisotropies the dependency on $(\vec{x}, \vec{p})$ must be considered.
Let us put for sake of simplicity $\mu_i = 0$, and distinguish between relativistic species ($p \gg m$) and non-relativistic species ($p \ll m$). For the non-relativistic species, the particle number density, the energy density and the pressure can be written as ($\hbar = c = 1$):

$$n_i = g_i e^{-\frac{m_i}{T}} \left(\frac{m_i T}{2\pi}\right)^{\frac{3}{2}} \tag{2.8a}$$

$$\rho_i = m_i n_i \tag{2.8b}$$

$$P_i = T n_i. \tag{2.8c}$$

i labels different species and g_i is the degeneracy of the species (e.g. $g_\gamma = 2$, for the photon has 2 spin states). The term $e^{-\frac{m_i}{T}}$ strongly suppresses non-relativistic particle densities, which implies $P_i \ll \rho_i$.

For relativistic particles instead:

$$n_i \propto T^3 \tag{2.9a}$$

$$\rho_i \propto T^4 \tag{2.9b}$$

$$P_i \propto T^4. \tag{2.9c}$$

Here there are no suppression terms. The fundamental consequence is that if we consider the universe in thermodynamical equilibrium, what contributes to density and pressure are the relativistic species. It is also interesting to note that from (2.9b) and since $\rho \propto a^{-4}$ in radiation domination, $T \propto a^{-1}$: as one would expect, the universe cools down as it expands.
Interactions between particles are described by the Standard Model of particle physics. The interaction rate is defined as:

$$\Gamma = n\sigma v_R \tag{2.10}$$

where v_R is the relative velocity and σ is the cross section for the considered process and is calculated using the methods of the Standard Model. To see if a species is in equilibrium at a given temperature, the two quantities to be confronted are the interaction rate and the Hubble rate. A species begins to come out of equilibrium when $\Gamma \simeq H$. Going through a little math, the energy density for the relativistic species can be written as:

$$\rho = \frac{\pi^2}{30} g_{eff} T^4 \tag{2.11}$$

where g_{eff} is an effective degeneracy, given by the sum on the relativistic species at a given temperature of all their independent degrees of freedom. (2.11) is valid for bosons, for fermions there is an additional 7/8 multiplying. Hence we get, neglecting Λ and with $k = 0$ in (2.5):

$$H^2 = \frac{8}{3}\pi G\rho \rightarrow H = \sqrt{\frac{8}{90}\pi^3 G g_{eff}}\, T^2. \tag{2.12}$$

2.1.2 The Boltzmann equation

Consider an annihilation process in which two species (1 and 2) interact producing another two species (3 and 4) or vice-versa, schematically 1 +

$2 \leftrightarrow 3 + 4$. The Boltzmann equation for such a system in an expanding universe states that the rate of change in the abundance of a given particle is the difference between the rates for producing and eliminating that species:

$$a^{-3}\frac{d\left(n_1 a^3\right)}{dt} = \int \frac{d^3p_1}{\left(2\pi\right)^3 2E_1}\int \frac{d^3p_2}{\left(2\pi\right)^3 2E_2}\int \frac{d^3p_3}{\left(2\pi\right)^3 2E_3}\int \frac{d^3p_4}{\left(2\pi\right)^3 2E_4} \times (2\pi)^4\delta^3(p_1+p_2-p_3-p_4)\delta(E_1+E_2-E_3-E_4)|\mathcal{M}|^2 \times [f_3 f_4(1\pm f_1)(1\pm f_2) - f_1 f_2(1\pm f_3)(1\pm f_4)]. \quad (2.13)$$

The left side just refers to the expansion of the universe, while the interactions are included in the right side. f_i is the occupation number of the i-th species, and the $1 \pm f_i$ factor represent the Bose enhancement and Pauli blocking phenomena. The matrix element $\mathcal{M}$ for the considered process is given by the Standard Model. There are some simplifications that can be done, which make Boltzmann equation easier to solve.

The first simplification comes since we are interested in systems at a temperature smaller than $E - \mu$, so that the exponential in (2.7) dominates on the ± 1 and the Bose enhancement and Pauli blocking terms in (2.13) are negligible. By virtue of this, the last line in (2.13) becomes:

$$e^{-\frac{E_1+E_2}{T}}\left[e^{\frac{\mu_3+\mu_4}{T}} - e^{\frac{\mu_1+\mu_2}{T}}\right]. \quad (2.14)$$

The number density at a generic time for the i-th species is:

$$n_i = g_i e^{\frac{\mu_i}{T}}\int \frac{d^3p}{(2\pi)^3}e^{-\frac{E_i}{T}} \quad (2.15)$$

so that $e^{\mu_i/T} = n_i/n_i^{eq}$, where n_i^{eq} are the number densities at equilibrium derived in the previous subsection. The last line in (2.13) can be again rewritten as:

$$e^{-\frac{E_1+E_2}{T}}\left[\frac{n_3 n_4}{n_3^{eq} n_4^{eq}} - \frac{n_1 n_2}{n_1^{eq} n_2^{eq}}\right]. \quad (2.16)$$

If we define the thermally averaged cross section:

$$\langle\sigma v\rangle = \frac{1}{n_1^{eq} n_2^{eq}}\int \frac{d^3p_1}{\left(2\pi\right)^3 2E_1}\int \frac{d^3p_2}{\left(2\pi\right)^3 2E_2}\int \frac{d^3p_3}{\left(2\pi\right)^3 2E_3}\int \frac{d^3p_4}{\left(2\pi\right)^3 2E_4}e^{-\frac{E_1+E_2}{T}} \times (2\pi)^4\delta^3(p_1+p_2-p_3-p_4)\delta(E_1+E_2-E_3-E_4)|\mathcal{M}|^2 \quad (2.17)$$

the Boltzmann equation greatly simplifies to the form:

$$a^{-3}\frac{d\left(n_1 a^3\right)}{dt} = n_1^{eq} n_2^{eq} \langle \sigma v \rangle \left[\frac{n_3 n_4}{n_3^{eq} n_4^{eq}} - \frac{n_1 n_2}{n_1^{eq} n_2^{eq}} \right]. \tag{2.18}$$

It is interesting to note that the left side is of the order of $n_1 H$, while the left side is of the order of $n_1 \Gamma$. At equilibrium $\Gamma \gg H$, so the terms on the right side are much larger than the one on the left. It follows then that at equilibrium:

$$\frac{n_1^{eq} n_2^{eq}}{n_3^{eq} n_4^{eq}} = \frac{n_1 n_2}{n_3 n_4}. \tag{2.19}$$

2.1.3 Decoupling of photons

Before matter recombination, photons are coupled to electrons via Thomson scattering (see the Feynman dyagram sketched in Figure 2.2). Neutral hydrogen formation occurs via the reaction $e^- + p \leftrightarrow H + \gamma$, but only when the temperature lowers well below the binding energy of neutral hydrogen ($\epsilon_0 = 13.6$ eV) effective recombination is possible. In case of thermal equi-

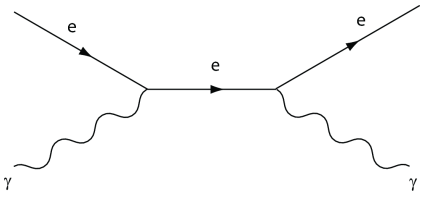

Figure 2.2: Feynman dyagram for Thomson scattering of photons.

librium, the electron density is:

$$n_e = g_e \left(\frac{m_e T}{2\pi} \right)^{-\frac{3}{2}} e^{-\frac{m_e}{T}}. \tag{2.20}$$

n_p and n_H are calculated in the same way. Note that since the chemical potential for photons is zero, it follows that $n_\gamma = n_\gamma^{eq}$. (2.19) then ensures that:

$$\frac{n_e n_p}{n_H} = \frac{n_e^{eq} n_p^{eq}}{n_H^{eq}}. \tag{2.21}$$

The neutrality of the universe ensures $n_e = n_p$. We define the free electron fraction:

$$X_e = \frac{n_e}{n_e + n_H} = \frac{n_p}{n_p + n_H} = \frac{n_p}{n_B} \tag{2.22}$$

where n_B is the baryonic density. Substituting the appropriate number density expressions in (2.19) and performing the integrals, we obtain:

$$\frac{X_e^2}{1 - X_e} = \frac{1}{n_B} \left(\frac{m_e T}{2\pi} \right)^{3/2} e^{-\epsilon_0 / T}, \tag{2.23}$$

which is known as Saha equation. When $T \simeq \epsilon_0$ the right side is very large, so that the the denominator on the left side is very small, that is $X_e \simeq 1$: all the hydrogen is ionized. Recombination takes place only when $T \ll \epsilon_0$. The Saha equation is no longer valid out of equilibrium, so the Boltzmann equation must be solved. Substituting the quantities we are dealing with, (2.18) becomes:

$$a^{-3} \frac{d\left(n_e a^3\right)}{dt} = n_B \langle \sigma v \rangle \left[(1 - X_e) \left(\frac{m_e T}{2\pi} \right)^{3/2} e^{-\epsilon_0 / T} - X_e^2 n_B \right]. \tag{2.24}$$

Since $n_B a^3$ is constant it can be passed through the derivative on the left after expressing n_e as $n_B X_e$, so that (2.24) is rewritten as:

$$\frac{dX_e}{dt} = (1 - X_e)\mathcal{I} - X_e^2 n_B \mathcal{R} \tag{2.25}$$

where $\mathcal{I}$ and $\mathcal{R}$ are the ionization and recombination rate, respectively:

$$\mathcal{I} = \langle \sigma v \rangle \left(\frac{m_e T}{2\pi} \right)^{3/2} e^{-\epsilon_0 / T} \tag{2.26a}$$

$$\mathcal{R} = \langle \sigma v \rangle. \tag{2.26b}$$

Results for the Saha equation and numerical integration of the Boltzmann equation (2.25) are shown in Figure 2.3. The Thomson scattering rate is:

$$\Gamma = n_e \sigma_T v_R = X_e n_B \sigma_T v_R, \tag{2.27}$$

where σ_T is the Thomson scattering cross section. Decoupling occurs at $z \simeq 1100$, when $t_{decoupling} \simeq 10^5$ years.

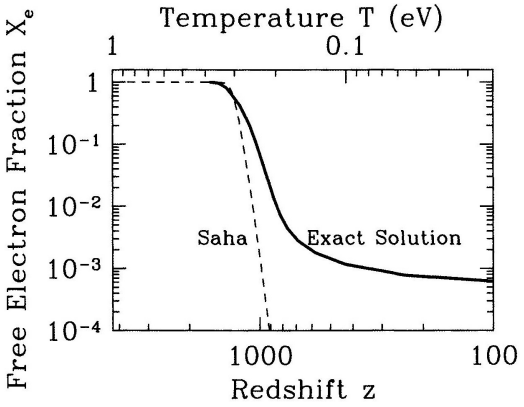

Figure 2.3: Free electron fraction as a function of redshift. Recombination takes place at z $\simeq$ 1100, or T $\simeq$ 0.25 eV. As can be seen, Saha equation holds at equilibrium, but not after recombination. [16]

2.2 Cosmological inflation

2.2.1 The horizon problem

Before discussing the origin of the anisotropies in the CMB, it is worth to introduce the paradigm of inflation. Cosmological inflation was introduced in the '80s [17] to solve fundamental problems that were debated since the late '60s. In particular, the uniformity and isotropy of the CMB brings to the problem known as the horizon problem.
To understand the nature of the horizon problem, a more formal description of the propagation of light in the expanding universe is needed. It is useful to define the conformal time:

$$d\eta = \frac{dt}{a(t)}. \tag{2.28}$$

Like in Minkowski space, the null geodesics of a photon is a straight line at $\pm 45°$ angles in the $\eta - r$ plane. The maximal distance a photon can travel between two istants of time t_1 and t_2 is:

$$\Delta r = \Delta\eta = \int_{t_1}^{t_2} \frac{dt}{a(t)} \tag{2.29}$$

and is called *comoving horizon*. The comoving horizon at recombination and the comoving horizon of a photon from recombination to the present days are then:

$$\eta_{ric} = \int_0^{t_{ric}} \frac{dt}{a(t)} \tag{2.30a}$$

$$\eta_0 = \int_{t_{ric}}^{t_0} \frac{dt}{a(t)}. \tag{2.30b}$$

The angle subtended by a causal connecting region can therefore be estimated as:

$$\theta_{hor} \simeq \frac{\eta_{ric}}{\eta_0}. \tag{2.31}$$

Assuming a flat, matter-dominated universe ($a(t) \propto t^{2/3}$) and knowing that $z_{ric} \simeq 1100$:

$$\theta_{hor} = \frac{\eta_{ric}}{\eta_0} = \left(\frac{t_{ric}}{t_0}\right)^{1/3} = \left(\frac{a_{ric}}{a_0}\right)^{1/2} = \frac{1}{\sqrt{z_{ric}}} \simeq 2^\circ \tag{2.32}$$

This is the horizon problem: two points in the sky separated by an angular distance greater than 2° could have never been in causal contact (see Figure 2.4). But then, CMB should not be homogeneous and isotropic (within a 10^{-5} level) as it is observed.

2.2.2 The solution

(2.28) can be rewritten in the form:

$$d\eta = (aH)^{-1} d\ln a. \tag{2.33}$$

The elapsed conformal time depends on the evolution of the *comoving Hubble radius* $(aH)^{-1}$. For (2.12) and (A.20):

$$(aH)^{-1} \propto a^{\frac{1}{2}(1+3\alpha)}, \tag{2.34}$$

with $\alpha = 0$ for matter domination or 1/3 for radiation domination (see Appendix A). It follows that the Hubble radius increases as the universe expands.

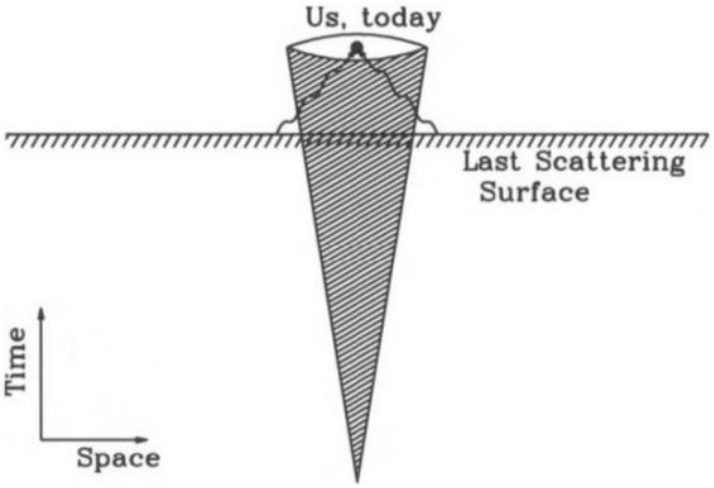

Figure 2.4: The horizon problem. The region inside the cone at any time is causally connected to us (at the center). Photons emitted from the last scattering surface ($z \sim 1100$) started outside of this region. Therefore, at the last scattering surface, they were not in causal contact with each other. Yet their temperature are almost identical. [16]

A simple solution to the horizon problem therefore is conjecturing a phase of decreasing Hubble radius, long before the time of recombination, so that $\eta_{ric} > \eta_0$. The condition for this to happen is $\alpha < -1/3$; for (A.16) it follows that during this phase the pressure is negative. Since conventional energy sources do not satisfy this condition, this means that during this phase a new form of energy must dominate. It can be shown that such a solution solves as well the flatness problem [18]. Requiring a phase in which:

$$\frac{d}{dt}(aH)^{-1} < 0 \tag{2.35}$$

is equivalent to requiring a period of accelerating expansion of the universe:

$$\frac{d}{dt}(aH)^{-1} = \frac{d}{dt}(\dot{a})^{-1} = -\frac{\ddot{a}}{(\dot{a})^2} < 0 \;\rightarrow\; \ddot{a} > 0. \tag{2.36}$$

This period is called inflation.

Figure 2.5 shows the evolution of the Hubble radius: during inflation the distance within which photons can communicate with each other dramatically

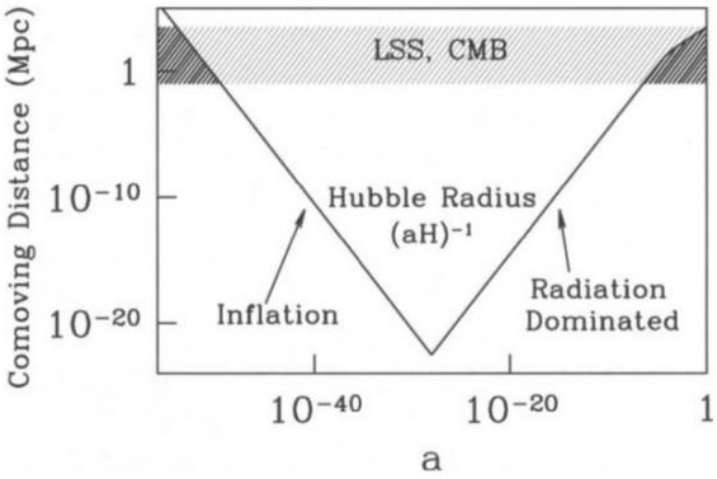

Figure 2.5: The comoving Hubble radius as a function of the scale factor (logarithmic scale). Scales of cosmological interest (shaded band) were larger than the Hubble radius until $a \sim 10^{-5}$. Dark shaded regions show when these scales were smaller than the Hubble radius, and therefore susceptible to causal physics. Very early on, before inflation operated, all scales of interest were smaller than the Hubble radius. Similarly, at very late times, scales of cosmological interest came back within the Hubble radius. [16]

decreases. Before inflation started, the Hubble radius was very large, so that all scales of cosmological interest were well within the comoving horizon. The symmetry of Figure 2.5 tells us that the perturbations we see and measure today are the same of when they first left the horizon during the inflationary epoch. To explain the structure of the universe today it is then important to understand the generation of perturbations during inflation.

With inflation, the situation of Figure 2.4 changes to the one depicted in Figure 2.6. The time at which inflation ends is called *reheating*: the large potential energy of the inflaton field decays into particles and fills the universe with Standard Model particles. The comoving horizon ceases to be an effective time parameter after reheating, because becomes very large during inflation and from the time of reheating it changes very little. The conformal

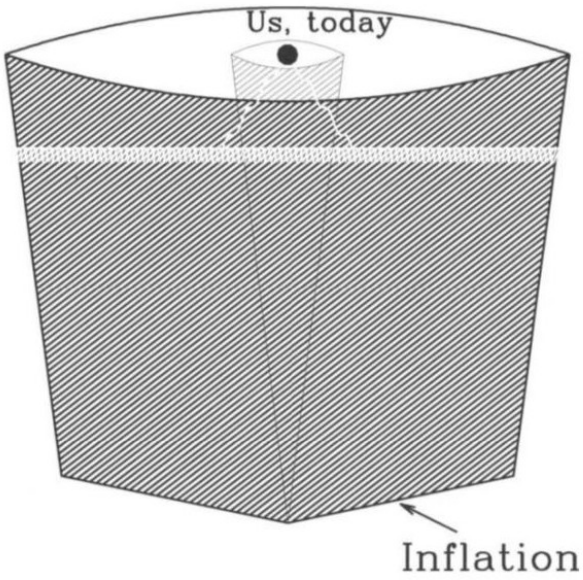

Figure 2.6: Inflationary solution to the horizon problem. Larger cone shows the true horizon in an inflationary model; smaller inner cone shows the horizon without inflation. During inflation, the physical horizon blows up very rapidly. All scales in the shaded region were once in causal contact so it not surprising that the temperature is uniform. [16]

time is then redefined as:

$$\eta = \int_{t_{reheating}}^{t} \frac{dt'}{a(t')}, \tag{2.37}$$

subtracting the primordial part, so that the total comoving horizon is $\eta_{prim} + \eta$. This redefinition means that, before the reheating, η is negative.
In the course of time many inflationary models have been proposed. A simple inflationary model, called slow-roll inflation, is described in Appendix B.

2.3 Perturbations

2.3.1 Boltzmann equation for photons

Characterizing the anisotropies in the distribution of photons is not an easy task, since photons are coupled to electrons via Thomson scattering and af-

fected by gravity, which in turn affects and is affected by all species present in the universe at decoupling (including neutrinos and dark matter). Boltzmann equation allows us to account for all of these couplings, although now we are not just interested in the integrated number density, as in subsection 2.1, but in the full distribution of photons, as a function of momentum.
The non-integrated Boltzmann equation takes the form:

$$\frac{df}{dt} = C[f], \tag{2.38}$$

where f is the photon phase-space distribution function.
The right-hand side of (2.38) contains all possible collision terms, which are complicated functionals of the distribution of photons. Writing down the explicit Boltzmann equation for photons and solving it is very time-taking and requires a lot of mathematics. For the complete calculations please refer to [16].
First, we must account for perturbations. An important theorem, called *decomposition theorem*, states that perturbations to the metric can be divided into scalar, vector and tensor, and each type evolves independently. This means that if some physical process in the early universe generates tensor perturbations, they don't induce scalar perturbations, and vice versa. Inflation generates tensor perturbations (gravity waves) to the metric. Later is shown that these leave their footprint in the polarization pattern of the CMB. For now let us consider only scalar perturbations.
The perturbed universe is described adding to the scale factor $a(t)$ two more functions, Ψ and Φ, which depend on space and time. The metric then becomes:

$$\begin{aligned} g_{00}(\vec{x},t) &= -1 - 2\Psi(\vec{x},t) \\ g_{0i}(\vec{x},t) &= 0 \\ g_{ij}(\vec{x},t) &= a^2\delta_{ij}(1 + 2\Phi(\vec{x},t)). \end{aligned} \tag{2.39}$$

The perturbations to the metric are Ψ, which corresponds to the Newtonian potential, and Φ, the perturbation to the spatial curvature. When they are zero, (2.39) reduces to the unperturbed FRW metric. Since the perturbations

in the universe are small at the times and scales of interest (i.e. during inflation), Ψ and Φ can be treated as small quantities, dropping all quadratic terms. The form (2.39) corresponds to a choice of *gauge* (called *conformal Newtonian gauge*).

The photon distribution function f can be expanded around its Bose-Einstein value. At first order:

$$f(\vec{x}, p, \hat{p}, t) = \left[\exp\left(\frac{p}{T(t)[1 + \Theta(\vec{x}, \hat{p}, t)]}\right) - 1\right]^{-1}. \tag{2.40}$$

The zero-order temperature T is a function of time only. $\Theta \equiv \delta T/T$ is the perturbation to the distribution function, whose dependency from $\vec{x}$ and $\hat{p}$ describes, respectively, inhomogeneities and anisotropies in the photon distribution. The absence of a p dependency follows from the fact that the magnitude of the photon momentum is virtually unchanged during a Thomson scattering. After some lengthy passages, it can be shown that (2.38) for photons becomes:

$$\dot{\Theta} + \hat{p}^i \frac{\partial \Theta}{\partial x^i} + \dot{\Phi} + \hat{p}^i \frac{\partial \Psi}{\partial x^i} = n_e \sigma_T a[\Theta_0 - \Theta + \hat{p} \cdot \vec{v}_b], \tag{2.41}$$

where n_e is the electron number density, σ_T is the Thomson cross section, v_b is the bulk electron velocity and Θ_0 is the monopole component of the perturbation to the temperature field (the multipole expansion of the temperature field is defined later on). Here and from now on, overdots represent derivatives with respect to conformal time.

In deducing (2.41), the dependence on the polarization of the incoming and outgoing photons during the Thomson scattering is neglected. This dependence is what causes the imprinting of perturbations in the polarization field, which is also coupled to the temperature anisotropies. The calculations can be simplified neglecting the dependency of the amplitude squared from the polarization and from the angle between the incident and outgoing photon. This simplification, although wrong, allows to describe the temperature anisotropies with good precision, momentarily neglecting polarization.

(2.41) is a partial differential linear equation coupling Θ to Φ, Ψ and $\vec{v}_b$. If we

Fourier transform these variables (so $\partial/\partial x^i \to k_i \equiv k^i$), the resulting Fourier amplitudes obey ordinary differential equations, which are simpler to solve. Moreover, since perturbations are small (i.e. we stopped at first order in the expansion) the equations are linear. This means that each Fourier mode evolves independently: Fourier transforming (2.41) produces a set of uncoupled differential equations for the Fourier modes. The Fourier convention used is:

$$\Theta(\vec{x}) = \int \frac{d^3k}{(2\pi)^3} e^{i\vec{k}\cdot\vec{x}} \tilde{\Theta}(\vec{k}). \tag{2.42}$$

A Fourier mode can be characterized by the magnitude of its wavevector: $k = \sqrt{k_i k^i}$. We define two other useful quantities. The first one is the following:

$$\mu = \frac{\vec{k}\cdot\hat{p}}{k}, \tag{2.43}$$

the cosine of the angle between the wavevector $\vec{k}$ of the perturbation and the photon direction $\hat{p}$. From now on, μ will be used to describe the direction of photon propagation. When $\mu = 1$ the photon direction is aligned with $\hat{k}$, so the photon is travelling in the direction along which the temperature is changing. A photon travelling in a direction in which the temperature remains the same has $\mu = 0$. The second useful quantity is:

$$\tau(\eta) = \int_{\eta}^{\eta_0} d\eta' n_e \sigma_T a, \tag{2.44}$$

the optical depth. We call the Fourier transform of the temperature perturbation $\Theta(k, \mu, \eta)$ (for simplicity of notation we omit the tilde symbols). It is in general useful to perform a multipole expansion of this quantity. The lth multipole is defined as:

$$\Theta_l(k, \eta) = \frac{1}{(-i)^2} \int_{-1}^{1} \frac{d\mu}{2} \mathcal{P}_l(\mu) \Theta(k, \mu, \eta), \tag{2.45}$$

where $\mathcal{P}_l$ is the Legendre polynomial of order l. The monopole corresponds to $l = 0$, the dipole to $l = 1$, the quadrupole to $l = 2$ and so on. The higher Legendre polynomials have structure on smaller scales, so the higher

moments capture information about the small scale structure of the field. With these definitions, (2.41) becomes:

$$\dot{\Theta} + ik\mu\Theta + \dot{\Phi} + ik\mu\Psi = -\dot{\tau}[\Theta_0 - \Theta + \mu v_b]. \tag{2.46}$$

The equations which rule the evolution of Ψ and Φ are found solving the perturbed Einstein equation, and are [16]:

$$k^2\Phi + 3\frac{\dot{a}}{a}\left(\dot{\Phi} - \Psi\frac{\dot{a}}{a}\right) = 4\pi G a^2[\rho_{dm}\delta + \rho_b\delta_b + 4\rho_\gamma\Theta_0 + 4\rho_\nu\mathcal{N}_0] \tag{2.47a}$$

$$k^2(\Phi + \Psi) = -32\pi G a^2[\rho_\gamma\Theta_2 + \rho_\nu\mathcal{N}_2]. \tag{2.47b}$$

ρ_{dm}, ρ_b, ρ_ν, ρ_γ are the energy density of, respectively, dark matter, baryons, neutrinos and photons; δ and δ_b are the density perturbations of dark matter and baryons, respectively; Θ_0 and $\mathcal{N}_0$ the monopole moment of, respectively, photons and neutrinos distributions; Θ_2 and $\mathcal{N}_2$ the quadrupole moment of, respectively, photons and neutrinos distribution.
The solution for (2.46), which describes the anisotropies today, is [16]:

$$\begin{aligned}\Theta_l(k,\eta_0) \simeq\ & [\Theta_0(k,\eta_*) + \Psi(k,\eta_*)]j_l[k(\eta_0 - \eta_*)] \\ & + 3\Theta_1(k,\eta_*)\left(j_{l-1}[k(\eta_0 - \eta_*)] - \frac{(l+1)j_l[k(\eta_0 - \eta_*)]}{k(\eta_0 - \eta_*)}\right) \\ & + \int_0^{\eta_0} d\eta e^{-\tau}[\dot{\Psi}(k,\eta) - \dot{\Phi}(k,\eta)]j_l[k(\eta_0 - \eta)].\end{aligned} \tag{2.48}$$

η_* is the conformal time of recombination, η_0 is the conformal time of present. This equation is the basis for semianalytic calculations of power spectra which agree with the exact (numerical) solutions to within 10%. We are going to define power spectra in a little. We see that, to solve for the anisotropies today, we must know the monopole Θ_0, dipole Θ_1 and potential Ψ at the time of recombination. If Ψ and Φ are time dependent there will be small corrections, encoded in the last line of (2.48). These corrections are due to the so-called *integrated Sachs-Wolfe effect* (ISW). This effect will be described later. The spherical Bessel function $j_l[k(\eta_0 - \eta_*)]$ in the first term of (2.48) determines how much anisotropy on a scale l is contributed by a plane wave

with wavenumber k. In particular, it can be shown that a perturbation with wavenumber k contributes predominantly on angular scales of order $l \sim k\eta_0$.

2.3.2 Acoustic oscillations

The equation governing perturbations in the primordial baryon-photon fluid is deduced from 2.46 in the tightly coupled limit ($\Gamma \gg H$) and can be written in the form [16]:

$$\ddot{\Theta}_0 + k^2 c_s^2 \Theta_0 = F, \tag{2.49}$$

where F is a force of gravitational attraction and c_s is the sound speed of the baryon-photon fluid. This is the equation of a forced harmonic oscillator: before recombination the amplitude of the perturbations oscillates according to (2.49). This phenomenon is due to the radiation pressure provided by the photons opposing the gravitational tendency to collapse of the baryons, and is the cause of the acoustic peaks appearing in the power spectrum of Figure 2.8, which will be defined later on.

It is interesting to note that these oscillations occur only for small-scale modes (i.e., modes whose wavelength k^{-1} is smaller than the horizon at recombination). Large-scale mode do not evolve and remain unchanged, since no causal physics can affect perturbations with wavelengths larger than the horizon. This means that when we observe large-scale anisotropies, which are sensitive to modes with wavelengths larger than the horizon at recombination, we are observing perturbations in their most pristine form, as they were created presumably during inflation.

From the calculations it emerges that not only the monopole Θ_0 is subject to acoustic oscillations, but also the dipole Θ_1, completely out of phase with Θ_0. All higher moments ($l \geq 2$) are damped out and do not oscillate.

Until now we considered only scalar perturbations. Since inflation generates tensor perturbations to the metric, we must characterize them before discussing the solution to the Boltzmann equation for photons. Vector perturbations instead rapidly decay as the universe expands.

2.3.3 Primordial gravity waves

Tensor perturbations to the metric are detectable because they produce observable distortions in the CMB, especially at large angular scales, and it is possible to consider them separately from scalar perturbations because, as previously said, for the decomposition theorem they are decoupled.
Tensor perturbations can be characterized by the metric:

$$\begin{aligned} g_{00} &= -1 \\ g_{0i} &= 0 \\ g_{ij} &= a^2 \mathcal{H}_{ij} \end{aligned} \tag{2.50}$$

where:

$$\mathcal{H}_{ij} = \begin{pmatrix} 1+h_+ & h_\times & 0 \\ h_\times & 1-h_+ & 0 \\ 0 & 0 & 1 \end{pmatrix}. \tag{2.51}$$

The perturbations are then described by the two functions h_+ and $h_\times$, assumed to be small. The z-axis is chosen as the direction of the wavevector $\vec{k}$. Writing down and solving the tensor-perturbated Einstein equation leads to:

$$\ddot{h}_{+,\times} + 2\frac{\dot{a}}{a}\dot{h}_{+,\times} + k^2 h_{+,\times} = 0. \tag{2.52}$$

(2.52) is a wave equation, generalized to an expanding universe, which has gravity waves as solutions. Neglecting the expansion of the universe, so that the damping term in (2.52) vanishes, the perturbation to the metric in real space is of the form:

$$h_{+,\times}(\vec{x},\eta) = \int d^3k e^{i\vec{k}\cdot\vec{x}}[Ae^{ik\eta} + Be^{-ik\eta}]. \tag{2.53}$$

The two modes correspond to waves travelling in the $\pm\hat{z}$ direction at the speed of light. If the expansion of the universe is considered, the solutions are still oscillatory, but damped. For a mode of wavevector $\vec{k}$, the condition for being out of the comoving horizon can be expressed by:

$$k\eta \ll 1, \tag{2.54}$$

which means that no causal physics can affect it. When $k\eta \simeq 1$, the mode begins to enter the horizon (decays), being affected by causal physics and is soon damped. This is seen in Figure 2.7, which shows the evolution of gravity waves of three different modes. The large scale mode ($k\eta_0 = 10$)

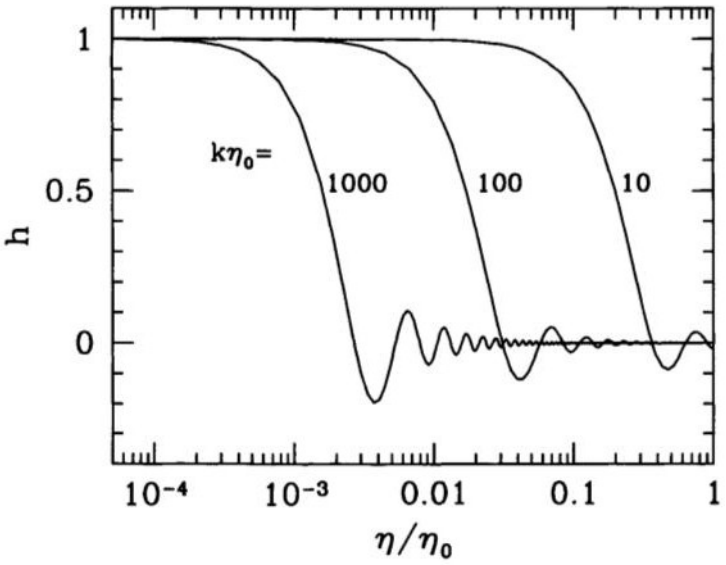

Figure 2.7: Evolution of gravity waves as a function of conformal time. Three different modes are shown, labeled by their wave numbers. Smaller scale modes decay earlier. [16]

remains constant until early times, when its wavelength is larger than the horizon. Once its wavelength becomes comparable to the horizon, the amplitude begins to die off, oscillating several times until the present. The small scale mode $k\eta_0 = 1000$ also begins to decay when its wavelength becomes comparable to the horizon. Its entry into the horizon occurs much earlier, though, so the damping is much more efficient. By today, the amplitude is extremely small. Figure 2.10 then tells us that only modes with $k\eta_0 \lesssim 100$ persist, and all smaller scale modes can be neglected. Therefore, anisotropies on small angular scales are not be affected by gravity waves, but only large scale anisotropies are.

2.3.4 Temperature anisotropies

The temperature field in the universe can be written as:

$$T(\vec{x},\hat{p},\eta) = T(\eta)[1+\Theta(\vec{x},\hat{p},\eta)]. \tag{2.55}$$

Since we can only observe this field here ($\vec{x}_0$) and now (η_0), we can evaluate the anisotropies just on their dependence on the direction of the incoming photons ($\hat{p}$). Observations are reported on maps, wherein the temperature is reported as a function of the direction $\hat{p}$. More precisely, what is used are not the $\hat{p}_x$, $\hat{p}_y$, $\hat{p}_z$ components, but rather polar (galactic) coordinates. However for now we will keep using $\hat{p}$. The field can be expanded in spherical harmonics:

$$\Theta(\vec{x},\hat{p},\eta) = \sum_{l=1}^{\infty}\sum_{m=-l}^{l} a_{lm}(\vec{x},\eta)Y_{lm}(\hat{p}). \tag{2.56}$$

All of the information contained in the temperature field T is also contained in the space-time dependent amplitudes a_{lm}, which are the observables. The Y_{lm}'s are normalized via:

$$\int d\Omega\ Y_{lm}(\hat{p})\ Y^*_{l'm'}(\hat{p}) = \delta_{ll'}\delta_{mm'}, \tag{2.57}$$

where $d\Omega$ is the solid angle spanned by $\hat{p}$. Multiplying both sides of (2.57) by $Y^*_{lm}(\hat{p})$ and integrating we obtain:

$$a_{lm}(\vec{x},\eta) = \int \frac{d^3k}{(2\pi)^3} e^{i\vec{k}\cdot\vec{x}} \int d\Omega\ Y^*_{lm}(\hat{p})\Theta(\vec{k},\hat{p},\eta), \tag{2.58}$$

where the right-hand side is written in terms of $\Theta(\vec{k},\hat{p},\eta)$, the Fourier transform of $\Theta(\vec{x},\hat{p},\eta)$. We cannot make predictions on the a_{lm}, but just on their distribution, supposed to be Gaussian. The mean value of each a_{lm} is zero, but their variance will be non-zero. This variance is called C_l. So:

$$\begin{aligned} \langle a_{lm}\rangle &= 0 \\ \langle a_{lm}a^*_{l'm'}\rangle &= \delta_{ll'}\delta_{mm'}C_l. \end{aligned} \tag{2.59}$$

For a given l, each a_{lm} has the same variance, so when measuring all its $(2l+1)$ coefficients we are sampling its distribution. The drawback is that at

large scales, e.g the quadrupole $l = 2$, we do not get much information about the underlying variance, C_2. Therefore, there is a fundamental uncertainty in the knowledge on the C_l. This uncertainty is most pronounced at low l and is called *cosmic variance*. Given any two observables X and Y, the quantity C_l^{XY} is defined as:

$$C_l^{XY} = \frac{1}{2l+1} \sum_m \langle a^*_{X,lm} a_{Y,lm} \rangle. \tag{2.60}$$

C_l^{XY} is called angular power spectrum, and is the Fourier transform of the two-point correlation function of the quantities X and Y. Let's put for now $X = Y = T$, where T means temperature. It can be shown that C_l^{TT} depends on $\Theta_l(k)$ by the following relation [16]:

$$C_l^{TT} = \frac{2}{\pi} \int_0^\infty dk \; k^2 P(k) \left| \frac{\Theta_l(k)}{\delta(k)} \right|^2, \tag{2.61}$$

where $P(k)$ is the power spectrum of matter and $\delta(k)$ is the dark matter density perturbation. (2.48) and (2.61) are the equations used to plot the theoretical anisotropy spectrum today.

2.3.5 The power spectrum

In Figure 2.8 the theoretical CMB anisotropy power spectrum is shown. We can see that in the region called Sachs-Wolfe Plateau ($l \lesssim 100$) anisotropies have not evolved significantly, because the perturbations responsible for these anisotropies were on scales far larger than those that could be connected via causal processes at the time of recombination. At these scales, only the monopole contributes to the anisotropy, i.e. the first term in (2.48). The name of this region of the power spectrum derives from the people who first computed the large-angle anisotropy [20].

For $100 \lesssim l \lesssim 1000$ the anisotropy spectrum depends also on the dipole and the ISW effect (second and third term in (2.48)). The perturbations at these smaller scales are affected by causal physics, so that the photon-baryon fluid was subject to acoustic oscillations, with the photons providing most of the

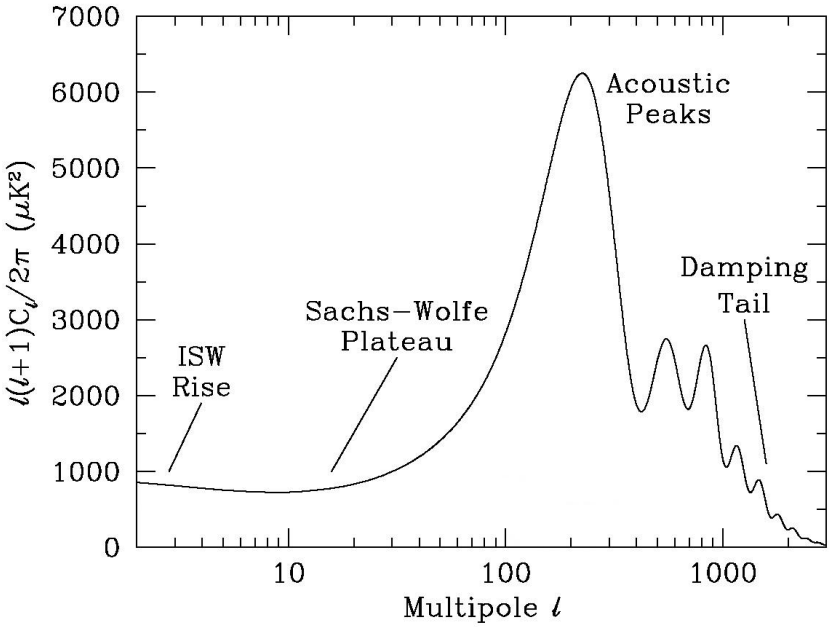

Figure 2.8: Plot of the theoretical CMB anisotropy power spectrum, using a standard ΛCDM model in the CMBFAST software. [19]

pressure and the baryons the inertia.

For $l \gtrsim 1000$ the power spectrum presents a damping tail. This is due to the recombination process not being instantaneous, giving a finite thickness to the last scattering surface and dumping the perturbations at scales smaller than that subtended by this thickness.

The shape of the region at largest angular scales (ISW Rise) is due to integrated Sachs-Wolfe effect (ISW) and reionization contributions. The Sachs-Wolfe effect is a property of the CMB, for which photons are redshifted when moving through gravitational potentials. ISW happens between η_{rec} and η_0 and is due to residual radiation after recombination: it occurs because the transition from radiation domination to matter domination is not instantaneous. This effect causes perturbations corresponding to scales l comparable with the ratio η_0/η_{rec} to get a boost. There is also a late-time ISW effect, due to the dark energy starting to govern the expansion of the universe.

The reionization effect is expected to happen at $z \backsim 6$ [21]. Reionisation

is caused by the formation of the first galaxies, bringing the CMB photons back in contact with the electrons of the ionized hydrogen atoms. During reionization the electron density is much lower than before recombination because of the expansion of the universe, therefore Thomson scattering occurs at a much lower rate when the universe is again somewhat opaque to photons. If the photons hit a region with optical depth τ, only a fraction $e^{-\tau}$ will escape without scattering. Since this is true only for those scales within the horizon at the time of reionization, only multipoles l larger than η_0/η_{reion} will be suppressed by $e^{-\tau}$. Small l, or equivalently large scales, will be unaffected. Due to Thomson scattering, polarization anisotropies at large scales are induced during reionization (see Section 2.4). This causes a bump in the B-modes theoretical power spectrum at low l (see again Figure 1.3), because tensor perturbations which are inside horizon and are not damped (like in Figure 2.7) affect again the polarization of the photons scattered during reionization, promoting B-modes generation, as explained in the next section.

2.4 Polarization

2.4.1 Thomson scattering

CMB radiation is expected to be polarized because of Thomson scattering at the time of decoupling. As it is known, light travelling in a direction (say $\hat{x}$-direction) corresponds to electric and magnetic fields oscillating in the y-z plane, transverse to the direction of propagation. Thomson scattering allows all transverse radiation to pass through unimpeded, while stopping the radiation parallel to the direction of propagation. Of course radiation gets scattered into all directions with varying probability, which must be taken into account. Figures 2.9 and 2.10, even if in a very simplified way, make clear that to produce polarized radiation the incoming radiation must have a non-zero quadrupole.

Polarizazion can be depicted as a headless vector, with a length corresponding

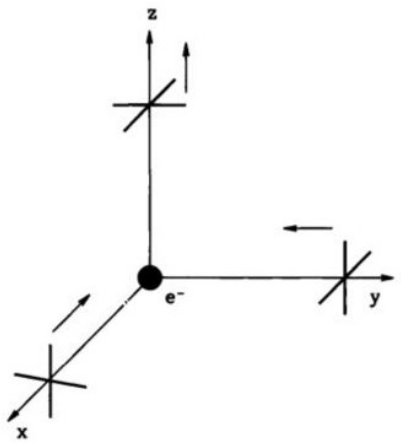

Figure 2.9: Incoming isotropic radiation produces no polarization. Here, since the incoming amplitudes from the $\hat{x}$ and $\hat{y}$ directions are equal, the outgoing intensities along both of these directions are equal, leading to unpolarized radiation. [16]

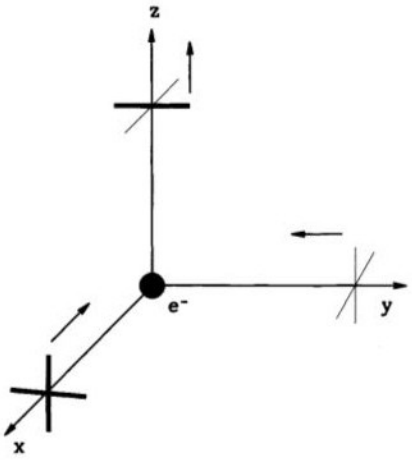

Figure 2.10: Incoming quadrupole radiation produces outgoing polarized light. The outgoing radiation has greater intensity along the y-axis than in the x-axis. This is a direct result of the hotter radiation incident from the $\hat{x}$ direction. [16]

to its magnitude and the orientation of the line describing the axis along which the intensity is greatest. In the 2D plane perpendicular to the direction

of propagation, the intensity of the radiation can be decomposed as:

$$I_{ij} = \begin{pmatrix} T+Q & U \\ U & T-Q \end{pmatrix}. \tag{2.62}$$

T is the temperature, which is composed, as previously seen, by a uniform part and a perturbation Θ. Q and U describe the polarization. T, Q and U are the Stokes parameters [5]. The Stokes parameters must be related to a quantity which describes the anisotropies in the polarization of the CMB, just like Θ_l does for the temperature anisotropies. To do so, we have to reconsider polarization in the calculations which led to (2.46). Doing so, calling Θ_P the quantity describing the polarization anisotropies, brings us to the Boltzmann equation for the polarization anisotropies:

$$\dot{\Theta}_P + ik\mu\Theta_P = -\tau\left[-\Theta_P + \frac{1}{2}(1-\mathcal{P}_2(\mu)\Pi\right], \tag{2.63}$$

where $\mu = \hat{k}\cdot\hat{n}$, $\Pi = \Theta_2 + \Theta_{P2} + \Theta_{P0}$, Θ_2 is the temperature quadrupole moment, Θ_{P2} and Θ_{P0} are quadrupole and monopole moment, respectively, of polarization. Θ_P can of course be multipole-expanded too. In the limit of $\Gamma \gg H$, the solution to (2.63) is the following [16]:

$$\Theta_{P,l}(k) \simeq \frac{15\Theta_2(k,\eta_*)}{8}\frac{l^2}{(k\eta_0)^2}j_l(k\eta_0). \tag{2.64}$$

As expected, polarization anisotropies depend on the quadrupole moment of temperature. In the tightly coupled limit ($\Gamma \gg H$), the quadrupole is proportional to the dipole [16], so (2.64) can be rewritten with as:

$$\Theta_{P,l}(k) \simeq -\frac{5k\Theta_1(k,\eta_*)}{6\dot{\tau}(\eta_*)}\frac{l^2}{(k\eta_0)^2}j_l(k\eta_0). \tag{2.65}$$

There are three important features which must be noted. First, the polarization spectrum is seen to be smaller than the temperature anisotropy spectrum by a factor of order $k/\dot{\tau}$ at the time of decoupling: this is a direct result of the fact that polarization is generated by a quadrupole moment and that the quadrupole is suppressed in the early universe [22]. Second, we

expect there to be oscillations in the polarization power spectrum because $\Theta_{P,l}$ depends on Θ_1, which undergoes acoustic oscillations. Because of this, we expect the polarization oscillations to be out of phase with the monopole (see Subsection 2.3.2). Third, there is no analogue here to the ISW effect which impacts temperature anisotropy spectrum, since polarization cannot be induced by photons moving through changing gravitational potentials. Therefore, polarization offers a view of the universe even more primordial than the one temperature gives.

(2.64) is an expression for the polarization moments from a single plane wave. However, in a realistic context a superposition of many plane waves must be considered, all with differing amplitudes Θ. The angular power spectrum from a superposition of plane waves follows from the identical calculation on the temperature anisotropies, and gives:

$$C_{P,l} = \frac{2}{\pi}\int_0^\infty dk k^2 |\Theta_{P,l}(k)|^2. \tag{2.66}$$

To derive the connection between the Stokes parameters and Θ_P, we write Q and U as a sum over all plane waves:

$$Q(\vec{\theta}) = \int \frac{d^3k}{(2\pi)^3}\Theta_P(\vec{\theta},\vec{k})cos(2\phi_k) \tag{2.67a}$$

$$U(\vec{\theta}) = \int \frac{d^3k}{(2\pi)^3}\Theta_P(\vec{\theta},\vec{k})sin(2\phi_k). \tag{2.67b}$$

Figure 2.11 schematically explains the various angles and vectors which appear in equations (2.67). The factors $e^{i\hat{k}\cdot\vec{x}}$ are set to 1, since for the spatial coordinates of the observer in its reference frame $\vec{x} = 0$. Taking the Fourier transform of (2.67)'s we get:

$$Q(\vec{l}) = \Theta_{P,l}cos(2\phi_l) \tag{2.68a}$$

$$U(\vec{l}) = \Theta_{P,l}sin(2\phi_l), \tag{2.68b}$$

where $\vec{l}$ and ϕ_l are the Fourier conjugated quantities of $\vec{\theta}$ and ϕ_k, respectively.

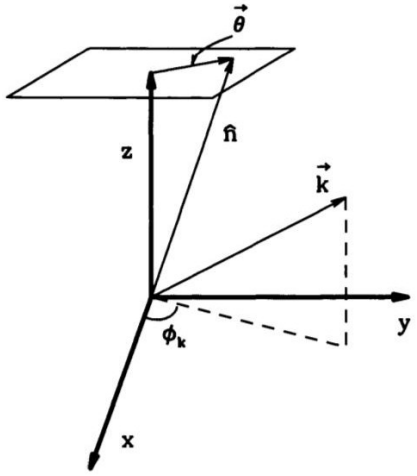

Figure 2.11: Sketch of the vectors which appear in (2.74)'s. The direction of observation is parameterized by the $\hat{n}$ direction, or by the 2D angle θ. [16]

2.4.2 E/B decomposition

We can define a linear combination of $Q(\vec{l})$ and $U(\vec{l})$:

$$E(\vec{l}) = Q(\vec{l})cos(2\phi_l) + U(\vec{l})sin(2\phi_l) \tag{2.69a}$$

$$B(\vec{l}) = -Q(\vec{l})sin(2\phi_l) + U(\vec{l})cos(2\phi_l). \tag{2.69b}$$

The quantities E and B completely specify the linear polarization field. E-mode polarization is curl-free with polarization vectors that are radial around cold spots and tangential around hot spots on the sky (see Figure 2.12). In contrast, B-mode polarization is divergence-free but has a curl: its polarization vectors have vorticity around any given point on the sky. The symmetries of temperature and polarization anisotropies allow four types of correlations: the autocorrelations of temperature fluctuations and of E- and B-modes denoted by TT, EE and BB, respectively, as well as the cross-correlation between temperature fluctuations and E-modes, denoted by TE. All other correlations (TB and EB) vanish for symmetry reasons.

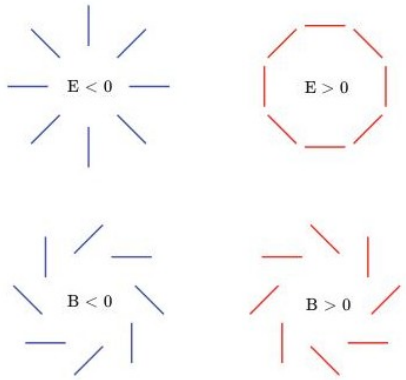

Figure 2.12: Examples of E-mode and B-mode polarization patterns. [23] Note that if reflected across a line going through the center the E-mode patterns are unchanged, while the positive and negative B-mode patterns get interchanged. As for the Stokes parameters Q and U, the sign of E and B specifies the orientation of the polarization vector.

The definitions (2.69) are such that:

$$\lim_{l\gg 1} C_l^{EE} = C_{P,l} \tag{2.70a}$$

$$C_l^{BB} = 0. \tag{2.70b}$$

This is true, however, if scalar perturbations only are considered. Tensor perturbations induce a non-zero power spectrum of B-mode polarization. Both scalars and tensors contribute to E-modes, but disentangling them relying on the differences in their spectra as a function of l is extremely hard. B-modes instead have no contamination from scalars, so an observation of B-modes in the polarization pattern would be a clear evidence of primordial gravity waves. Tensor anisotropies are often parametrized by:

$$r = \frac{C_2^T}{C_2^S}, \tag{2.71}$$

where C_2^T is the variance of the quadrupole due to tensors and C_2^S is the same due to scalars. It is then fundamental to perform polarization experiments to determine the value of the parameter r.
The fact that scalars do not produce $B-$modes while tensors do is the basis

of the famous statement that a detection of $B-$modes would be a smocking gun of tensor modes and therefore of inflation, since no other early universe mechanism produces tensor perturbations at scales larger than the horizon at recombination. Furthermore, it turns out that the tensor-to-scalar ratio is a direct measure of the energy scale of inflation, which is usually expressed as [18]:

$$V^{1/4} \sim \left(\frac{r}{0.01}\right)^{1/4} 10^{16} \text{ GeV}, \tag{2.72}$$

where V is the potential energy of the inflaton. Large values of the tensor-to-scalar ratio ($r > 0.01$) would therefore correspond to inflation happening at energy scales predicted by grand unification theories (GUT) [24, 25].

Chapter 3

CMB experiments

In Chapter 2 the CMB and its anisotropies have been characterized via their power spectra, as well as the mechanisms which have led to their generation, discussing how a detection of the curl component of the CMB polarization ($B-$modes) at large angular scales would represent a unique signature of the tensor perturbations produced during inflation, giving a possible measurement of the energy scale of GUT, since this energy scale is correlated with the tensor-to-scalar ratio r.
The hunt for $B-$modes thus represents a great possibility and challenge not only for cosmology but also for particle physics. In this Chapter the experiments that have so far been performed to detect and experimentally characterize CMB are described, focussing in particular on the most recent Planck Surveyor satellite. The purpose and design of the Large Scale Polarization Explorer (LSPE), an upcoming balloon-based experiment whose sensibility would be suitable to measure $B-$modes, are then described.

3.1 State of the art

Since its first detection in 1964 by Penzias and Wilson, several experiments have been designed and performed throughout the decades to study the CMB and measure its anisotropy and polarization spectra, using ground-, balloon-

and space-based detectors. Among the most remarkable of these experiments there are:

- the Cobe satellite [26], which was the first to detect CMB temperature anisotropies and to confirm that it followed a black body spectrum.
- the BOOMERanG balloon-based experiment [27], which determined the angular diameter distance to the surface of last scattering with high precision. This, combined with complementary data regarding the value of Hubble's constant, confirmed the geometry of the universe to be flat.
- the DASI and CBI telescopes [28, 23], which were, respectively, the first to detect CMB polarization signal and the first to obtain high resolution measurements of $E-$mode polarization.
- the WMAP satellite [29], whose data supported the ΛCDM inflationary model.

The more recent Planck Surveyor satellite recently extented and improved WMAP results, producing the most precise measurements about CMB and early universe up to date [12]. The Planck satellite was launched on May 2009 and observed the sky continuously from August 2009 to October 2013. Its payload contained an array of 74 detectors in nine frequency bands sensitive to the frequencies between 25 GHz and 1 THz, which scanned the sky with angular resolution between 33' and 5'. The detector was composed of two different instruments, the LFI (Low Frequency Instrument) and HFI (High Frequency Instrument). The scientific goals of Planck were to measure the spatial anisotropies in the CMB temperature and polarization, with an accuracy set by fundamental astrophysical limits, and to obtain information on the properties of extragalactic sources and on the dust and gas in the Milky Way. Figures 3.1, 3.2 and 3.3 report the temperature intensity map, temperature power spectra and TE and EE power spectra as measured by Planck.

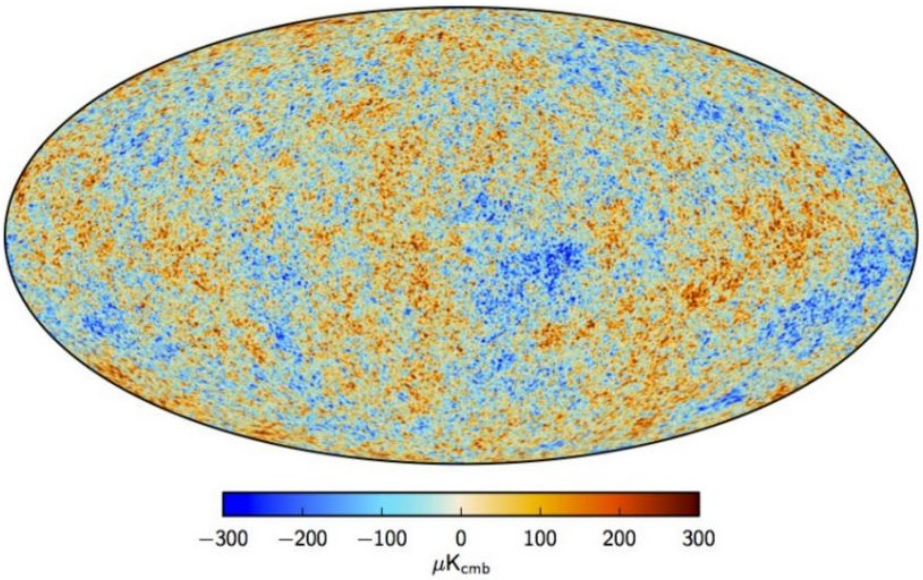

Figure 3.1: Maximum posterior CMB intensity map at 5' resolution derived from the joint baseline analysis of Planck, WMAP and 408 MHz observations. [12]

The intensity maps showed here and below are plotted using galactic coordinates.

Among the products of the Planck mission, there is the all-sky map of the polarized emission from interstellar dust and synchrotron radiation, as well as the evaluation of the various foregrounds which contaminate CMB temperature and polarization signals: thermal dust, synchrotron radiation and thermal Bremsstrahlung, also called free-free (this last one is negligible for polarization).

Interstellar dust grains emit thermal radiation, the intensity of which increases from 100-150 GHz, the favoured band to observe the CMB, and becomes dominant at frequencies larger than 350 GHz (see Figure 3.4), even at high galactic latitudes. This thermal emission has a degree of linear polarization, due to the alignment of the dust grains with the galactic magnetic field. The observed degree of polarization depends on the structure of the magnetic field and on the properties of the dust grains. This polarized emission results both in $E-$modes and $B-$modes [31], representing then a contaminant to

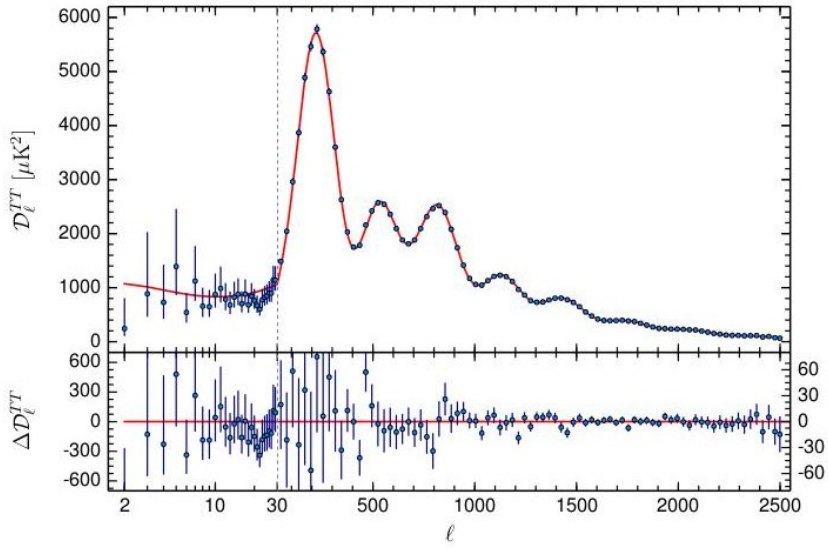

Figure 3.2: CMB temperature power spectrum, as reported by the Planck 2015 release. The upper panel shows the best-fit base ΛCDM theoretical spectrum fitted to the Planck TT-lowP likelihood. The lower panel shows the residuals with respect to this model. The error bars show $\pm 1\sigma$ uncertainties. The maximum likelihood frequency averaged power spectrum is computed using two different algorithms, one for $2 \leq l \leq 29$ and one for $l \geq 30$. [12]

the measure of the tensor-to-scalar ratio r.

Synchrotron radiation results from the helical motion of ultra-relativistic electrons around the field lines of the galactic magnetic field. In the interstellar medium the radiating electrons are the cosmic ray electrons whose energy distribution follows a power law:

$$N(E) = KE^{-\gamma} \tag{3.1}$$

where K is a normalization constant and $\gamma \sim 2.7$ is the spectral index [32]. Since the radiation produced by each electron is practically monochromatic, the resulting radiation spectrum is also a power law. It can be shown that the Stokes parameters of this radiation are non-zero, so that both $E-$modes and $B-$modes exist for synchrotron radiation.

Free-free radiation is due to thermal bremsstrahlung from ionized hydrogen

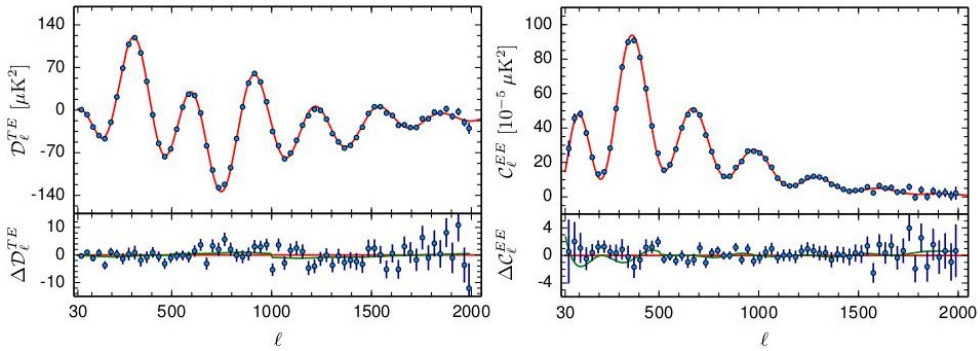

Figure 3.3: Frequency averaged TE (left) and EE (right) spectra. The theoretical TE and EE spectra plotted in the upper panel of each plot are computed from the same best-fit model used for the TT power spectrum. Residuals with respect to this theoretical model are shown in the lower panel in each plot. The error bars show $\pm 1\sigma$ errors. The green lines in the lower panels show the best-fit temperature-to-polarization leakage model (used to correct the systematics due to beam mismatch [30]), fitted separately to the TE and EE spectra. [12]

clouds. It is often called free-free emission because it is produced by free electrons scattering off ions without being captured (the electrons are free before the interaction and remain free afterwards).

Figures 3.4 and 3.5 show the spectra of fluctuations of diffuse foreground components in temperature and polarization, compared to the CMB. Figures 3.6 and 3.7 show, respectively, synchroton and interstellar dust polarization maps as measured by Planck [12].

These measures were crucial to establish the trustworthiness of the claim of $B-$modes detection by the BICEP2 experiment. BICEP2 was a low angular resolution ($\sim 1°$) telescope experiment, which operated from the South Pole from 2010 to 2012, measuring CMB at 150 GHz with a sensitivity comparable to Planck, looking on a roughly 1% patch of the sky at high galactic latitude using an array of 512 TES bolometers. In March 2014, the BICEP2 Collaboration published a highly significant detection of $B-$mode polarization in the range $30 < l < 150$. The detected $B-$mode level was higher than that projected by several existing dust models. The observed $B-$mode

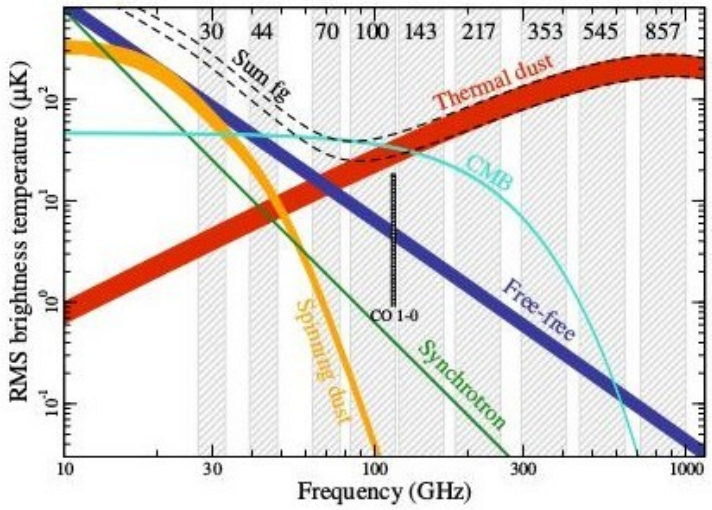

Figure 3.4: Brightness temperature rms as a function of frequency and astrophysical component for temperature. [12]

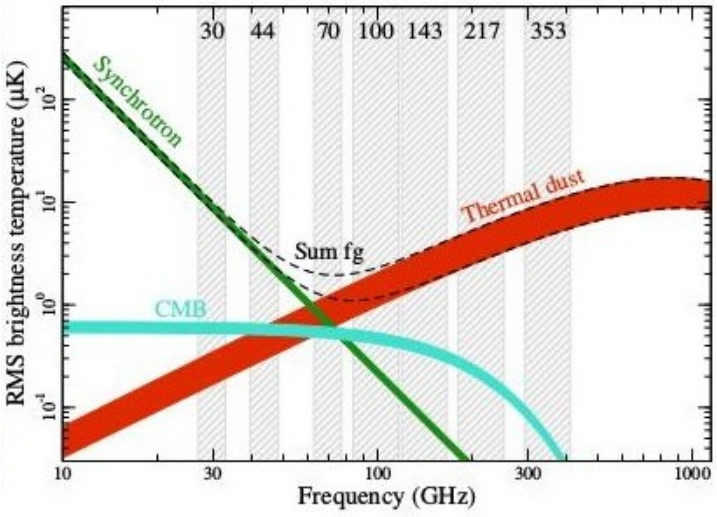

Figure 3.5: Brightness temperature rms as a function of frequency and astrophysical component for polarization. [12]

power spectrum was reported to be well fit by a lensed-ΛCDM + tensor theoretical model with tensor-to-scalar ratio $r = 0.20^{+0.07}_{-0.05}$, with $r = 0$ disfavored at 7.0σ [33]. This claim was rejected in September 2014 when Planck published its first results on dust polarization at high altitude, confirming that

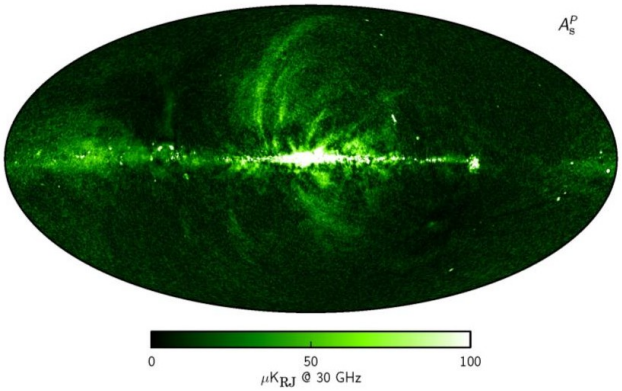

Figure 3.6: Synchrotron polarization amplitude map, $A_s^P = \sqrt{Q^2 + U^2}$, at 30 GHz, smoothed to an angular resolution of 40', produced using Planck and WMAP data. [12]

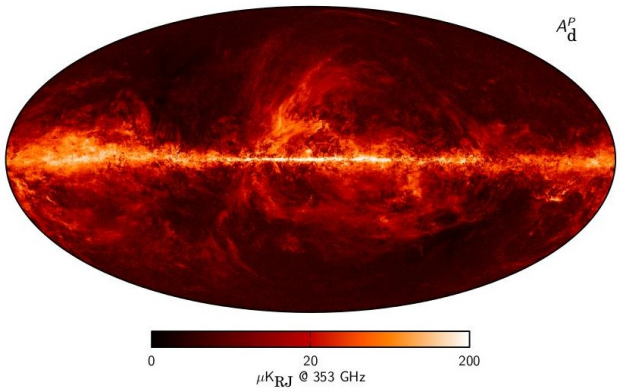

Figure 3.7: Dust polarization amplitude map, $A_d^P = \sqrt{Q^2 + U^2}$, at 353 GHz, smoothed to an angular resolution of 10', produced using Planck and WMAP data. [12]

the BICEP2 region was significantly contaminated by dust, finding a level of polarized dust emission at 353 GHz sufficient to explain the 150 GHz excess observed by BICEP2 [34].

Planck's data placed the upper bound $r < 0.10$ at 95% CL, considering a ΛCDM+r model. New experiments are under construction to improve the sensibility for detecting $B-$modes [35]. One of these is the Large Scale Polarization Explorer (LSPE) [11].

3.2 The Large Scale Polarization Explorer

LSPE is a balloon-borne mission aimed at measuring the polarization of the CMB at large angular scales, and in particular to constrain its $B-$modes. The primary target is to improve the limit on the tensor-to-scalar ratio down to $r = 0.03$ at 99.7% CL. A secondary goal is to produce wide maps of foreground polarization generated in our galaxy by sinchrotron emission and interstellar dust emission. Figure 3.8 shows that the experiment is sensitive to scales $l \lesssim 100$, so that the mission can exploit the reionization peak at $l \lesssim 10$. The angular resolution of the beam is roughly 1.5° FWHM and the experiment has a 25% coverage of the sky. The payload will fly in a circumpolar long duration balloon mission during the polar night. The launch of the balloon is forecast to take place from Longyearbyen, in the Svalbard Islands (Figure 3.9) in 2017-2018.

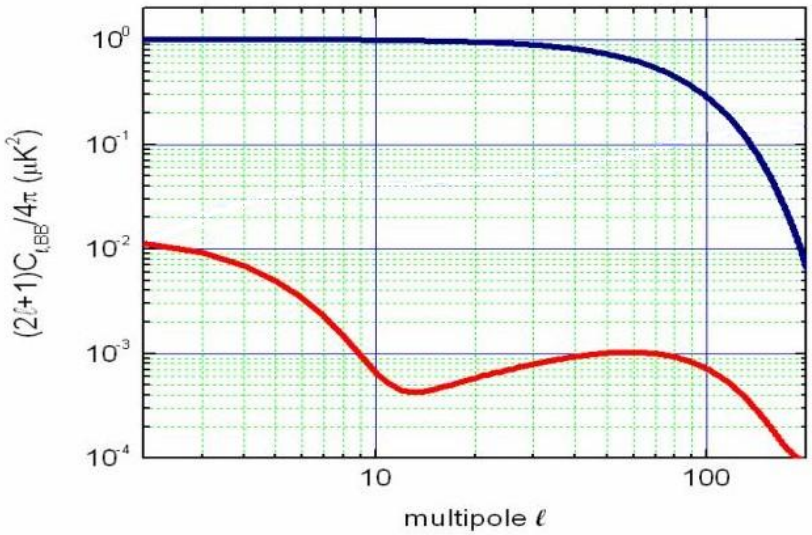

Figure 3.8: The red line represents the contribution from each multipole to the total mean square fluctuation of the tensor component of CMB polarization ($B-$modes, assuming $r = 1$. The blue line represents the beam transfer function, and therefore the sensitivity, of an experiment with a 1.5 FWHM Gaussian beam. Despite of the coarse angular resolution such an experiment collects most of the polarization signal from $B-$modes.

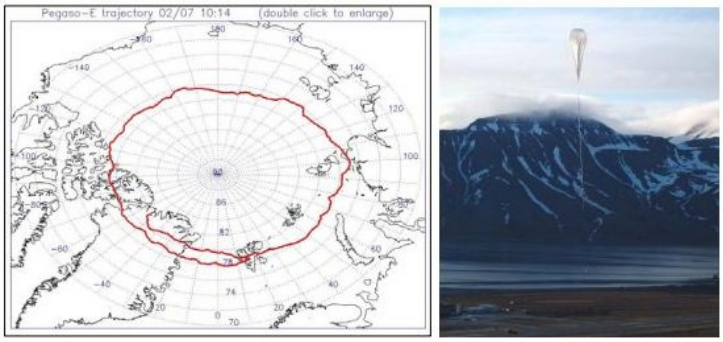

Figure 3.9: Left: ground path of one of the test flights performed by ASI to test the stratospheric circulation near the North Pole (flight performed in summer). Right: launch of a heavy-lift balloon from the Longyearbyen airport (Svalbard Islands). [11]

The nominal duration of the flight is 15 days, after which the payload will be recovered in Greenland. The instrument will spin in azimuth, using the Earth as a solar shield. The payload will mount two independent detectors: STRIP and SWIPE. The two instruments are located on a common frame (gondola), providing flight control, power supply, sky scanning and communication services. This gondola must be characterized by low weight and high stiffness. At the moment steel and aluminum alloys have been considered as construction materials. A preliminary sketch is showed in Figure 3.10. At the current level, the total weight of the payload is around 2 tons which requires a $8{\cdot}10^5$ m^3 balloon to fly at more than 37 km of altitude.
There are two main technical problems for such a mission. The first is the thermal management of the payload: the stratospheric temperature during the polar night is around -80 °C, with no solar radiation to warm up the payload. The most important impacts of these harsh conditions are on the electronics, thus thermal insulation from the external environment is mandatory to achieve self-heating conditions. The second problem is the supply power for the experiment and the telemetry: the total power requirement for a 15 days flight is estimated to be around 700 W, which means an electrical energy storage close to 10^9 J. Essential data will be transmitted to ground

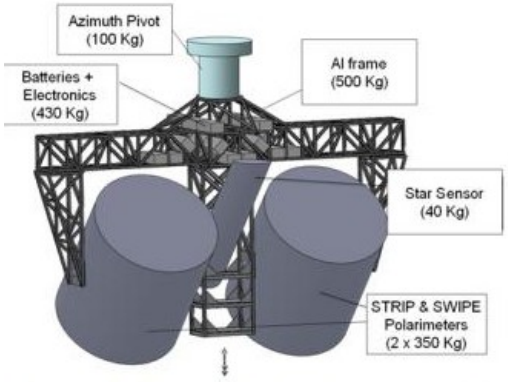

Figure 3.10: Preliminary sketch of the LSPE experiment. The width of the gondola for this configuration is ~ 5 m.[11]

through the Iridium network, using a line-of-sight telemetry when the system flies over selected locations hosting dedicated receiving stations.
The pointing direction of the telescope is controlled by a set of actuators, a processor and a set of altitude sensors. Its purpose is to produce the required scan of the sky and of the calibration sources (planets, stars), and to acquire altitude data precisely enough to allow sub-arcmin reconstruction of the pointing when performing data analysis.
The LSPE payload will spin around the azimuth axis at a constant speed of 3 rpm, while keeping the telescope elevation fixed at the chosen value, which will be changed occasionally in order the extend the sky coverage and to execute calibration scans. The main targets for this purpose will be Jupiter, the Moon and the Crab nebula. Jupiter will be observed to map the main beam; the Crab nebula to calibrate the main axis of the polarimeter, since it is the most powerful polarized source observable at the LSPE frequencies and angular resolutions; the Moon limb can be measured to calibrate the polarimeter.
As said, there will be two instruments on LSPE: STRIP and SWIPE. STRIP is an array of coherent polarimeters, whose main target is the accurate measurement of the low-frequency polarized emission, dominated by galactic synchrotron. SWIPE is an array of bolometric polarimeters, whose target is the

accurate measurement of polarization of the galactic dust foreground and of the CMB. I designed, produced and performed preliminary tests on prototypes of the detectors that will be used for the SWIPE instrument.

3.2.1 The SWIPE instrument

The Short Wavelength Instrument for the Polarization Explorer (SWIPE) is composed of 3 arrays of multi-mode bolometers to detect CMB at the frequencies of 140 GHz, 220 GHz and 240 GHz. The multifrequency detection is fundamental to achieve an efficient and reliable foreground evaluation. The system is cooled at 300 mK, with optical components and filters cryogenically cooled below 4 K to reduce the background on the detectors. The sky-scanning Stokes polarimeter uses a rotating half-wave plate (HWP) and a steady polarizer to modulate the linear polarization of the incoming brightness. The advantage of using such a system is that, while other bolometric detector for CMB compare the power measured by two detectors sensitive to the two orthogonal polarizations (see [36]), in a Stokes polarimeter both orthogonal components of polarization are measured with the same detector, thus reducing systematic effects due to uncorrelated drifts in detector response and offsets which could generate an apparent polarization signal.
High angular resolution is not a priority for this experiment, aimed at measuring CMB polarization at large angular scales. Nonetheless, an angular resolution of $1 \div 2$ degrees is desired so that SWIPE can be calibrated against Planck data at the same frequency and at the same angular scales. In Figure 3.11 a sketch of the instrument is shown. More details about key subsystems of SWIPE are reported below.

Telescope The optical system is an axially symmetric refractive telescope, cooled cryogenically to reduce its emission and exploit the advantages of the cold stop of the optical system (a cold stop is a baffle that prevents stray infrared light, radiated from the housing, from impinging upon the detector from outside its intended field [37]). The cold stop is efficiently matched to

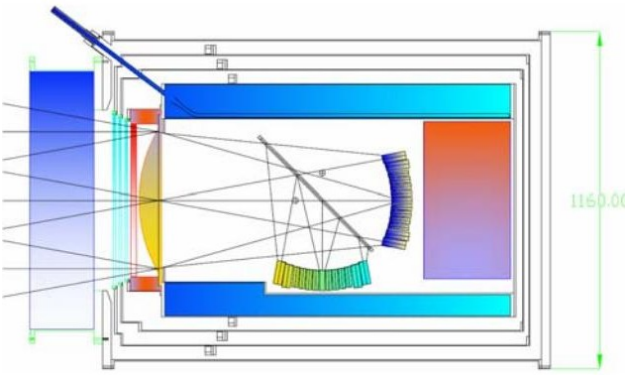

Figure 3.11: Sketch of the SWIPE instrument, fully enclosed in a large liquid ^{4}He cryostat. From the left the large foam window (60 cm clear aperture), the three thermal filters connected to the 130 K, 30 K and 2 K stages of the cryostat, the rotating HWP, the HDPE lens, the beamsplitting wire-grid and the two focal plane arrays of Winston horns and detectors are visible. The rectangle on the right encloses the sub-K refrigerator. The volume of liquid ^{4}He is 250 litres and the weight of the system is 300 kg. [36]

the multi-mode patterns of the horns (see later), which allows the collection of multiple modes of oscillations of the incoming radiation, granting a more efficient detection than with single-mode detectors. The optics consist in a single 470 mm diameter lens and a 440 mm diameter cold stop, resulting in an entrance pupil of 450 mm diameter. The field of view (FOV) is split in polarization into two curved focal planes, both 300 mm in diameter, by a 500 mm diameter wire grid tilted at 45°. Each focal plane will contain 165 detectors.

Polarization modulator The response of the focal plane to the polarization is modulated by a 500 mm diameter rotating Half-Wave Plate, built with photolithtographic techniques. The HWP introduces a controlled phase shift Γ between the two polarization components of the incident radiation, according to relationship:

$$\Gamma = \frac{2\pi \Delta n L}{\lambda_0}, \tag{3.2}$$

where Δn is the birefringence of the material, L the thickness of the plate and λ_0 is the vacuum wavelength of the radiation. In this way the two components of the polarization can be separated.

Detectors The CMB detectors in SWIPE are spider-web bolometers with Transition-Edge Sensor (TES) thermistors, described in detail in Chapter 4. Parabolic Winston horns are used to efficiently couple the optical stages of the detector with the TES bolometers, put in the backshort of the horns. The Winston horns will be coupled to 12 modes for the 140 GHz band, 30 modes for the 220 GHz band and 34 modes for the 240 GHz band. The detectors will be disposed on each focal plane like depicted in Figure 3.12. Due to their multi-mode operation, Winston horns can achieve very high

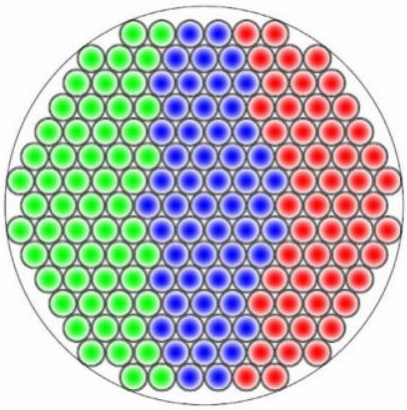

Figure 3.12: Final configuration of the focal plane for LSPE. The color code is red for 140 GHz, green for 220 GHz and blue for 240 GHz.

coupling efficiency in the main beam and ensure high suppression of stray radiation, through the incoherent superposition of the propagated modes at large angles. In the photon noise limit, a single detector sensitive to n modes is exactly as sensitive as n detectors each sensitive to a single mode. Thus, if angular resolution is not an issue (and this is the case of LSPE), a focal plane tiled with N single-mode detectors can instead be tiled with N/n multi-mode detectors, with no loss of sensitivity.

Readout The readout of the detectors is achieved using the frequency domain multiplexing (FDM) technique, both for reduction of costs and implementation simplicity, by means of superconductive LC filters in series to each TES. FDM and filters design and tests are discussed in detail in Chapter 5. A cold LC filter is placed in series with each TES bolometer like in Figure

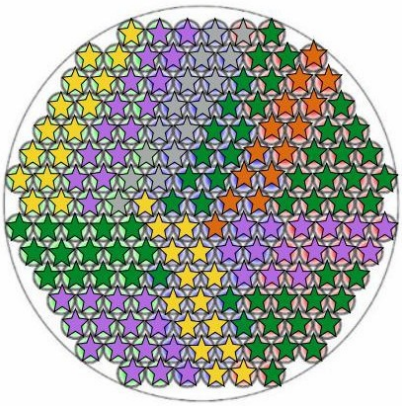

Figure 3.13: Possible multiplexing readout configuration of the detectors of each focal plane.

3.14, with the double function of limiting with its bandwidth the current noise from the resistive TES bolometer and allowing the N detectors to be biased with a single pair of wires. A comb of N bias frequencies is sent down this single pair. The tuned filter passes the appropriate bias carrier and suppresses the other N-1. The N sensors with their series filters are connected in parallel and the currents are summed and readout with a single SQUID, which is the most sensible magnetic flux-to-voltage converters currently available. SQUIDs principle of operation and performance test are discussed in Chapter 6.
Warm demodulation electronics separate and recover the individual detector signals. SWIPE will use a 16-channel multiplexing, as sketched in Figure 3.13, in the range of 200 kHz-1.6 MHz.

Electronics Bolometer bias carriers are synthesized by a FPGA, which also performs demodulation and digitization of the bolometer outputs. The

comb of the bias carriers is converted to analog through a DAC and then sent to the RLC. The signal is amplified by a SQUID, after that active nulling is performed by sending an identical comb with a displacement of 90° at the SQUID input. In this way only the physics signal is amplified. After being digitized by an ADC, the FPGA demodulates the signal and sends it to the readout control computer via an Ethernet port.

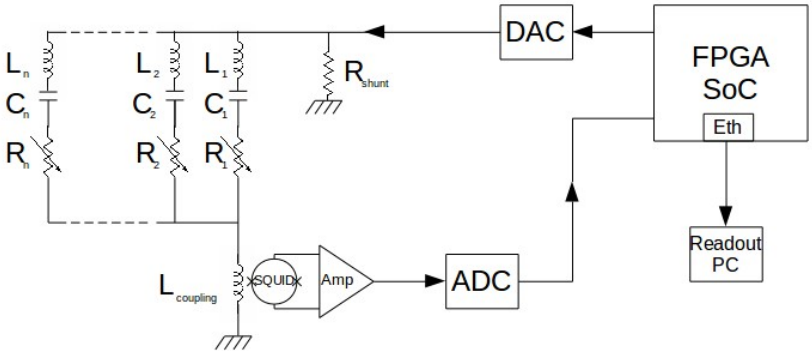

Figure 3.14: Simplfied schematics of the readout electronics.

Chapter 4

Transition-Edge Sensor bolometers

The detectors of CMB radiation are of two types: coherent and direct. In the former, radiation is coherently received by an antenna, preserving the phase information, and then amplified and measured. Above 100 GHz the noise performance of this technique is severely reduced. Since our goal, as explained in Chapter 2, is to measure CMB at frequencies of 140 GHz, 220 GHz and 240 GHz, it is prefereable to use direct detection. Direct detectors incoherently measure the power of the radiation, giving a signal proportional to the power of the input signal.

The direct detectors commonly used to detect CMB are bolometers. Bolometers are thermal detectors of radiation, consisting of an absorber element with a heat capacity C (J/K) which is thermally connected to a heat sink at T_0 through a weak thermal conductance G (W/K). When the bolometer absorbs a radiation power P from the sky, its temperature increases to:

$$T = T_0 + \frac{P}{G}\left(1 - e^{-t/\tau}\right) \tag{4.1}$$

where $\tau = C/G$ is the intrinsic thermal time constant of the bolometer.

Absorbers typically consist of a thin layer of metal deposited on a suspended backing structure. A convenient geometry for the absorber in balloon- and space-based experiments is the spider-web: the geometry spacing is such that

radiation can be effectively absorbed while simultaneously providing a very small cross-section for absorption of cosmic rays.
The rise in bolometer temperature due to the absorbed CMB radiation is measured with a thermistor, which is attached at the center of each spider-web bolometer. A competing thermistor technology for CMB bolometers is the superconducting transition-edge sensor (TES) [38].
In this Chapter the choice of a TES bolometer as collector of CMB is motivated, describing its principles of operation and showing the results of a performance simulation we implemented, using the experimental transition curve of a TES realized at the INFN Laboratories of Genova and a simulated CMB signal. The simulation was necessary to establish the design of the LC filters for multiplexing.

4.1 Theory of operation

A transition-edge sensor is a thin film of superconducting material that is electrically biased in the transition between its normal and superconducting state. Since the transition is very sharp (as shown in Figure 4.1), the derivative of the resistance R with respect to the temperature T is very high, so that very small changes in temperature produce large changes in resistance.

The sharpness of the transition is characterized by the dimensionless parameter α:

$$\alpha = \frac{T}{R}\frac{dR}{dT} = \frac{d\ln R}{d\ln T}. \tag{4.2}$$

For TES bolometers α ranges from 50 to 1000. The positivity and the generally high value of α give the TES the fundamental property of strong electrothermal feedback [38]. As said, the sensor is operated applying a voltage bias ($O(\mu V)$) to the film. When operating at its transition, the absorption of optical power from the sky makes the temperature of the sensor rise, strongly increasing in consequence the resistance of the film. The electrical bias power

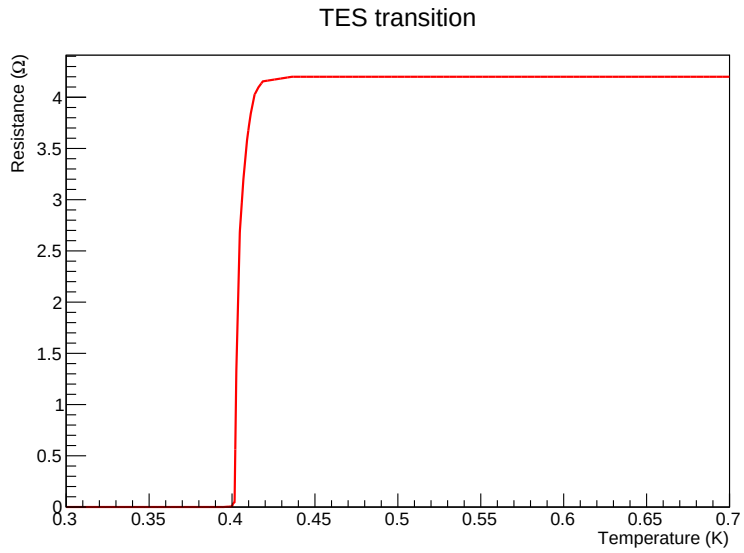

Figure 4.1: Experimental superconducting transition of a TiAu TES bolometer. The measurement has been performed at INFN Section of Genoa mounting the TES on a probe and introducing it in a liquid Helium Dewar bottle. The points have been taken exploiting the thermal stratification of the He in the Dewar bottle.

of the TES:

$$P_b = \frac{V_b^2}{R} \tag{4.3}$$

then decreases. The reduction of dissipated power turns into a decrease in temperature, which brings back the TES to the operating point. As explained later, there is a limitation to the dynamic range a TES bolometer can operate this way.

Dynamic range, responsivity, sensitivity and bandwidth of a TES are quantified in the following way [7]. Let us consider energy conservation in the bolometer in the presence of a constant optical power P_{op} coming from the sky and a bias power P_b. If the frequency of the bias power is high enough so that the bolometer sees it as a constant (and this is a fundamental condition for multiplexing), the balance equation for this system is:

$$P_{op} + \frac{V_b^2}{R} = G(T - T_0) + C\frac{dT}{dt}. \tag{4.4}$$

$G = dP_{total}/dT$ is the differential thermal conductance of the weak link at temperature T, C is the heat capacity. The term $C\frac{dT}{dt}$ is zero once the TES reaches the equilibrium temperature. If we introduce a time-varying term $\delta P e^{i\omega t}$, the balance equation becomes:

$$P_{op} + \frac{V_b^2}{R} + \delta P e^{i\omega t} - \frac{V_b^2}{R^2}\frac{dR}{dT}\delta T e^{i\omega t} = G(T - T_0) + G\delta T e^{i\omega t} + i\omega C \delta T e^{i\omega t} \quad (4.5)$$

so that we can distinguish a time-independent and a time-dependent equation:

$$P_{op} + \frac{V_b^2}{R} = G(T - T_0) + C\frac{dT}{dt} \quad (4.6a)$$

$$\delta P e^{i\omega t} = \left(\frac{P_b \alpha}{T} + G + i\omega C\right)\delta T e^{i\omega t}. \quad (4.6b)$$

(4.6)a states that the average optical power and electrical bias power must match the power leaving the bolometer through the weak thermal link to the bath, plus the power used by the TES to change its temperature. The terms in brackets in (4.6)b have the dimension of a thermal conductance and define the effective complex thermal conductance of a TES bolometer under strong electrothermal feedback:

$$G_{eff} = \frac{P_b \alpha}{T} + G + i\omega C. \quad (4.7)$$

(4.7) shows that strong electrothermal feedback effectively increases G, which is equivalent to say that the feedback opposes to changes in temperature, mantaining the TES at the operating transition point for relatively large changes in incident power.

The strength of the electrothermal feedback can be defined as the ratio of the change in electrical bias power to the change in the TES power, in analogy to the loop gain in an electronic feedback circuit:

$$L(\omega) = \frac{-\delta P_b}{\delta P_{total}} = \frac{P_b \alpha}{G T_b (1 + i\omega\tau_0)} = \frac{L}{1 + i\omega\tau_0} \quad (4.8)$$

where $L = P_b\alpha/GT_b$ is the DC gain. The gain rolls off at $\omega > 1/\tau_0 = G/C$. At frequencies $\omega << 1/\tau_0$, the temperature change:

$$\delta T = \frac{\delta P_{op}}{G(L+1)} \quad (4.9)$$

is reduced by a factor of $L+1$ compared with that without strong electrothermal feedback.

The signal output of the sensor, called *responsivity*, is the current change δI in response to an incident optical power δP. Since:

$$\delta I = -\frac{V_b}{R^2}\frac{dR}{dT}\delta T = -\frac{P_b\alpha}{GT}\frac{G}{V_b}\delta T = -\frac{LG}{V_b}\delta T \tag{4.10a}$$

$$\delta P = \left(\frac{P_b\alpha}{T} + G + i\omega C\right)\delta T = G(L + 1 + i\omega\tau_0)\delta T, \tag{4.10b}$$

S_i can be written as:

$$S_i = \frac{\delta I}{\delta P} = \frac{-1}{V_b}\frac{L}{L+1}\frac{1}{1+i\omega\tau}, \tag{4.11}$$

where $\tau = \tau_0/(L+1)$ is the effective thermal time constant of the TES bolometer. In the limit $L \gg 1$ with $\omega \ll 1/\tau$, the responsivity $S_i \simeq -1/V_b$ is simply a constant given by the bias voltage. The strong electrothermal feedback then linearizes the response of the TES, producing a very stable and linear responsivity.

As anticipated, there is a fundamental limitation to the TES dynamic range. If the incident power exceeds $G(T - T_0)$ the bolometer saturates, i.e. goes from superconductive to normal state. In this condition, the responsivity rapidly drops to zero. It is then important to estimate the maximum anticipated incident power to the TES, ensuring that the thermal conductance and the operating and bath temperature result in enough power margin to avoid saturation.

The sensitivity of a TES is often expressed in terms of noise equivalent power (NEP), defined as the signal power that gives a signal-to-noise ratio of 1 in a 1 Hz output bandwidth. An output bandwidth of 1 Hz is equivalent to half a second of integration time (the one half factor is due to the Nyquist-Shannon theorem). The units of NEP are $\mathrm{W}/\sqrt{\mathrm{Hz}}$. A smaller NEP means a more sensitive detector.

There are several sources that contribute to the NEP of a TES bolometer. Since the mean-square fluctuations from uncorrelated sources can be added

in quadrature, the NEP can be written [39]:

$$NEP^2 = NEP^2_{photon} + \gamma 4kT^2G + \frac{4kT/R}{S_i^2}\left(\frac{\tau}{\tau_0}\right)^2 \frac{1+\omega^2\tau_0^2}{1+\omega^2\tau^2} + \frac{i^2_{SQUID}}{S_i^2}. \quad (4.12)$$

The terms in (4.12) describe, respectively, the photon noise, thermal fluctuations noise, Johnson noise and amplifier noise. The two noise terms which mainly set limits to the performance of the bolometer are the thermal fluctuations noise and the Johnson noise. Thermal fluctuations noise is caused by the random propagation of energy carriers between the thermometer and the heat sink. The fluctuations of power flow have a spectral density $4kT^2G$, adjusted by a factor γ, close to unity [7]. Johnson noise generates a fluctuating current in a closed circuit with a spectral density $4kT/R$. However, these fluctuations are reduced by the large dynamic resistance of a bolometer in the strong electrothermal feedback limit [7]. The i_{SQUID} term is the noise current of the SQUID amplifier.

The optical power incident on the sensor is carried by photons, so the Poisson statistics of photon arrival affects the sensitivity with which this power can be measured. For an integration time of 1 second, the NEP_{photon} is:

$$NEP_{photon} = \sqrt{2P_{op}h\nu}. \quad (4.13)$$

We want the sensor performance to be dominated by photon noise, so a fundamental requirement is the thermal fluctuations noise to be less than the optical NEP. To achieve this, operating temperatures of 400-500 mK are typically chosen. Once T and T_0 are chosen to ensure photon-noise limited performance, the thermal conductance G of the detector must be chosen to satisfy:

$$P_{max} < G(T - T_0). \quad (4.14)$$

P_{max} is the maximum anticipated power. Its evaluation depends on several factors, like the maximum temperature of the radiation source, the throughput of the optics coupling the radiation source to the sensor and the bandwidth of the radiation.

The bandwidth of the TES determines the speed at which the detector can

respond to incident radiation. Since, as we have seen, the intrinsic time constant τ_0 is reduced by a large factor because of strong electrothermal feedback, the response to the incident radiation is in practice limited by the time incident power takes to thermalize in the absorber. This is solved by adding a large additional thermal capacitance to the absorber.
The readout system of the TES bolometer must satisfy several requirements:

- low input impedance Z_{in};
- low input current noise $i_{readout}$;
- large forward gain.

The first requirement ensures that the presence of the readout system does not affect the current flowing through the thermistor. Since the TES bolometers typically have normal resistances of $\sim 1\Omega$, this requirement becomes $Z_{in} \ll 1\Omega$. The second requirement ensures that the readout of the TES bolometer does not degrade the NEP of the detector. The third requirement ensures that the bolometer signal is amplified to a higher level than the input voltage noise of subsequent room temperature amplification stages in the readout.
These requirements are met by DC SQUID ammeters. Their principles of operations are exposed in Chapter 6.

4.2 Performance simulation

We performed a simulation in ROOT for the behavior of a TES bolometer. Our aim was to verify that strong electrothermal feedback (ETF) maintains the detector on its transition slope, and for which conditions this happens. We also verified that the interactions with cosmic rays do not contribute to the noise in a significant way and characterized the bandwidth of the TES.

4.2.1 Strong electrothermal feedback

In our simulation the TES spider-web was characterized using the parameters of the TiAu TES realized and measured at the INFN Laboratories of Genoa (Figure 4.1 reports its transition curve), so we used $G = 7 \cdot 10^{-11}$ W/K (thermal conductance) and $C = 7.1 \cdot 10^{-12}$ J/K (thermal capacitance). The slope of the TES transition is around 400 mK, so we chose a temperature for the heat sink $T_0 = 250$ mK. The two last important parameters to be set are the bias voltage supplied to the TES bolometer and the optical power absorbed by the detector.

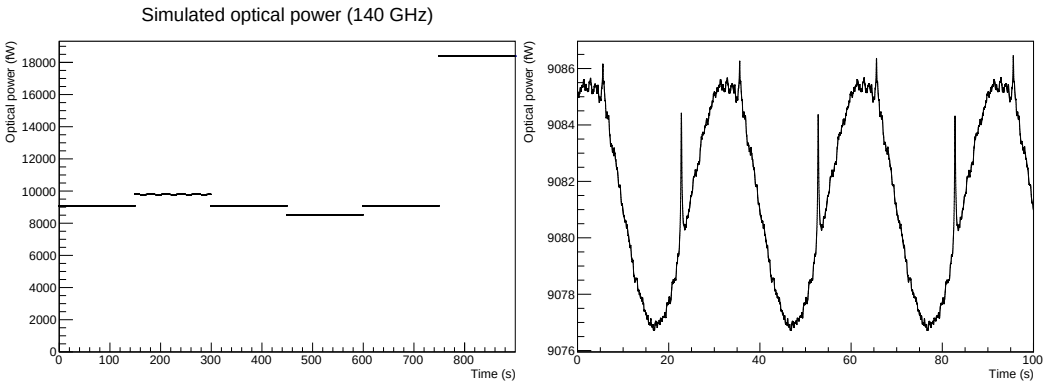

(a) (b)

Figure 4.2: Simulated optical power absorbed by the detector during the flight (a) and zoom of the first 60 seconds showing the fluctuations (b).

For the latter, within the LSPE collaboration a preliminary simulation was performed for the optical power on the detectors during the flight. In Figure 4.2 the simulated signal at 140 GHz is reported. The constant contributions to the power are due to the CMB monopole and to instrumental emission; the time varying contributions are due to signal (CMB anisotropies) and foregrounds (dust and atmosphere, the latter assumed to be constant). In the simulation the instrument rotates with a speed of 2 rpm, thus generating the 30 seconds oscillation which is modulated by the CMB dipole anisotropy. The largest spikes are due to signals from small sources in the galactic plane.

No noise has been included. The signal is smoothed to the angular resolution of LSPE.
The signals due to CMB anisotropies, dust and galactic plane sources were generated using the galactic maps released by Planck. The signal due to the atmosphere was calculated using the HITRAN atmosphere model. The elevation of the telescope was set to, from left to right in Figure 4.2a, 45 degrees, 30 degrees, 45 degrees, 60 degrees, 45 degrees and 10 degrees, each step lasting 150 seconds. In the last step (10 degrees) the telescope was made to point to a planet.
The same has been done for the 220 GHz and 240 GHz bands. From this simulation we found an indicative value for the optical power absorbed from the sky of 9 pW at 140 GHz, 6 pW at 220 GHz and 14 pW at 240 GHz. This information is used to choose the bias voltage for the TES bolometers. Its value must be such that ETF mantains the TES on its transition slope: if too high a bias voltage is fed to the TES, the latter goes out of its superconducting state and it is incapable of detecting the smallest fluctuations in the optical power absorbed. In Figures 4.3 and 4.4 the TES temperature and output current responses for a voltage bias $V_b = 2$ μV are reported. The starting temperature for the TES has been set to 500 mK. We can see how ETF mantains the TES on the slope of its transition, except for the data at elevation 10 degrees: here the optical power coming from the planet, combined with the bias voltage, makes the TES temperature rise above its transition temperature. The TES becomes then a normal conductor, its responsivity drops to zero and it is no longer sensitive to the fluctuations due to anisotropies. This is clear in Figure 4.4a, where from 750 s to 900 s the output current drops (because the TES becomes a normal conductor) becoming constant in time.
In Figure 4.5 we can see how the strong electrothermal feedback allows to measure temperature variations down to the order of 10^{-7} K, which is at least the necessary sensitivity to detect $B-$modes (see again Figure 1.3).

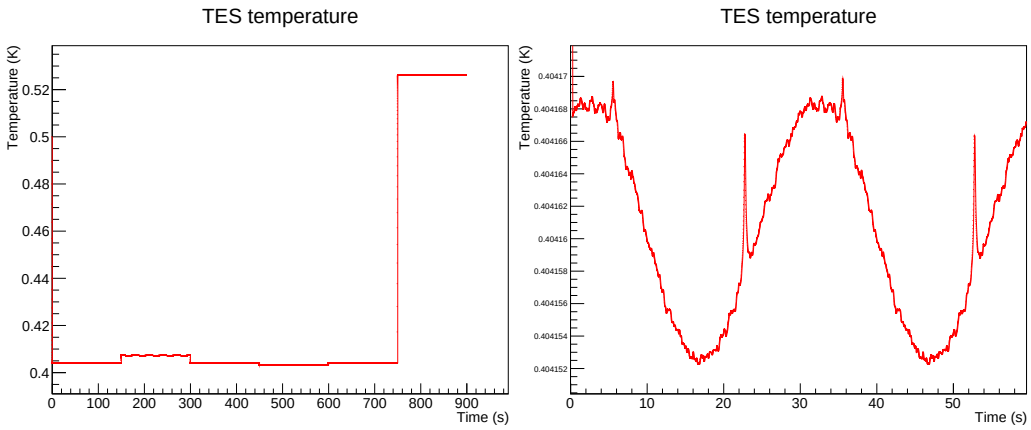

(a) (b)

Figure 4.3: Temperature response of the TES (a) and zoom of the first 60 seconds showing the order of 10^{-5} K fluctuations in temperature, due to anisotropy (b).

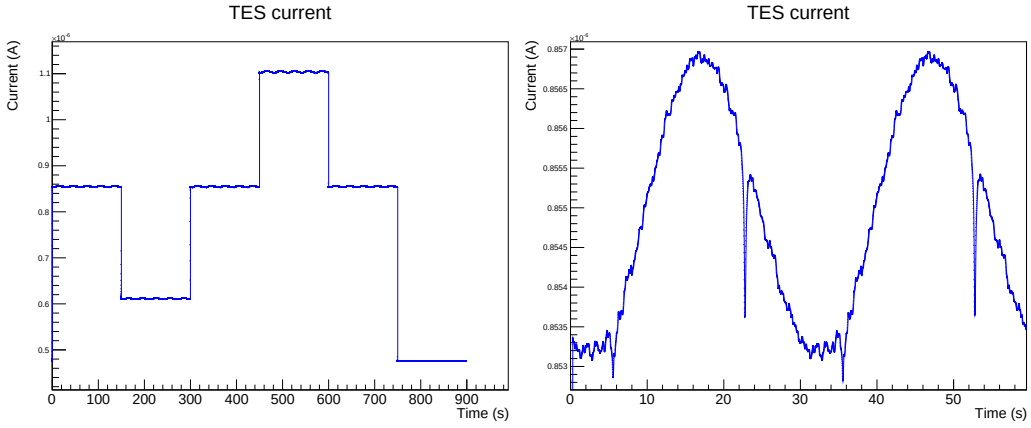

(a) (b)

Figure 4.4: Current response of the TES (a) and zoom of the first 60 seconds showing the fluctuations in the current due to the fluctuations in temperature (b).

4.2.2 Bandwidth

To evaluate the bandwidth of the TES, we generated sinusoidal optical power modulations at 12 different frequencies, with an amplitude of 9 pW, and fed

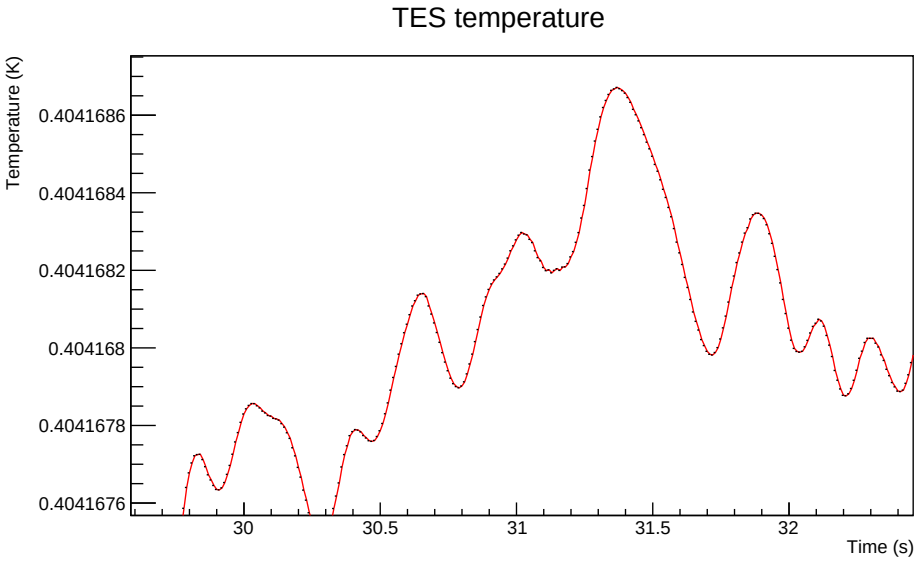

Figure 4.5: Zoom of Figure 4.3b.

it to the TES in place of the simulated signal previously given. The response current of the TES to the different power modulations is plotted in Figure 4.6 (for clarity, only four frequencies are plotted).

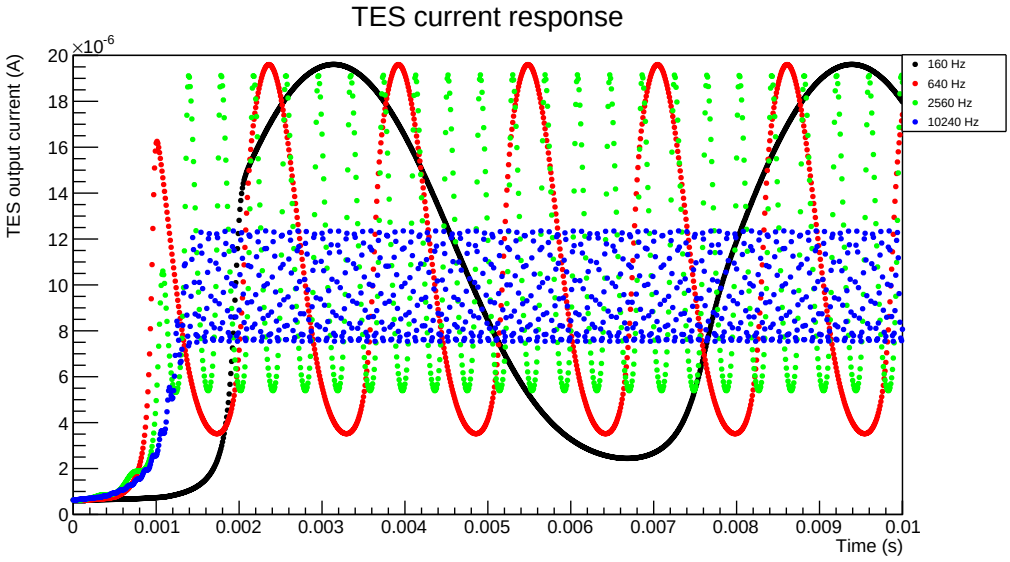

Figure 4.6: Response current of the TES at four different optical power modulations with constant amplitude of 9 pW.

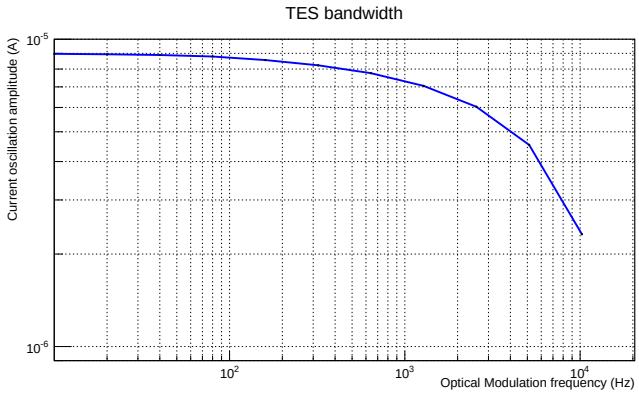

Figure 4.7: Bandwidth of the simulated TiAu TES.

We can see how, with the increasing frequency, the response of the TES decreases. In Figure 4.7 we report the bandwidth of the TES, up to a frequency of ~ 20 KHz. The decreasing of the TES response to high frequency modulations justifies the choice of frequencies for multiplexing in the range ~ 100 KHz $\div \sim 2$ MHz: the TES is unable to follow the rapid variation of the bias voltage and thus sees it as a constant contribute to the power supplied to it, which efficiently puts it in the desired point along its transition curve.

4.2.3 Interaction with cosmic rays

One important effect to evaluate is the undesired contribution of interactions of cosmic rays with the TES. We simulated the effects of cosmic rays on the TES bolometer during the LSPE circumpolar flight. Using known distributions of cosmic rays in the atmosphere [40] (see Figure 4.8), a Geant4 simulation was performed to find the distribution for the released energy by cosmic rays in the spiderweb (see Figure 4.9), which was simulated as a 70 nm thin Gold sheet.

We can see that the energy deposit due to a cosmic ray is of the order of keVs. We simulated an energy deposit of 1 keV and 4 keV in a TES bolometer which was absorbing an unmodulated (constant) optical power of 9 pW (140 GHz) from the sky, starting from a temperature of 410 mK. The effects

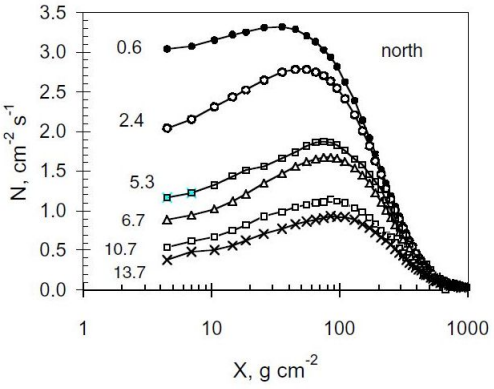

Figure 4.8: Cosmic rays flux in the atmosphere in function of the depth, at various latitudes. [40]

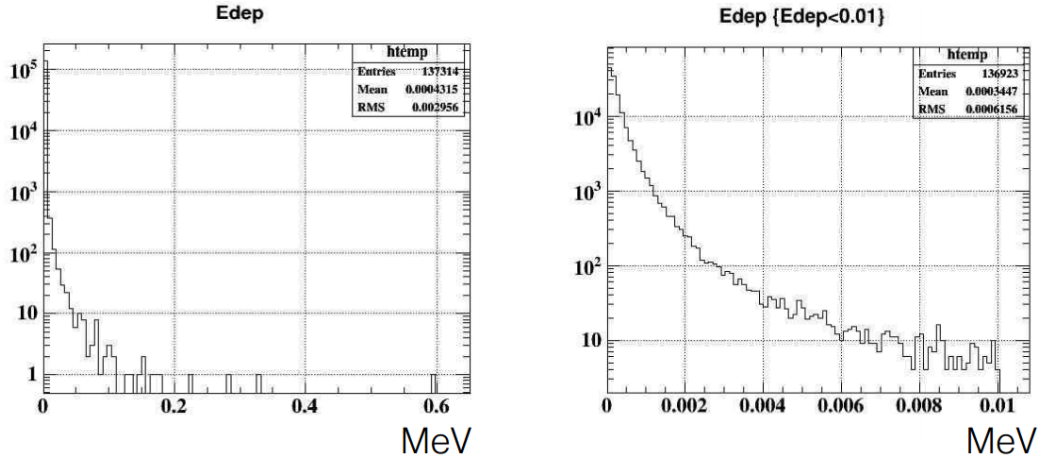

Figure 4.9: Geant4 simulation for the energy deposit of cosmic rays in the TES.

are reported in Figures 4.10 and 4.11.

As we can see, the effect of the cosmic ray is to create a spike in the TES response, which would be (for an unmodulated optical power) otherwise constant, after thermalization has occurred. Figure 4.12 shows the current response of the TES to the simulated optical power with a cosmic ray releasing 1 keV at $t = 5$ sec.

A deposit of 1 keV makes the detector blind for roughly 3 ms. The expected interaction rate is of 0.4 Hz, which means a cosmic ray event every $2 \div 3$ sec-

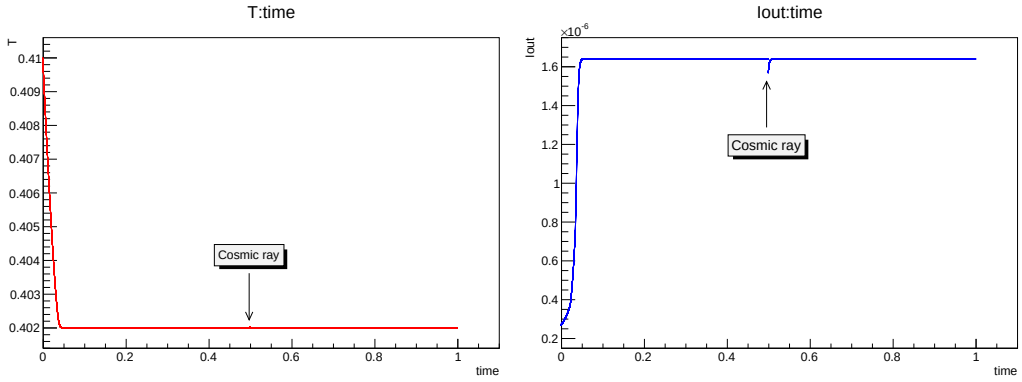

(a) (b)

Figure 4.10: TES response to a cosmic ray releasing 1 KeV of energy at 500 ms. As a result, the TES is blinded for $\sim$ 3 ms.

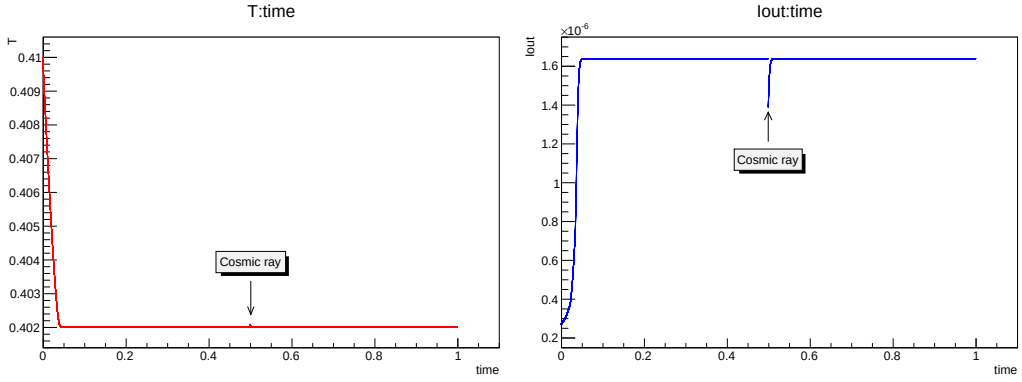

(a) (b)

Figure 4.11: TES response to a cosmic ray releasing 4 KeV of energy at 500 ms. As a result, the TES is blinded for $\sim$ 10 ms.

onds. Such energy deposits are easily recognisable as cosmic ray events and do not contribute significantly to dead time; low energy deposits however are difficult to individuate and can give dead time contributions to the analysis. Algorithms to eliminate cosmic rays interactions from the data stream are under development.

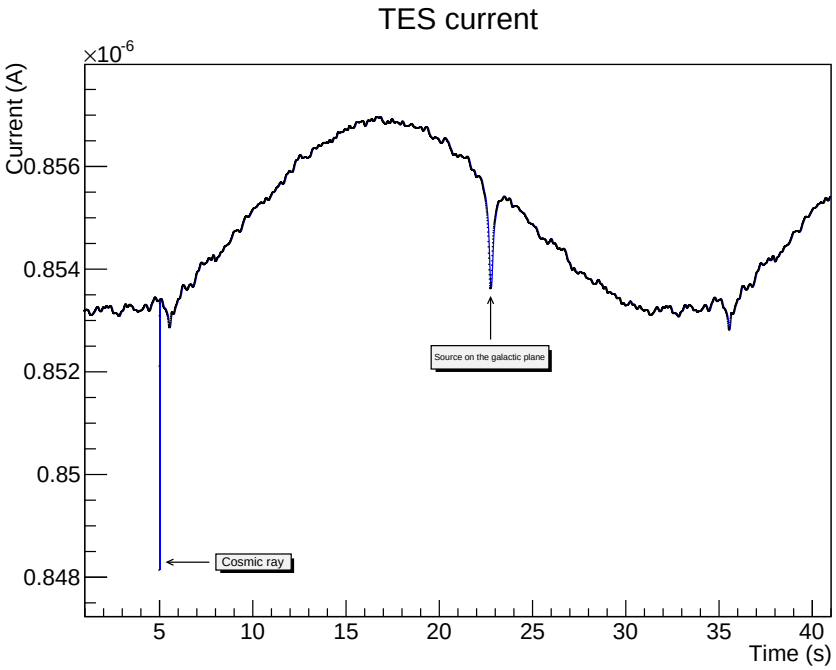

Figure 4.12: TES response current, comparing the spike generated by a source on the galactic plane with the one generated by an energy deposit of 1 KeV due to a cosmic ray.

Chapter 5

Superconductive resonant filters

The large array of TES detectors requires a multiplexed readout. Each member of a set of n sensors is biased at a unique frequency, separating the n sensor signals in frequency and thus allowing them to be summed. This is accomplished placing a tuned filter consisting of a superconducting inductor and a capacitor in series with each multiplexed sensor. The use of the LC filters has three advantages: I) they allow the sensors to be biased with different frequencies, II) their narrow bandwidth limits the Johnson current noise and prevent it from leaking to the other n channels in a multiplexed set, III) they allow a comb of biases to be sent down a single pair of bolometer bias wires which greatly reduces the wire count to the sub-kelvin temperature stages, passing the appropriate bias frequency and suppressing the other n-1. In this Chapter the design, fabrication and cryogenic tests of the elements constituting the filters are described, as well as the reasons for frequency domain multiplexing and the cryogenic test facility and preliminary tests.

5.1 Filters requirements

An LC filter acts as a resonant bandpass filter, whose resonance frequency is determined by:

$$f_r = \frac{1}{2\pi\sqrt{LC}}, \tag{5.1}$$

where L and C are, respectively, the inductance and capacitance of the filter. The TES bolometer can be seen as a small resistance $R \sim 1\Omega$ placed in series with the filter. The impedance of a RLC circuit is:

$$Z(\omega) = \sqrt{R^2 + X^2}, \tag{5.2}$$

where:

$$X = \omega L - \frac{1}{\omega C} \tag{5.3}$$

is the reactance, i.e. the imaginary part of the impedance. f_r is the frequency at which the inductive reactance ωL and the capacitive reactance $1/\omega C$ are equal, so that X is null and the impedance is minimum.
The bandwidth of the LC is determined by the sum of all the dissipative elements in series with the filter. For an ideal LC filter in series with a TES bolometer with resistance R, the bandwidth (defined as the width of the resonance measured at 3 dB of attenuation) is given by:

$$\Delta f = \frac{R}{2\pi L}. \tag{5.4}$$

In practice there is also parasitic contribution R_p since the inductor and the capacitor are not ideal elements. The dissipative terms are summarized in the quality factor Q of the filter, defined as:

$$Q = \frac{f_r}{\Delta f} = \frac{2\pi f_r L}{R + R_p}. \tag{5.5}$$

A fundamental requirement for the filters is that Q must be high enough not to compromise the voltage bias applied to the bolometer. This means that the equivalent series resistance (ESR) of the LC filter must be negligible with respect to the operating resistance of the bolometer. In particular, Irwin and

Hilton [41] showed that to ensure sensor stability the ESR must be smaller than the operating resistance of the bolometer by at least 5.8.
Another requirement is to achieve LC filter resonance frequencies within a precision of percent from the design frequencies, so that the desired channel spacing can be maintained.
Finally, since in LSPE there are going to be ~ 300 sensors to be multiplexed, the size of the microchips must be suitable to fit in the physical dimensions of the focal planes. This means that the LC filters dimensions must be of the order of centimetres.

5.2 Inductors

Since the LC filters are placed near the sensors, thus operating at sub-K temperatures, a natural choice is to use a superconducting coil to obtain the desired high quality factor. The standard inductor design for this applications is a superconducting coil deposited on and insulated from a square slit washer (see Figure 5.1).

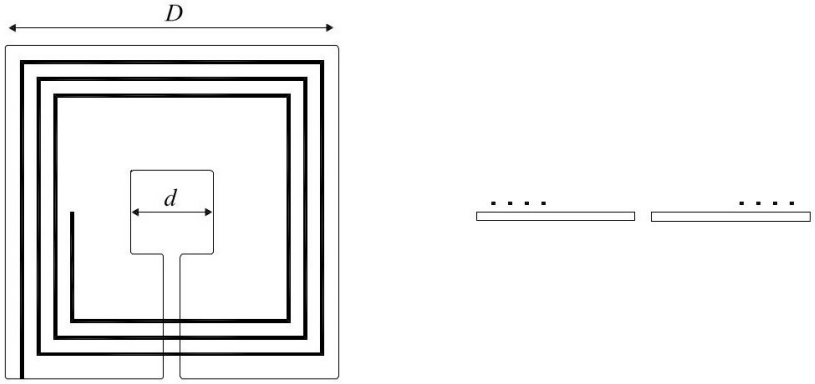

Figure 5.1: Not to scale sketch of the square spiral inductor used for the LC filters. [39]

This is the same design used for planar SQUIDs. The purpose of the square slit washer is to exploit the Meissner effect [42] to minimize the stray magnetic field, channelling the field lines into the central hole. This leads to very low

mutual inductances between coils placed close together. Jaycox and Ketchen [43] showed that for an n turn coil placed over a square slit washer with outer diameter D and inner diameter d, if $D > d$, the inductance is close to:

$$L = 1.25\mu_0 d n^2. \tag{5.6}$$

For its relatively high critical temperature (~ 9 K), a standard choice is to use Niobium to fabricate the coil and the washer. The dielectric between them produces a parasitic capacitance C_p, which can be considered in parallel to the capacitor of the LC filter. We want these capacitance to be very high, so to be negligible with respect to C. We chose SiO_2 as fabrication material for the dielectric of the inductor, which has a $\varepsilon_r = 3.9$.
For Irwin and Hilton, the filter bandwidth given in (5.4) must exceed the sensor bandwidth by at least a factor of 5.8. Since the sensor bandwidth and resistance are all the same, the filter bandwidth should be a constant. Therefore, the same inductance value must be used for all the filters, which means that the resonance frequencies are set by varying the capacitances. From the simulated bandwidth of Figure 4.7, we found a sensor bandwidth of roughly 2 KHz. This means that the inductance must be $\lesssim 30$ μH.

5.2.1 Design

The results showed in Figure 5.2s and (5.6) are used as the basis of my design for the inductors.
If D is the outer diameter of the inductor, d the inner diameter, w the width of the track of the coil and s the spacing between two adjacent tracks, it can be easily deduced that these parameters are related by:

$$\frac{D-d}{2} = nw + (n-1)s. \tag{5.7}$$

I chose to design 3 different inductors so that the values of L were ~ 20 μH, 30 μH and 40 μH, with $w = 5$ μm and $s = 10$ μm. As a result, the number n of turns per coil is of the order of 150.
To create such a layout and simulate its electromagnetic behaviour I made us

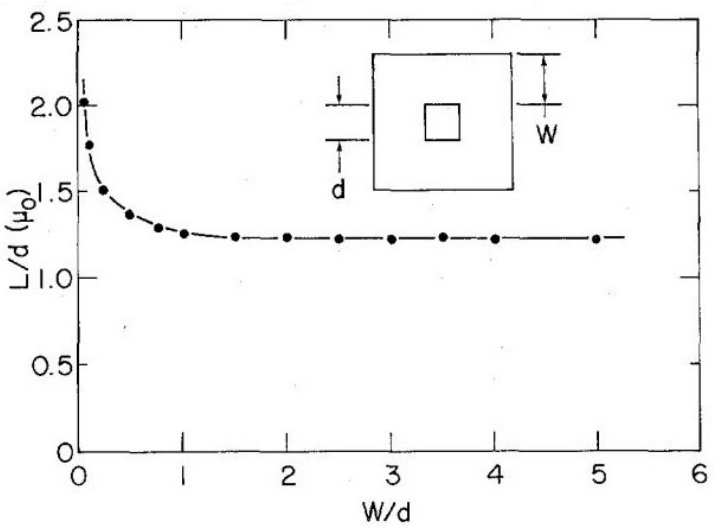

Figure 5.2: Results from Jaycox and Ketchen for inductance values of square slit washer inductors. If $W > d$, L tends to the values predicted by (5.6). [43]

of SONNET software [44], a standard for this kind of applications. In Figures 5.3, 5.4 and 5.5, as an example of the study I made, the SONNET design for the 40 μH inductor, the result of a simulation showing the predicted L as a function of the frequency and the simulated supercurrent in a smaller inductor are reported.

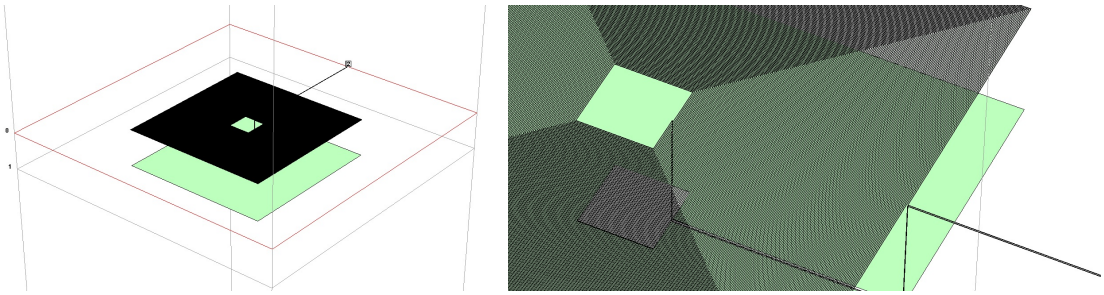

(a) (b)

Figure 5.3: Design of the 40 μH realized in SONNET. The dimensions are $D = 6$ mm, $d = 0.86$ mm, $w = 5$ μm, $s = 10$ μm.

The superconducting Niobium of the spiral and the washer is simulated assuming it is a perfect conductor with zero resistance, surface reactance and

surface inductance. This model is a very good approximation for frequencies below 150 GHz (which is our case), where effects such as kinetic inductance are not present. The Niobium is simulated with thickness equal to zero. The SiO_2 thickness between the spiral and the washer is 1 μm. This structure is sandwiched between a 150 μm thick layer of intrinsic Silicon and 1 mm of air.

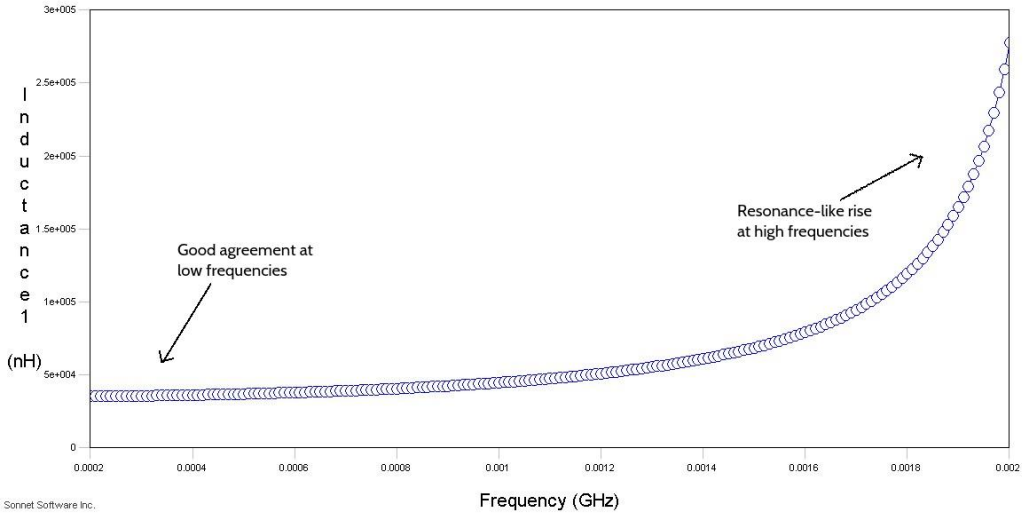

Figure 5.4: Result of the SONNET simulation for the 40 μH inductor, performed from 200 KHz to 2 MHz.

The result of the simulation (Figure 5.4) shows a very good agreement with the foreseen value at low frequencies. The resonance-like rise at $\sim$ 2 MHz is due to the presence of a parasitic capacitance, which can be estimated to be roughly 150 pF. The presence of this rise is due to the method used by the software to simulate the inductance, which consists in computing the Y-parameters (or admittance parameters) matrix of the two-port network designed in SONNET, so that:

$$\begin{pmatrix} I_1 \\ I_2 \end{pmatrix} = \begin{pmatrix} Y_{11} & Y_{12} \\ Y_{21} & Y_{22} \end{pmatrix} \begin{pmatrix} V_1 \\ V_2 \end{pmatrix}, \tag{5.8}$$

where the I and V parameters are simulated by the software. The inductance is then computed as:

$$L = \frac{Im(Y_{11})^{-1}}{2\pi\nu}, \tag{5.9}$$

where $Im(Y_{11})$ is the imaginary part of the admittance parameter Y_{11} and ν is the frequency.

The parasitic capacitance causing this rise must be eliminated from the frequency range of interest. This can be achieved using a different dielectric with a higher ε_r, such as Nb_2O_5 ($\varepsilon_r = 41$), or either reducing or lowering the thickness of the dielectric so to move the resonance out of the 200 KHz $\div$ 2 MHz range.

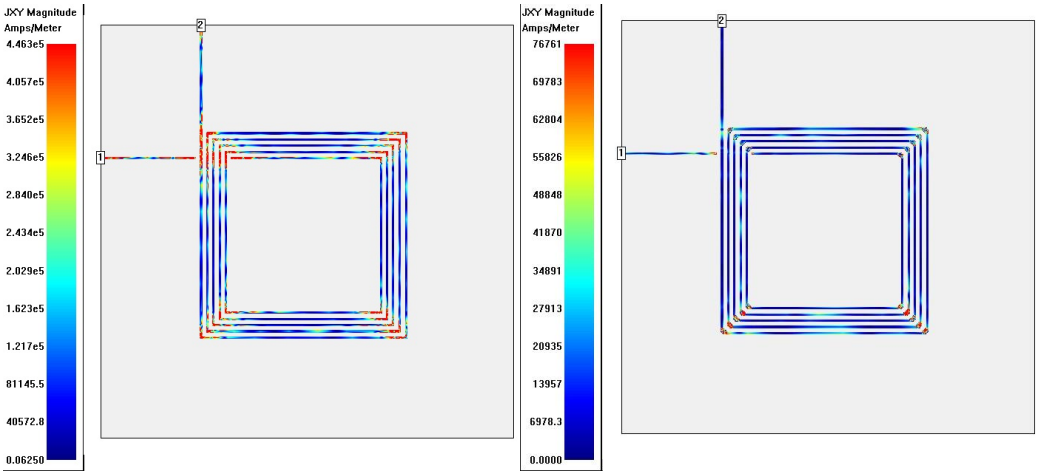

(a) (b)

Figure 5.5: Supercurrent simulated in SONNET, before and after the rounding of corners. The graphics shown are for $\nu = 500$ KHz.

Ultimately, I used SONNET to perform a simulation of the supercurrent circulating in a simple 5-turn spiral (Figure 5.5). We can see how the supercurrent density intensifies around corners. To avoid the superconductor to locally exceed its critical current, the corners of the spiral have been rounded. This solution effectively reduces the supercurrent at corners.

5.2.2 Fabrication

The fabrication of the inductors is made through photolithography and sputtering. I used the layout of the spiral inductors created in SONNET to make a design for the 3" photolithographic mask in AutoCAD (Figure 5.6).

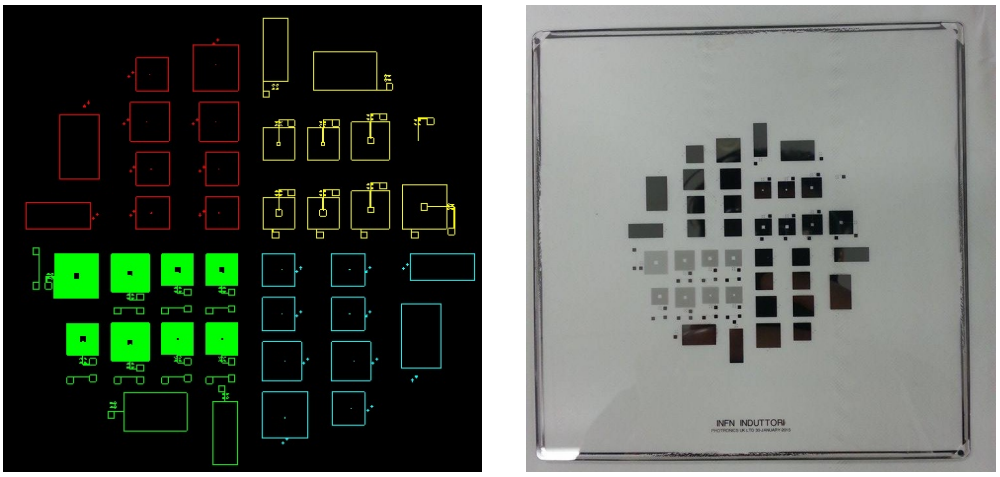

(a) (b)

Figure 5.6: (a) AutoCAD design for the photolithographic mask. In the upper right quarter there is the design for the Nb square slit washer sputtering, in the upper left and lower right quarters there is the design for the SiO_2 dielectric and in the lower left quarter there is the design for the Nb spiral inductors.
(b) Quarz mask after production.

The mask hosts 8 inductor designs: 2 with expected $L \sim 20$ μH, 2 with expected $L \sim 30$ μH, 2 with expected $L \sim 40$ μH, 1 with the design of the ~ 20 μH but without washer, and 1 with $s = 30$ μm instead of 10 μm, with expected $L \sim 10$ μH. I also inserted the design for 2 capacitors of expected $C \sim 1$ nF.
Later on I realized the design for a second photolithographic mask, holding the geometries for other three inductors with expected $L \sim 4$ μH, 6 μH and 8 μH.
Fabrication of spiral inductors have been realized first at the INFN Laboratories of Genoa and later at the National Enterprise of nanoScience and

nanoTechnology (NEST) of Pisa. I report here the description of the various steps for the production of the inductors. Details on the receipts I optimized are reported in Appendix C.

Spiral photolithography. 2" Si wafers with a thin SiO_2 layer deposited on one side are used. Due to the criticality of the structure, the use of a high resolution photoresist is chosen. A traditional resist normally has a resolution of ~ 2 μm, a high resolution photoresist has a resolution of less than 1 μm. I used negative photoresists, so that during the development process the unexposed parts to UV light, covered by the designs on the mask, are washed away.
The photoresist is deposited on the wafer as in Figure 5.7(a) and is then spin coated to obtain a uniform layer, whose thickness depends on the spinning speed as shown in Figure 5.7(b) [45].

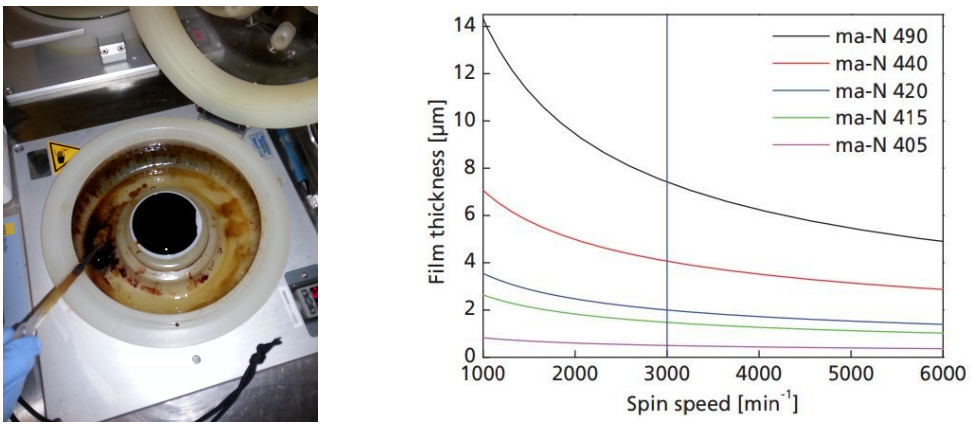

(a) (b)

Figure 5.7: (a) Deposition of photoresist on the 3" wafer placed on the spinner. (b) Relation between spinning speed and resulting thickness for various photoresists. The thickness goes as the inverse squared root of the spinning speed.

The resist is then pre-baked; the pre-baking (also called "softbaking") minimizes the solvent concentration in the photoresist in order to avoid mask contamination or sticking to the mask and improve the photoresist adhesion

to the substrate.
I used a Süss MJB4 mask aligner (Figure 5.8) to expose the sample with UV radiation.

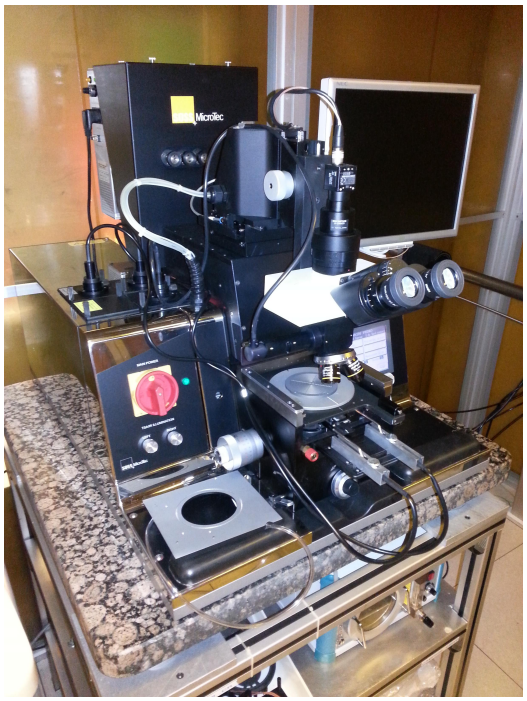

Figure 5.8: Süss MJB4 mask aligner.

The radiation triggers a photochemical reaction, changing the chemical-physical properties of the exposed photoresist, while leaving unaltered the areas covered by the patches of the mask. The sample is then put in a bath of developer to remove the unexposed photoresist, and then put in water to stop the development process. The sample is then observed at the microscope and, if needed, attacked with Oxygen plasma to remove residual photoresist (Figure 5.9).
In Figure 5.10 an example of a successful lithography, as well as some examples of typical defects, are reported.

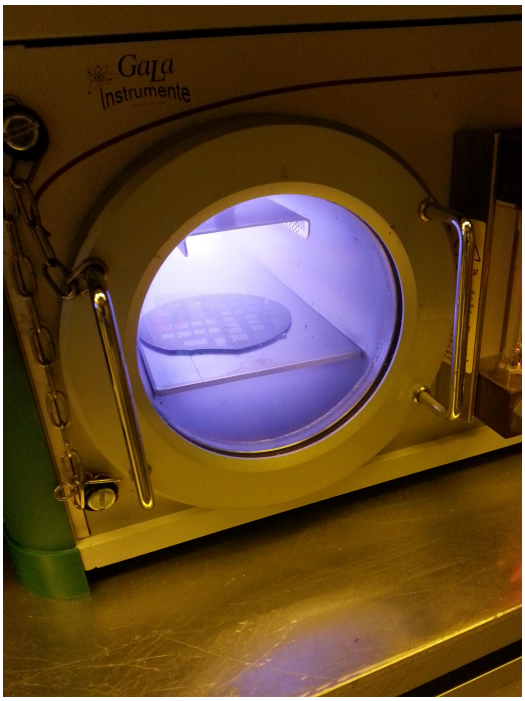

Figure 5.9: Sample in the Oxygen plasma chamber.

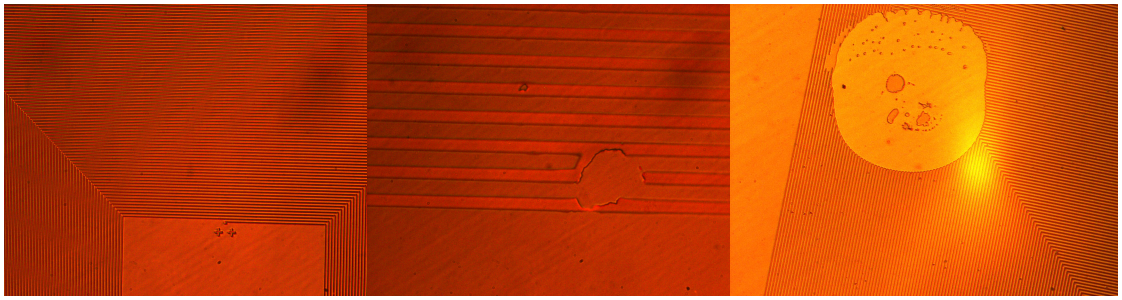

(a) (b) (c)

Figure 5.10: (a) Successful lithography of a spiral inductor (4x zoom).
(b) Short-circuit and interruption between adjacent tracks of the spiral (40x zoom).
(c) Hole in the lithographed structure caused by a blob of air trapped in the photoresist (4x zoom).

Nb spiral sputtering and lift-off. Once the pattern for the spiral inductors have been photolithographed, the sample is inserted in the sput-

tering chamber (Figure 5.11). After inserting the sample in the chamber

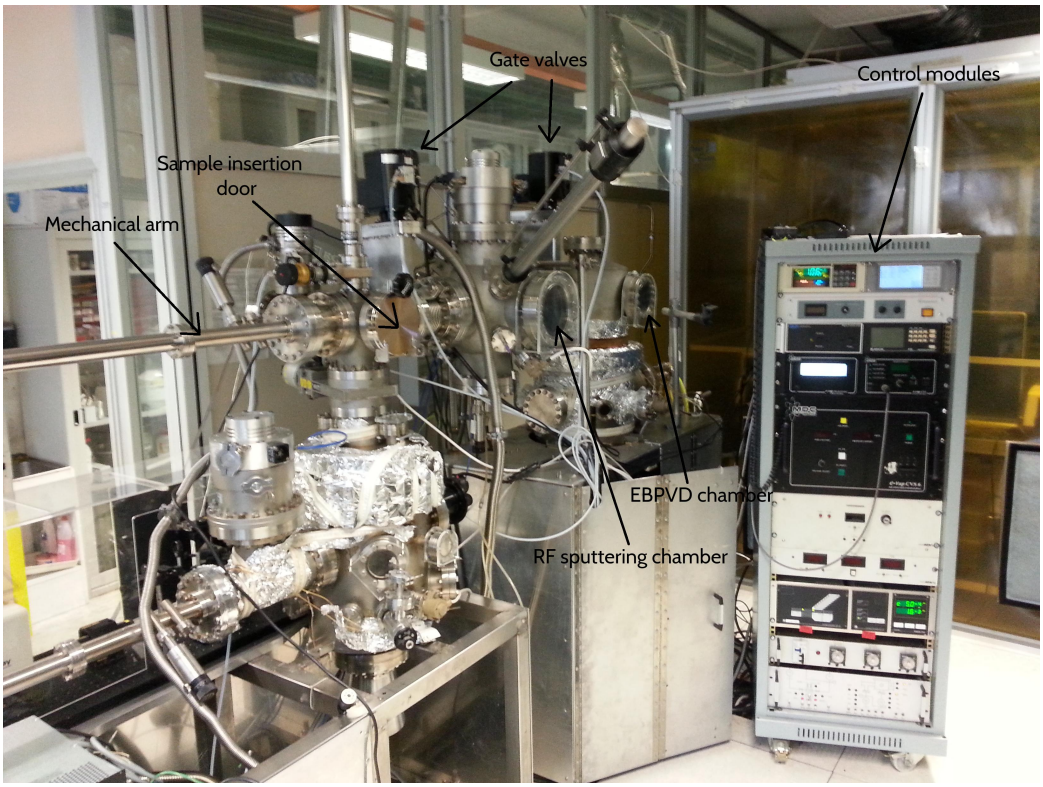

Figure 5.11: Sputtering facility of the INFN Laboratories of Genoa.

and positioning it above the Niobium target, vacuum is pumped to a level of $10^{-8\div9}$ mbar, then 99.9999% pure Argon is inserted until the pressure reaches roughly 10^{-2} mbar.

RF high tension is then applied between the mechanical arm holding the target (anode) and the metal plate holding the Niobium target (cathode, not visible in the figure), ionizing the Argon gas in the chamber and thus creating a plasma (see Figure 5.12). An magnetic field is applied so that the Ar^+ ions are accelerated towards the Niobium target, extracting Nb atoms which are emitted in all directions, and in particular in the one pointing to the sample. In this way a uniform layer of Niobium is deposited all over the sample, with a deposition speed of 30 nm/min. The thickness of the Nb spiral must be much smaller than the thickness of the photoresist. Otherwise, the final pro-

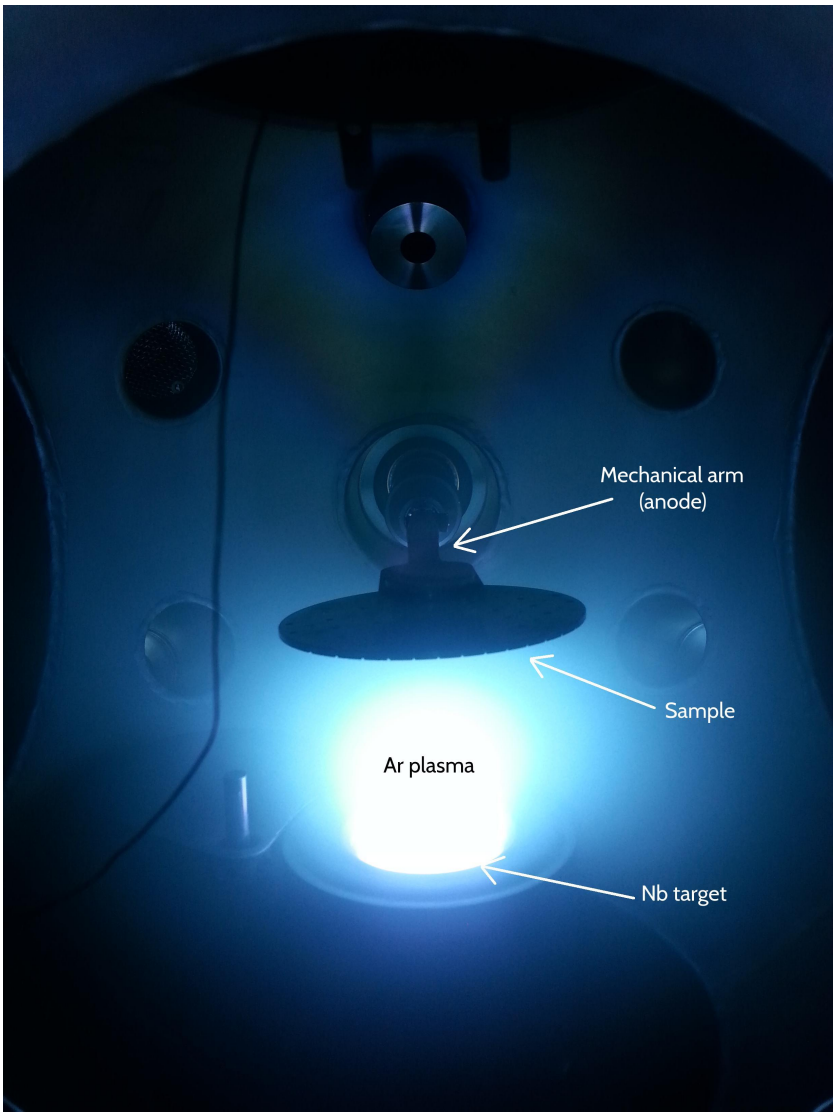

Figure 5.12: Nb sputtering process in the facility of the INFN Laboratories of Genoa.

cess of lift-off to remove the photoresist would be compromised. To lift-off the photoresist, the sample is put in a bath of Acetone, until the photoresist and the Niobium attached above it is completely removed. In Figure 5.13 the lift-off process of a square slit washer, and not of an inductor, for sake of clarity is shown. The various steps of photolithography and lift-off are resumed in Figure 5.14.

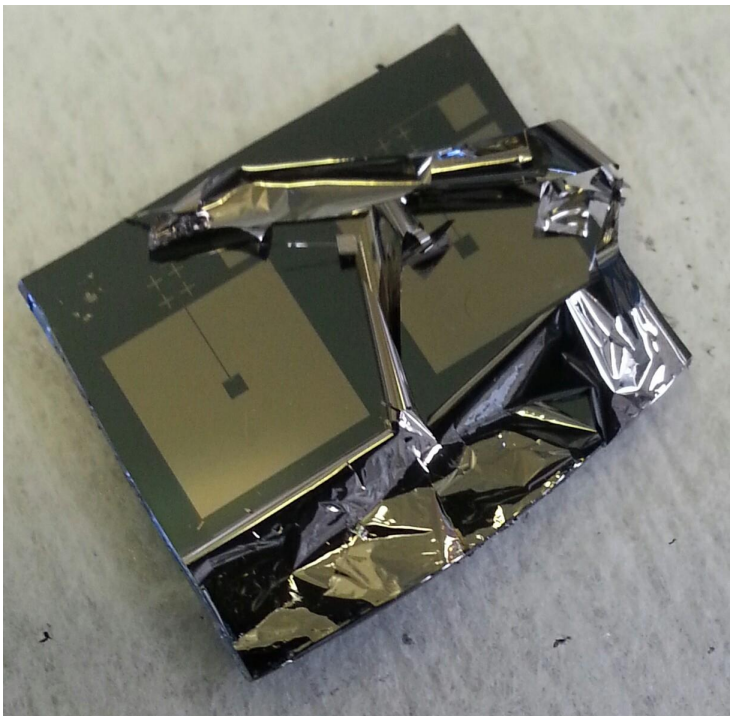

Figure 5.13: Lift-off process of a square slit washer, realized at the NEST laboratories. The Si chip is put in Acetone. The photoresist with Niobium attached above is being removed, looking like a thin film.

SiO_2 and vias. The photolithography for the layer of SiO_2 follows the same steps previously described. The only difference is that, since this structure is not critical as the spiral inductors, a traditional photoresist is used, presenting a worse resolution but allowing a higher thickness after spinning. In Figure 5.15 a correct photolithography for the SiO_2 layer is shown.
For the deposition of SiO_2 at INFN Laboratories of Genoa I exploited the Electron Beam Physical Vapor Deposition (EBPVD) chamber of the deposition facility of Figure 5.11. In this process a SiO_2 target anode is bombarded with an electron beam, obtained by a Tungsten filament in high vacuum (10^{-9} mbar). The electron beam causes the target material to evaporate and deposit onto the sample in a thin uniform layer.
The only substantial issue that could occur in this process is, during the lift-off, the incomplete opening of the holes for the vias connecting the center

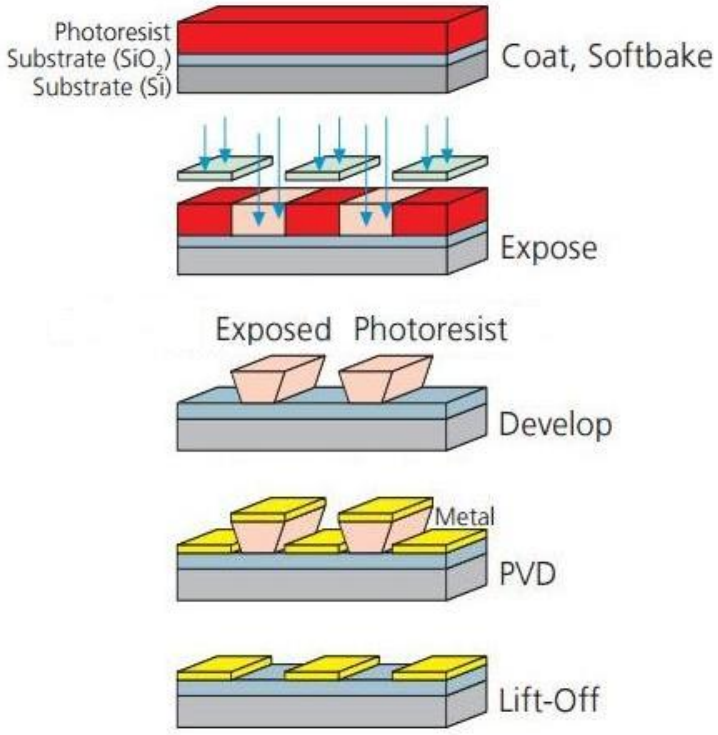

Figure 5.14: Summary of the steps in the photolithography and lift-off processes. [45]

of the spiral to the Niobium bridge within the slit of the washer (see Figure 5.16), due to the presence of residual resist. This is solved by bombarding with Oxygen Plasma or by doing numerous bathing cycles with Acetone and Ethanol.

Nb slit washer. The photolithographic and sputtering processes follow the same lines previously described. The criticality in this structure is in the bridge between the center of the spiral and the external bonding pad, since it is a very long track with a very small section (5 $\mu m^2 \times 2 \div 3$ mm track). A high resolution photoresist cannot be used here because a thickness of more than 1 μm is needed. A typical defect in this lithography is the "violin string" effect, shown in Figure 5.17, due to an incorrect rooting of the photoresist to

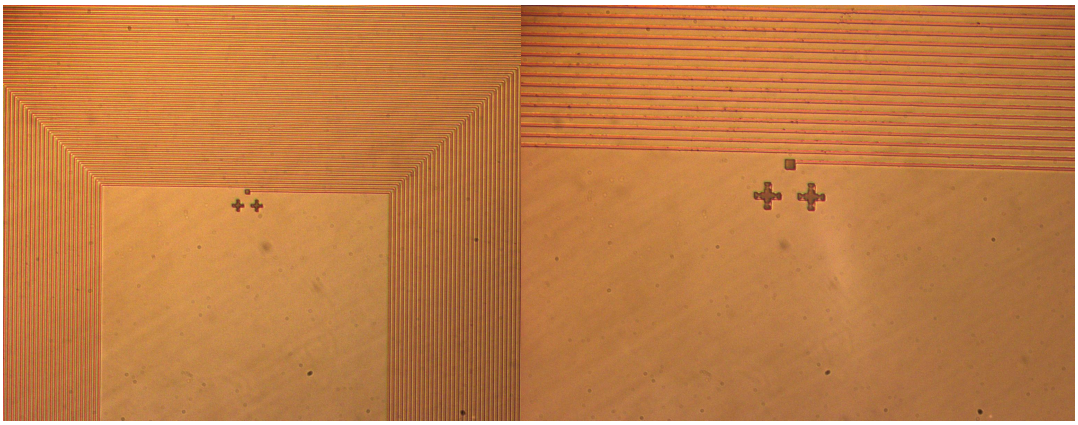

(a) (b)

Figure 5.15: (a) Microscope view of the lithography for the SiO_2 deposition (4x zoom). The dark areas are exposed photoresist.
(b) Particular of the via, with alignment crosses (10x zoom).

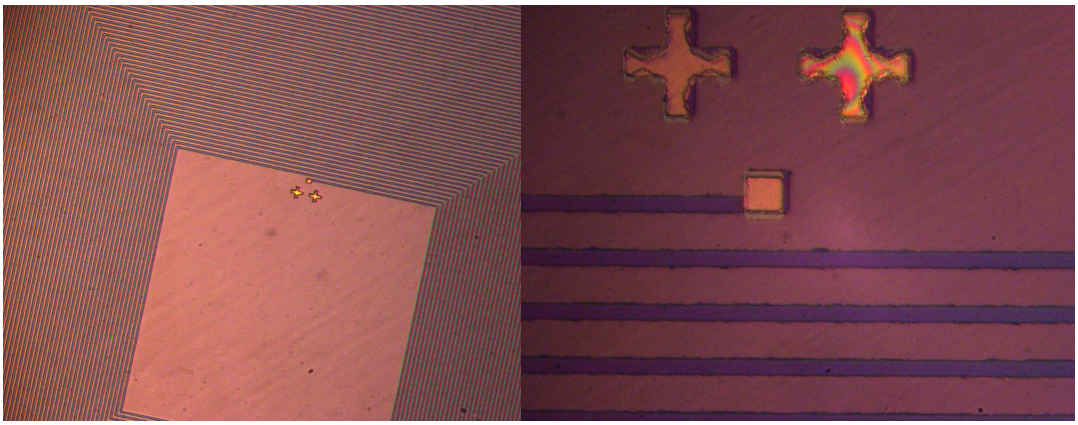

(a) (b)

Figure 5.16: (a) Microscope view after SiO_2 evaporation (4x zoom).
(b) The hole for the via and the left alignment cross are correctly opened, while the Newton rings in the right alignment cross indicate the presence of residual resist (40x zoom).

the substrate.
This issue is solved bombarding the substrate, before depositing the photoresist, with Ar^+ ions in the sputtering chamber. This expedient roughens

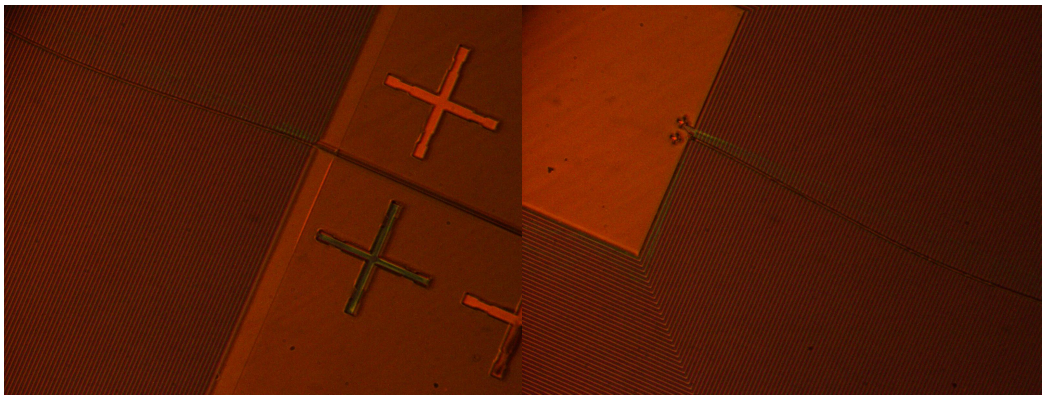

(a) (b)

Figure 5.17: Violin string effect, due to the incorrect rooting of the photoresist (4x zoom).

the surface of the SiO_2 substrate, favoring the rooting of the photoresist. In Figure 5.18 an example of successful washer lithography is shown.

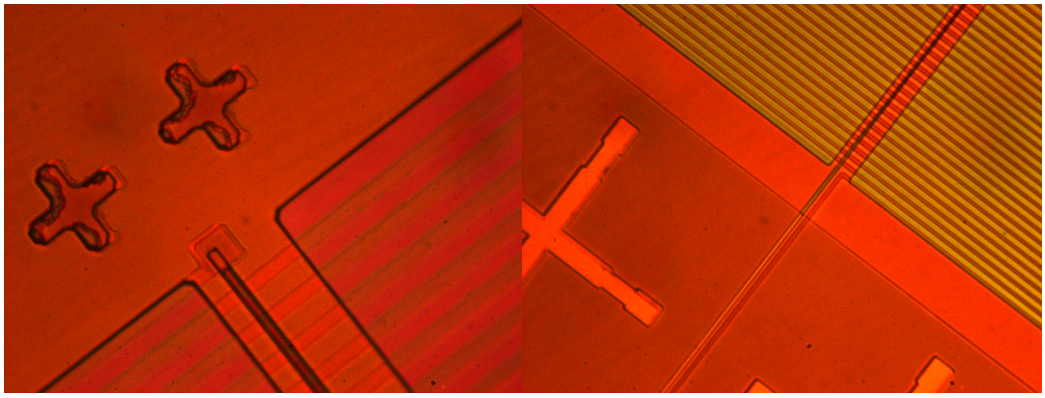

(a) (b)

Figure 5.18: (a) Microscope view of the washer photolithography (10x zoom). (b) Particular of the connection with the via (40x zoom).

Before proceeding with the Nb sputtering, a further cleansing of the substrate with Ar^+ ions bombardment is performed, to erase the superficial layers of Nb_2O_5 inside the via, formed with the bare exposition of the sample in the air. This is fundamental to avoid Superconductor-Dielectric-Superconductor

junctions in the spiral. Furthermore, a 10 nm sticking layer of Titanium is deposited on the SiO_2 before depositing Niobium, since Titanium shows a better rooting to SiO_2 than Niobium. A Nb layer is then deposited.

Wafer cut and cleaning Once the deposition processes are complete, the wafer is cut with a diamond-blade saw and cleaned in Acetone. The final result is shown in Figure 5.19.

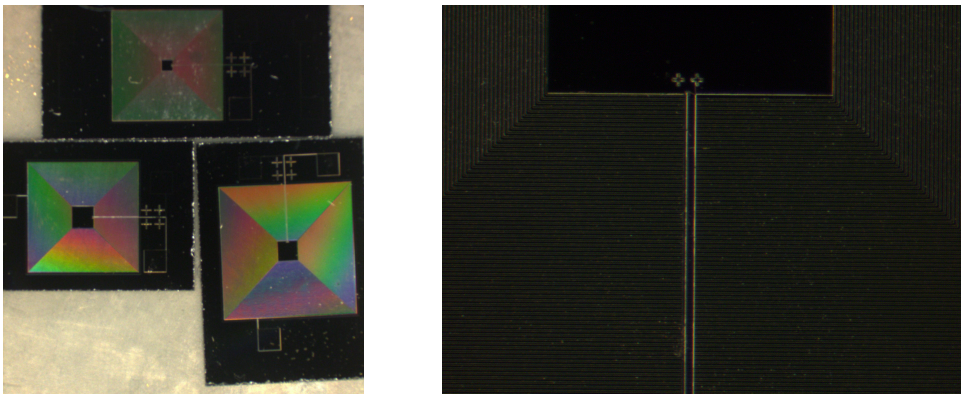

(a) (b)

Figure 5.19: (a) Ensemble view of the three different inductors designed after fabrication.
(b) Zoomed view (10x) of the 30 μH inductor, after the fabrication.

5.3 Capacitors

5.3.1 SMD capacitors

The frequencies of the sinusoidal biases which must be provided to the sensors range roughly from 100 KHz to 2 MHz. Considering inductances of 20-40 μH, this means that the capacitors must have capacitances varying about from 100 pF to 20 nF.

An ensemble of SMD capacitors have been selected and preliminary tested in liquid Nitrogen.
It is fundamental to know the behaviour with frequency and temperature of the capacitance, the dissipation factor (DF) and the equivalent series resistance (ESR). DF is defined as the ratio between ESR and |X|, where X is the imaginary part of the impedance.
The capacitors we selected mount a C0G/NP0 dielectric, which contains Neodymium, Samarium and other rare earth oxides. C0G/NP0 is classified as "Ultra Stable" dielectric, with negligible dependence of capacitance and dissipation factor with time, voltage, frequency and temperature. It is also known that, for C $\geq$ 50 pF (which is our case), DF $\lesssim$ 0.15% [46, 47]. For these reasons, C0G/NP0 seems suitable to our purpose.
A HP 4285A LRC Meter has been used to perform a 4-point test of the capacitors. In this way a direct measurement of the impedance Z and the phase angle θ is possible, allowing us to measure the parameters we are interested in, since:

$$C = -\lim_{\omega \to 0} \frac{1}{\omega X} \tag{5.10a}$$

$$ESR = |Z| cos\theta \tag{5.10b}$$

$$DF = \frac{cos\theta}{sin\theta} = cotan\theta = \tan\delta. \tag{5.10c}$$

where δ is the complementary angle of θ. The limit in the first equation means that the definition of C is valid until the inductive reactance is negligible with respect to the capacitive reactance:

$$\omega L \ll \frac{1}{\omega C}, \tag{5.11}$$

and in particular (see next subsection):

$$\frac{\omega L}{1/\omega C} \lesssim 10^{-3}. \tag{5.12}$$

Indeed, a parasitic inductive component is expected, mainly due to the coax cables used, the length of which is of the order of 2 m. The LCR Meter has a

Wire Correction function, which was used to take into account this parasitic inductance.

We tested Kemet and Multicomp C0G/NP0 0603 capacitors, with C ranging from 220 pF to 7.5 nF. The capacitors have been soldered on boards designed and printed for the test; SIL pins have been soldered on each board and used to connect to the coax cables and finally to the LCR Meter. The capacitors were measured first at room temperature and then dropped in a small Dewar bottle containing liquid Nytrogen. No breaks due to thermal shock were observed. As example, the results for the 1 nF and 7.5 nF capacitor are reported in Figures 5.20 and 5.21.

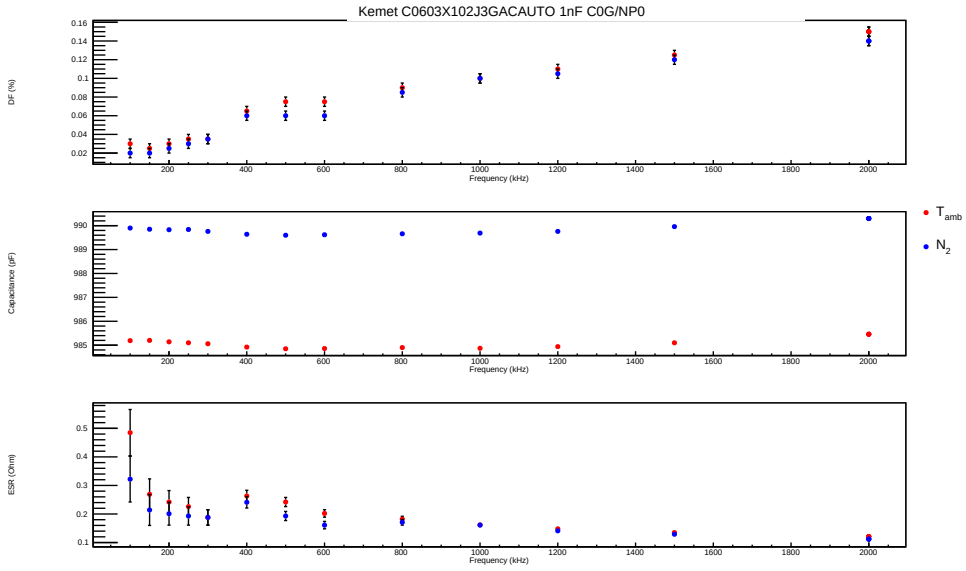

Figure 5.20: C, DF and ESR behaviour with frequency of a 1 nF capacitor, at room temperature and in liquid Nytrogen.

The last stable digit on the instrument screen is taken as the uncertainty on the C and DF data (error bars may not be visible because of the scale). From the definition of ESR it follows:

$$ESR = \frac{D}{\omega C}, \tag{5.13}$$

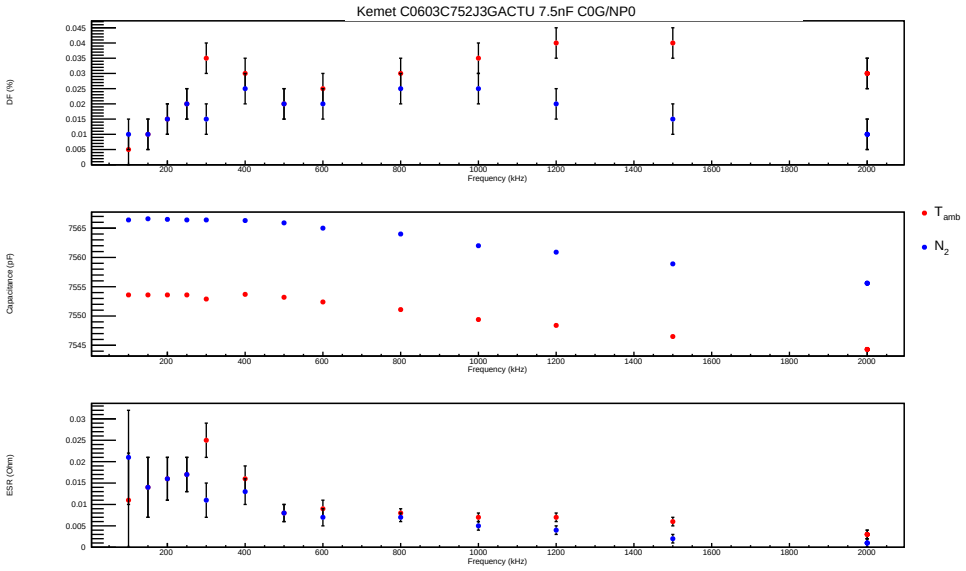

Figure 5.21: C, DF and ESR behaviour with frequency of a 7.5 nF capacitor, at room temperature and in liquid Nytrogen.

so that:

$$\sigma_{ESR}^2 = \left(\frac{\partial ESR}{\partial D}\right)^2 \sigma_D^2 + \left(\frac{\partial ESR}{\partial C}\right)^2 \sigma_C^2. \tag{5.14}$$

But since $\sigma_C \ll \sigma_D$, from the previous equations it follows that:

$$\frac{\sigma_{ESR}}{ESR} = \frac{\sigma_D}{D}. \tag{5.15}$$

This is how the error bars for ESR in Figures 5.20 and 5.21 are evaluated. However at low frequencies this is an underestimation of the error, because the current measured by the instrument is very small (order of μA). Due to shrinkage of the dieletric, there is a small increase in the capacitance at liquid Nitrogen temperature. At fixed temperature, the capacitance is with good approximation constant with frequency (fluctuations are of the order of 0.05 %), apart for the 7.5 nF capacitor, which exhibits a larger fluctuation ($\simeq$ 0.15 %) at high frequency. This larger variation is attributable to a stray parasitic inductance, due to precision limits of the Wire Correction function of the instrument (see next subsection).

The dissipation factors measured are in agreement with what reported in

literature, and the ESRs result to be smaller for greater capacitors (ESR $\sim$ 1 Ω for 220 pF, $\sim$ 0.1 Ω for 1 nF). Such ESR is desirable to minimize the dissipation of the resonators: considering a bias signal level of $\simeq$ 1 μV, the power dissipated by one capacitor is of the order of 0.1 pW, which is negligible with the expected $\sim$ 10 pW of the signal coming from the sky. Furthermore, a ESR of $\sim$ 0.1 Ω is within the requirement of being at least a factor 5.8 smaller than the operating resistance of the TES bolometer, which is $\sim$ 1 Ω.

5.3.2 Coax stray inductance

The inductance of a coax cable can be evaluated using the formula:

$$L_{coax}(\mu H) = 0.459\ log\left(\frac{D}{d}\right) l, \tag{5.16}$$

where D is the diameter of the outer conductor, d is the diameter of the inner conductor and l is the length of the cable in meters. Considering the dimensions of the cables used, we get $L_{coax} \simeq 1$ μH. A reasonable assumption is that the precision of the Wire Correction function of the instrument is of order of 0.1 %. Then:

$$L_{stray} = L_{coax} \times 10^{-3} \simeq 1 \text{ nH}. \tag{5.17}$$

The fluctuations on the capacitance due to a non-negligible inductive reactance must be comparable with the ratio of the inductive reactance and the capacitive reactance, hence the expected maximum fluctuation should be:

$$\Delta C|_{max} \simeq \frac{\omega L_{stray}}{1/\omega C}. \tag{5.18}$$

Considering L_{stray} = 1 nH, C = 7.5 nF and a frequency of 2 MHz, we get:

$$\Delta C|_{max} \simeq 0.12\ \%. \tag{5.19}$$

A cross-check was to find the self-resonance frequency, which is the frequency where the imaginary part of the impedance is closest to zero. A value of

roughly 22 MHz has been found; considering a C of 7.5 nF, it follows:

$$L = \frac{1}{\omega_0^2 C} = 0.7 \text{ nH}. \tag{5.20}$$

Hence, to have a negligible inductive reactance in testing capacitors, it must be:

$$\frac{\omega L}{1/\omega C} \lesssim 10^{-3}. \tag{5.21}$$

This explains the decrease of capacitance with the increasing of frequency observed for the 7.5 nF capacitor.

5.3.3 Interdigitated capacitors

An alternative to SMD capacitor would be photolithographing interdigitated capacitors in the same washer of the spiral inductors. This should reduce the ESR and the dissipation of the components, but the greatest limitation is the dimensions needed to obtain the desired capacitances. Preliminary simulations using SONNET have been performed: I designed a 1 pF unit, with dimensions of 1mm x 1mm, using 10 μm thick Cu lines and a 15 μm spacing. This 50 μm thick layer conductor is sandwitched between 2 layers of 500 μm SiO_2. It results from the simulation that the capacitance scales with the surface, so to obtain e.g. a 220pF capacitor an array of 15x15 such units is needed; for a 1 nF capacitor, an array of 30x30 is needed, and so on.

In Figure 5.22 the design of the unity of 1 pF is shown on the left; on the right the result of a simulation of a 2x2 array of such unit is shown (the red line refers to the resistance, the blue line to the capacitance).

5.4 Filters multiplexing

Multiplexing technology is essential for large arrays of bolometers. TES bolometers are usually cooled below 1 K. Individual wiring to each sensor,

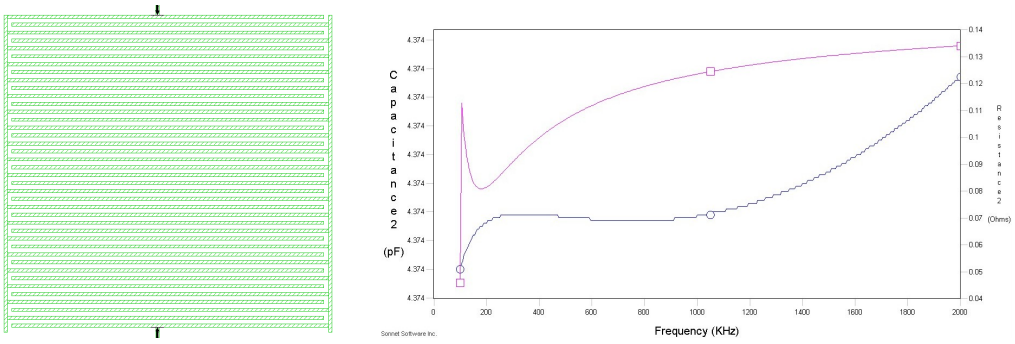

(a) (b)

Figure 5.22: SONNET design of an interdigitated capacitor and simulation result to determine its capacitance and resistance.

when dealing with hundreds of bolometers, is not a valuable option for cryogenic reasons, due to the huge heat load that so many wires would deliver. Not using multiplexing would also imply to use one SQUID for each sensor. SQUIDs though are very costly components, so the construction costs of the detector would drastically increase. Finally, the wiring that connects the 1K and 300K stages would also greatly grow, in terms of complexity and cost.
As already said, there are two techniques of multiplexing, TDM and FDM. Although they can be considered complementary, differences arise in real implementation of these systems [48]. In particular FDM, compared to TDM, allows a smaller noise contribution from the readout SQUID amplifier. Fig-

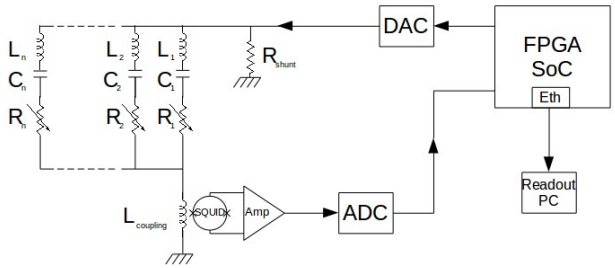

Figure 5.23: Schematic of a FDM readout multiplexer.

ure 5.23 shows the basic FDM circuit. Each detector in a set of N is biased with a sinusoidal bias at a unique frequency f_n, which typically range from

200kHz to 1-2MHz. A tuned filter consisting of a cold inductor and a cold capacitor is placed in series with each TES bolometer. The tuned filter has a double function: its bandwidth limits the current noise from the resistive TES bolometer and allows the N detectors to be biased with a single pair of wires: a comb of N bias frequencies is sent down this single pair. The tuned filter passes the appropriate bias carrier and suppresses the other $N-1$. The N sensors with their series filters are connected in parallel and the currents are summed and readout with a single SQUID. Warm demodulation electronics separate and recover the individual detector signals.

The number of detectors that can be multiplexed is defined by the readout bandwidth. For a FDM system this is determined by the closed-loop bandwidth of the readout SQUID amplifier. Currently these are of the order of 1-2MHz.

The readout noise comes from the Johnson noise from the TES detector and the readout SQUID amplifier. Johnson noise is limited in a FDM system by the cold tuned filter in series with the detector. The contribution from the readout SQUID amplifier is limited by the constant sampling of all the detectors, since only the small bandwidth around the detector bias frequency contributes to the readout noise. This is not true for the TDM system.

Regarding the power dissipation, at the coldest stage (< 1K) the power dissipated is very close to zero. At the SQUID stage (4K) the power dissipation is due to the readout SQUID biases, and amounts a few μW for a 1000 elements array. The main power dissipation is due to the current generation of sinusoidal bias carrier generation integrated circuits, in the hot stage outside of the cryostat.

One last thing worth noting is that the sinusoidal bias of the detectors in the FDM system is at a much higher frequency than any possible mechanical resonance or vibration in the receiver, telescope, balloon or satellite that houses the readout system. This makes in principle FDM extremely insensitive to mechanical perturbations.

5.5 Prototype tests

5.5.1 The cryogenic test facility

Resonant filters for FDM and SQUIDs operate at sub-K temperatures. To reach these cryogenic temperatures, we used a pulse-tube cryo-cooler. A cryogenic environment can be obtained using liquid cryogens (such as liquid Nytrogen or Helium) or mechanical cryo-coolers. In general, the latter are preferable to the former for experimental studies requiring temperatures below 4 K because of better reliability, cost and cooling power, however cryo-coolers have significant drawbacks, such as electromagnetic noise, mechanical vibration and temperature fluctuations inherent to cryo-coolers. These effects have especially relevance on sensitive measurements, like tests with SQUIDs. The pulse-tube cryocooler (PTC) has the advantage of having no moving parts inside the cold head, since the compression and expansion cycles of the Helium gas to produce cooling are not achieved by a mechanical piston but by using acoustic pulses.

The pulse tube we used is a Sumitomo SRP-082B2-F70H. The acoustic pulses are induced by a valve unit switching between two lines of Helium, one at 5 atm and one at 20 atm. Since this valve generates electromagnetic noise, it is separated from the refrigerator, as shown in Figure 5.24.

The refrigerator has two stages: a first cold head (first stage) nominally reaching 35 K with a cooling power of 40 W and a second stage nominally reaching 4 K with a cooling power of 0.9 W, shown in Figure 5.25. For these preliminary tests we could not reach sub-K temperatures, due to the lack of the two additional ^{3}He-^{4}He stages needed to reach ~ 350 mK. A temperature of $3 \div 4$ K however is enough to verify the operation of the SQUID and of the filters, since the nominal transition temperature of Niobium is ~ 9 K.

The two cold heads are hosted in a custom cryostat. The outer room temperature shell is a steel vacuum chamber (Figure 5.26), capable of reaching and maintaining a vacuum of P $\sim 10^{-7}$ mbar. This vacuum is achieved using a rotative pump to go down to P $< 10^{-3}$ mbar and, subsequently, a turbo-

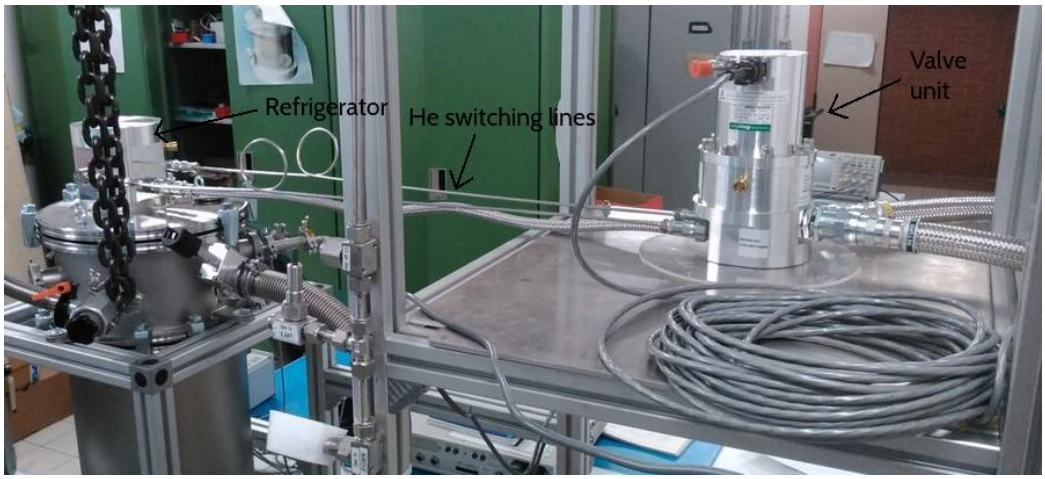

Figure 5.24: Large view of the pulse-tube cryocooler, showing the valve unit and the refrigerator unit.

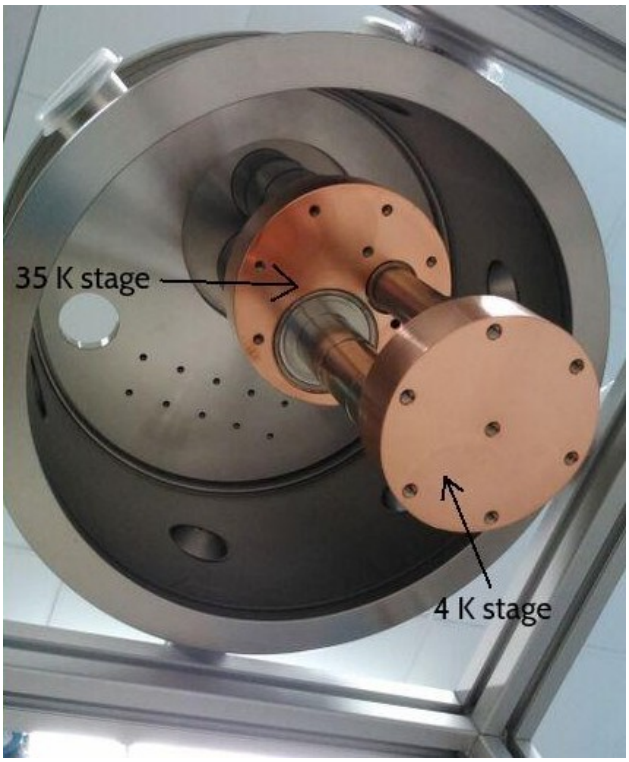

Figure 5.25: Bottom view of the inside of the cryostat.

molecular pump to reach P $\sim 10^{-5}$ mbar. At this point cooling is activated and cold heads act as cryogenic vacuum pumps, further increasing the vacuum level.

Figure 5.26: Outer view of the cryostat.

The first stage of the PTC is used to cool an intermediate 35 K stage, using a large copper plate, acting as a thermal break between room temperature and 4 K stage. To reduce emissivity and radiative loading, a cylindrical gold-plated copper radiation shield is suspended below the 35 K stage and encloses the 4 K stage. Moreover, a layer of Super-Insulation shield envelopes the radiation shield (Figures 5.27).

The second stage is the last and main stage of the PTC, reaching a nomi-

(a) (b) (c)

Figure 5.27: Disposition of the radiation shield and Super-Insulation, enveloping the 4 K stage.

nal temperature of 4 K, constituted of a copper plate, smaller than the first stage's one. We observed that, with no heat load applied, a temperature of ∼1.9 K was achieved. With a SQUID and a resonant filter mounted on it, we could reach a temperature of ∼2.5 K in a few hours (Figure 5.28). However, the time required for the first stage to reach its nominal temperature is higher (∼ 4 hours), so we assume that thermalisation of the load applied and the 4 K stage occurs not before this time. To monitor the temperature, we mounted a PT100 sensor on the radiation shield and a Si diode on the second stage (Figure 5.29). The PT100 is a thermoresistence, i.e. a temperature sensor which exploits the variation of the resistivity of the material with temperature; PT100s are commonly used to read temperatures in cryogenic environments down to ∼ 30 K.

The operation of a Si diode (silicon bandgap temperature sensor) instead, is based on the fact that the forward voltage of the diode is temperature-dependent, and this dependency is very well known. Si diodes are used to

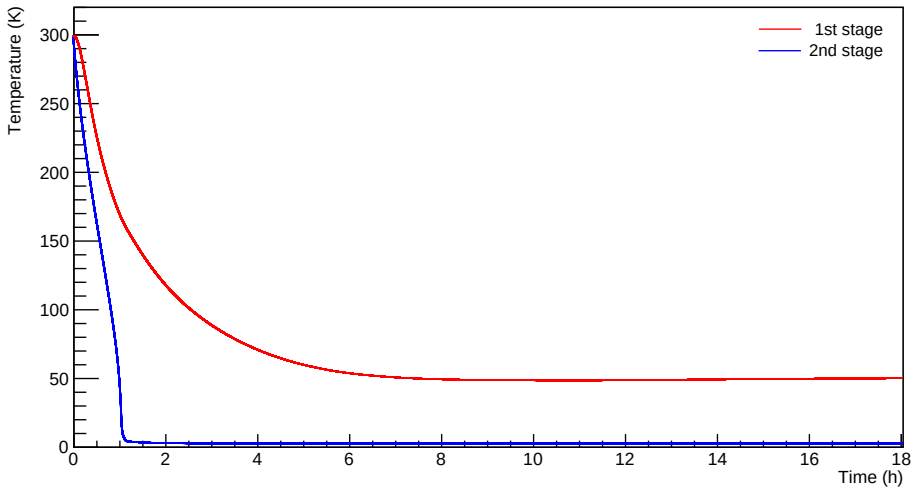

Figure 5.28: Cooling performance of the pulse-tube cryocooler. The PT100 sensor is attached to the first stage, the Si diode to the second stage.

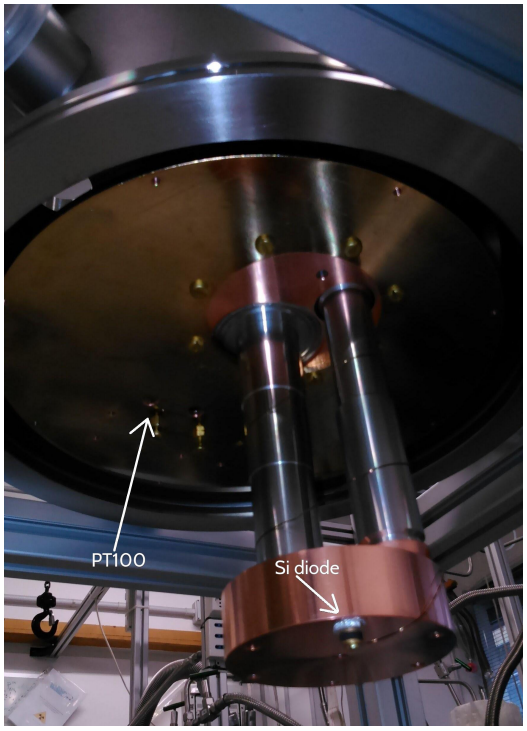

Figure 5.29: Disposition of the temperature sensors inside the cryostat.

monitor temperatures down to $\sim$ 1 K.
The sensors pass through the radiation shield and are connected to a custom flange. The outputs are connected to a Lakeshore Model 350 temperature controller, which allows to monitor at the same time the temperature read by both sensors.

5.5.2 Preliminary results

The optimization of the production of the spiral inductors have been very time consuming and required several steps of trial and failures to find the correct parameters to be used during the processes of photolithography and sputtering. This effort ultimately brought to the capability of producing spiral inductors with very good success percentage. As an example of the remarkable spatial precision obtainable, in Figures 5.30 and 5.31 a finalized spiral inductor I realized at NEST is shown.
As a preliminary test, I fabricated a square slit washer and used it as test structure in the cryogenic test facility of the INFN Laboratories of Pisa, to see its superconducting transition. As can be seen from Figure 5.32, the washer has been mounted to a Copper plate with vacuum grease and then micro-bonded to Copper soldering pads, disposed for a four-point measurement. A brass box was shaped and mounted above the Copper plate to reduce the thermal input to the washer due to thermal irradiation. The Copper plate was attached to the 4 K stage of our cryocooler (Figure 5.25); the wires were made to pass through the radiation shield and connected to the flange shown in Figure 5.26. The four-point monitoring of the resistance was realized connecting a HP 34401A multimeter to the flange. The full scale of the instrument was set such that the current applied to the device was 5 μA, in order to avoid to exceed the critical current of the washer and preventing it from becoming superconducting. At room temperature, the washer presented a resistance of $\simeq$ 7.8 Ω. The superconducting transition occurred at $R \simeq$ 8.9 K, as shown in Figure 5.33. The nominal Niobium

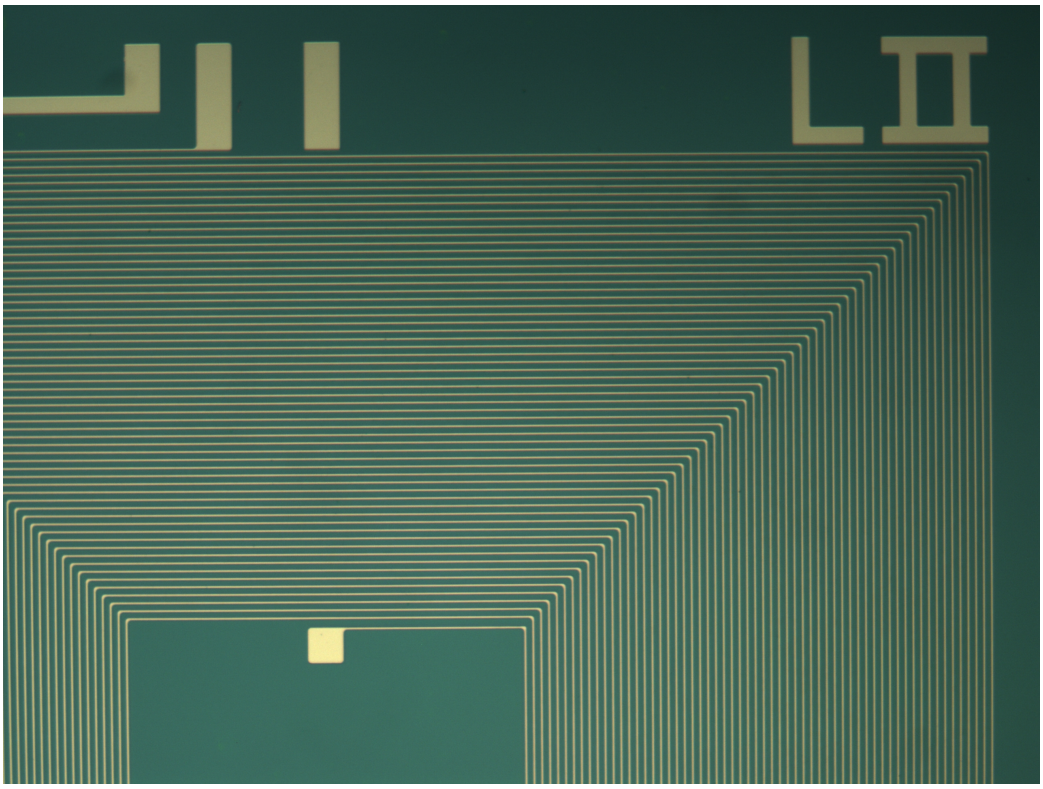

Figure 5.30: Microscope view of a spiral inductor, zoom 5x. The green regions are the SiO_2 of the wafer, the light brown regions are the Niobium tracks of the inductor.

critical temperature is 9.2 K [49]. The difference with our measured value may lie in the fact that our was a thin film ($\sim$ 100 μm) and/or a sub-optimal thermal contact of the sensor with the Copper plate. Subsequently, on the same Copper plate two inductors I realized at NEST have been mounted, as shown in Figure 5.32, to measure their superconducting transition and their inductance.

The experimental setup is currently being optimized to perform the characterization of single inductors and a test of multiplexing with two or more spiral inductors.

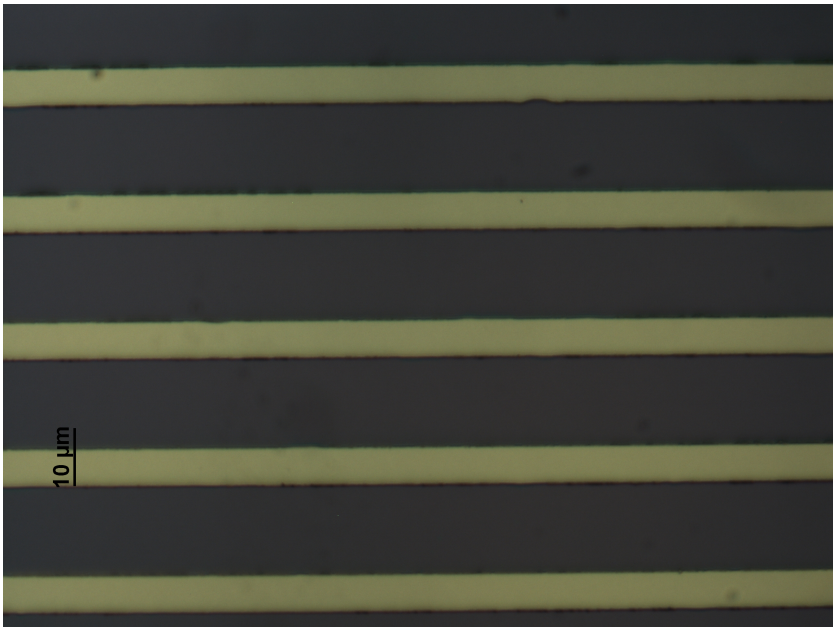

Figure 5.31: Microscope view of a spiral inductor, zoom 100x. The purple regions are the SiO_2 of the wafer, the light brown regions are the Niobium tracks of the inductor.

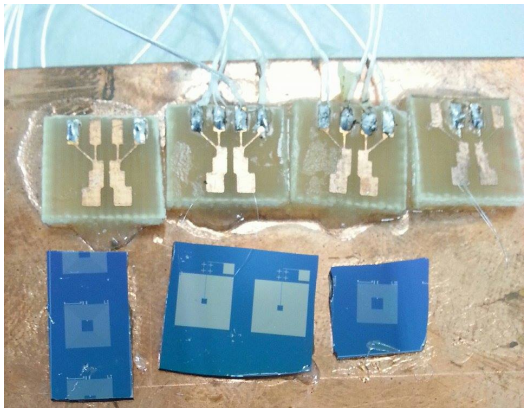

Figure 5.32: Two spiral inductors and one test structure (square slit washer) mounted on a Copper plate used for a preliminary test.

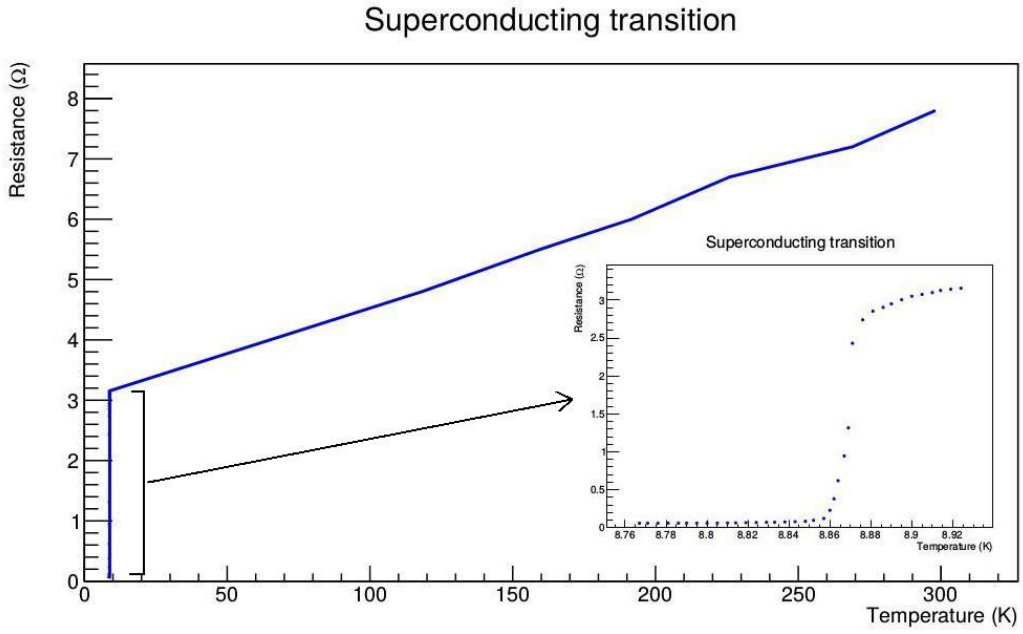

Figure 5.33: Behaviour of the resistance as a function of the temperature of the test structure (square slit washer). The inlet shows the detail of the superconducting transition curve.

Chapter 6

SQUIDs

Superconducting QUantum Interference Devices (SQUIDs) are the most sensitive detectors of magnetic flux currently available and this property can be used to make them excellent current sensors. Their principle of operation is based on magnetic flux quantization in a closed superconducting loop [50] ($\Phi_0 = h/2e \simeq 2.07 \cdot 10^{-15} Tm^2$ is the flux quantum) and tunnelling through a thin Josephson junction [51]. There are two kinds of SQUIDs. The first one is the dc SQUID [50], which consists of two Josephson junctions connected in parallel in a superconducting loop, operated by a stedy current bias. The second one is the rf SQUID [50], which involves a single Josephson junction interrupting the current flow around a superconducting loop, and is operated with a radiofrequency flux bias. In both cases, the output from the SQUID is periodic with period Φ_0 in the magnetic flux applied to the loop. Flux changes of order $10^{-6}\Phi_0$ are usually detectable [52].
Magnetic flux Φ quantization arises from the fact that the Cooper pairs in a superconductor can be described with one macroscopic wave function:

$$\psi(\vec{r}, t) = |\psi(\vec{r}, t)| e^{i\phi(\vec{r},t)} \tag{6.1}$$

with a well-defined phase $\phi(\vec{r}, t)$. In a closed superconducting loop, since the macroscopic wave function must be single-valued, the phase evolves of a

factor $2\pi n$ per turn. It can be shown [50] that this leads to the condition:

$$\Phi = n\Phi_0 \tag{6.2}$$

where Φ is the magnetic flux trapped in the loop and n is an integer.
A Josephson junction consists of two superconductors separated by a thin insulating barrier. Its operation is based on the fact that Cooper pairs are able to tunnel through the barrier, maintaining phase coherence in the process. The applied current I to the junction controls the difference $\delta = \phi_2 - \phi_1$ between the phases of the waveform in the two superconductors according to the current-phase relation:

$$I = I_c \sin \delta, \tag{6.3}$$

where I_c is the critical current, i.e. the maximum supercurrent the junction can sustain. When the current is increased from zero, initially there is no voltage across the junction, but for $I > I_c$ a voltage V appears, according to the voltage-frequency relation [50]:

$$\dot{\delta} = \frac{2eV}{\hbar} = \frac{2\pi V}{\Phi_0}. \tag{6.4}$$

6.1 DC SQUID

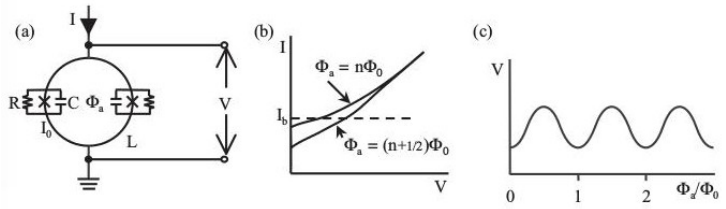

Figure 6.1: (a) The DC SQUID; (b) I-V characteristics; (c) V vs Φ/Φ_0 at constant bias current I. [50]

To perform the readout of the sensors, we will use dc SQUIDs. Figure 6.1 shows the fundamentals of a DC SQUID. Two Josephson junctions are connected in parallel on a superconducting loop of inductance L. If we bias

the SQUID with a constant current ($> 2I_c$), the voltage across the SQUID oscillates with period Φ_0 as we steadily increase Φ_a, as shown in Figure 6.1(c). The SQUID produces an output voltage δV in response to a small input flux $\delta\Phi$:

$$\delta V = V_\Phi \delta\Phi, \tag{6.5}$$

with $\delta\Phi \ll \Phi_0$. The point of operation of the SQUID is generally chosen on the steep part of the $V - \Phi$ curve, where the transfer coefficient:

$$V_\Phi \equiv \left|\frac{\partial V}{\partial \Phi}\right|_I \tag{6.6}$$

is maximum. The SQUID is then effectively a flux-to-voltage transducer. If an applied flux is provided through a current circulating in a coil coupled with the loop, the SQUID can be used as a transimpedance amplifier, i.e. converts a current to a voltage.

To give a simple description of how the DC SQUID works, we assume that the two junctions are identical and arranged symmetrically on the loop. In the absence of any applied flux (or in general with $\Phi_a = n\Phi_0$), there is no current circulating around the loop and the bias current divides equally between the two junctions. The measured critical current is $2I_c$. If we apply a magnetic flux Φ_a (or if $\Phi_a/\Phi_0 \neq n$), the flux in the loop will be quantized and will generate a current $J = -\Phi/L$ (Figure 6.2). This current adds to the bias

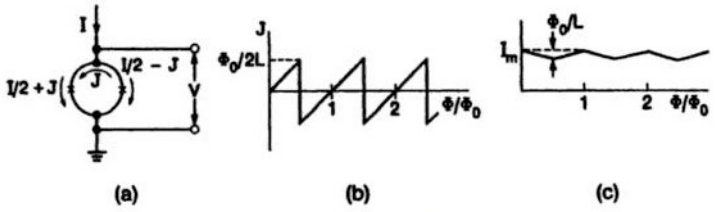

Figure 6.2: (a) A magnetic flux Φ generates a circulating current J that is periodic in Φ as shown in (b); as a result (c), the maximum supercurrent I_m is also periodic in Φ. [53]

current flowing through junction 1 and subtracts from that flowing through junction 2. In this simplicistic picture, the critical current in junction 1

is reached when $I/2 + L = I_c$, and in junction 2 flows a current $I_c - 2J$. The SQUID then switches to voltage state when $I = 2I_c - 2J$. As Φ_a is increased to $\Phi_0/2$, J increases to $\Phi_0/2L$ and the effective critical current falls to $2I_c - \Phi_0/L$. As the flux is increased beyond $\Phi_0/2$ the SQUID makes the transition from flux state $n = 0$ to $n = 1$, and J changes sign, flowing in opposite verse in the loop. As we increase Φ_a to Φ_0, J is reduced to zero and the effective critical current is restored to its maximum value $I_m = 2I_c$. In this way the critical current oscillates as a function of Φ. Since the voltage signal read from the SQUID is:

$$V = RI_c = \frac{RI}{2} + R|J|, \tag{6.7}$$

also V varies as a function of Φ_a with period Φ_0, as shown in Figure 6.1c. The voltage change across the SQUID is then $\Delta V = RJ = \Phi_0 R/2L$, where $R/2$ is the parallel resistance of the two shunts. Hence $V_\Phi = R/L$: to obtain high transfer coefficients it is important to produce SQUIDs with very low L.

The equivalent flux noise of the SQUID can be estimated considering a noise voltage across the SQUID $V_N(t)$ with a spectral density $S_V(\nu)$. The corresponding flux noise referred to the SQUID loop is:

$$S_\Phi(\nu) = \frac{S_V(\nu)}{V_\Phi^2}. \tag{6.8}$$

Flux noise is often characterized in terms of noise energy per unit bandwidth:

$$\varepsilon(\nu) = \frac{S_\Phi(\nu)}{2L}. \tag{6.9}$$

Assuming that the noise in the SQUID is dominated by the Johnson noise in the shunt resistors, we find $\varepsilon(\nu) = k_B T L/R$. We see that to have low $\varepsilon(\nu)$ we must choose T and L as low as possible and R as high as possible.

In practice, DC SQUIDs are made from thin films using photolitography or electron-beam litography techniques. To efficiently couple the input coil to the SQUID, Jaycox and Ketchen [43] introduced the idea of depositing a spiral input coil on a SQUID in a square washer configuration, separating

them with an insulating layer (see Figure 6.3). Typically, L is fractions of nH and R is of the order of Ohm.

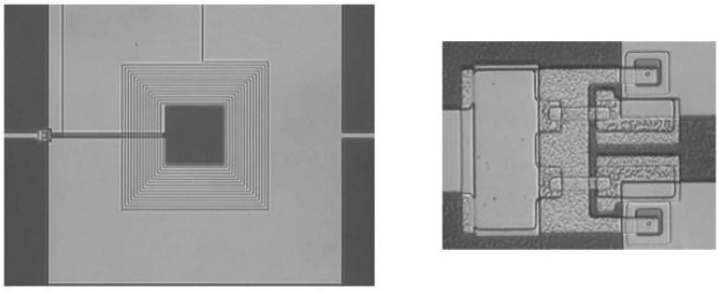

Figure 6.3: (a) Square-washer dc SQUID with overlaid 15-turn input coil. (b) Expanded view of the left-hand end of the slit showing the junction on each side of the slit, and the resistive shunts. [50]

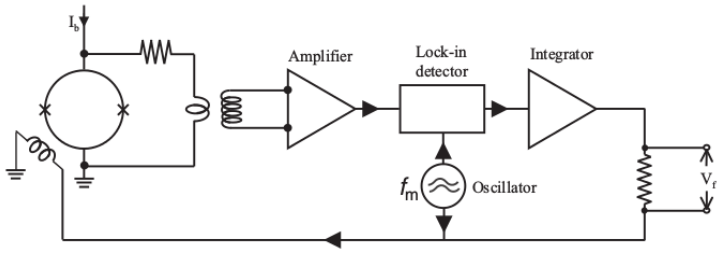

Figure 6.4: Flux modulation and feedback circuit for the dc SQUID. [50]

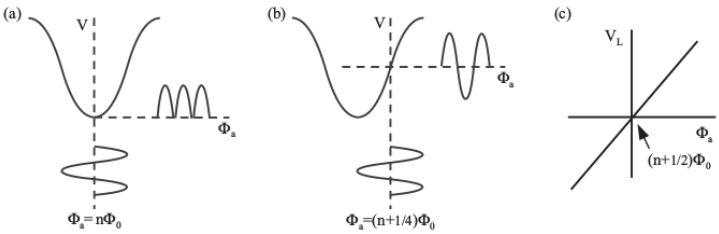

Figure 6.5: Flux modulation scheme showing voltage across the SQUID for (a) $\Phi = n\Phi_0$ and (b) $\Phi = (n + 1/4)\Phi_0$. (c) shows the output from the lock-in detector vs Φ. [50]

SQUIDs are generally used as null detectors of magnectic flux, in a flux-locked loop feedback circuit (FLL) as shown in Figure 6.4. A modulating flux is applied to the SQUID with a peak-to-peak amplitude $\Phi_0/2$ and a frequency f_m (usually ranging from 100 KHz to 10 MHz). If the flux in the SQUID is $n\Phi_0$ the output voltage is a rectified sine wave, as shown in Figure 6.5a. When this voltage is connected to a lock-in detector referenced to f_m , the output is zero. On the other hand, when the flux is $(n + 1/4)\Phi_0$ (Figure 6.4b), the output from the lock-in is maximum. Thus, as one increases the flux from $n\Phi_0$ to $(n + 1/4)\Phi_0$, the output from the lock-in steadily increases; if instead we decrease the flux from $n\Phi_0$ to $(n - 1/4)\Phi_0$, the output from the lock-in is negative (Figure 6.5c). After integration, the signal from the lock-in is coupled, via a resistor, to the same coil as that producing the flux modulation. In this way, if we apply a flux $\delta\Phi$ to the SQUID, the feedback circuit generates an opposing flux $-\delta\Phi$ to maintain a constant flux in the SQUID, producing a voltage V proportional to $\delta\Phi$ across the resistor. This technique allows to measure changes in flux with a sensibility of $10^{-6}\Phi_0$ [50].

6.2 SQUID test

In our cryogenic facility, already described in Chapter 5, we tested a CE1 blue dc SQUID by Supracon [54]. In Figure 6.6 the SQUID capsule and microchip and the circuit diagram of the SQUID chip is shown. In Figure 6.7 the main technical parameters of the SQUID are reported.
To perform the test, the SQUID capsule has been screwed to the 4 K stage of the cold head, using a C-shaped Copper plate, and further shielded from external magnetic fields using a μ-metal cylinder. Since its cooling is mainly provided by the cables, the outer insulating sheath of the SQUID cable has been removed in two points, and the inner cables have been wrapped around two brass screws, one at the 30 K stage and one at the 4 K stage, to improve the thermal contact (see Figure 6.8). The SQUID cable was then soldered to a dedicated 10-pins connector, which emerged out of the cryostat through a

(a) SQUID chip and Niobium shield.

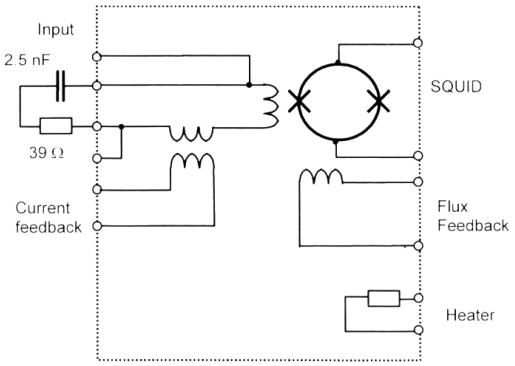

(b) Circuit diagram of the SQUID chip.

Figure 6.6

Parameter (open input coil)	Value
Chip size	2.5 mm × 2.5 mm
Working temperature	1...5 K
SQUID-Inductance L_S	≈ 180 pH
Input coil inductance L_{IN}	≈ 160 nH
Input coil – to – SQUID mutual inductance M_{IN}	4.8 nH
Input coupling $1/M_{IN}$	0.44 μA/Φ_0
Flux feedback coil – to – SQUID mutual inductance	80 pH
Flux feedback coupling	26 μA/Φ_0
Current feedback coil – to – input coil mutual inductance	4.2 nH
Current feedback coupling with short on the input coil	18 μA/Φ_0

Figure 6.7: Main technical parameters of the CE1 Blue SQUID.

custom flange.

With this configuration, the Si-sensor put on a copper plate on the 4 K stage went down to a temperature of 2.5 K in roughly 3 hours. The transition of the SQUID was checked by measuring the resistance between the flux feedback coil pins using a tester. At room temperature the nominal value is 0.81 kΩ. After the transition, we observed a resistance drop down to below 1 Ω.

6.2.1 V-Φ characteristic

To observe the V-Φ characteristic (Figure 6.1c), we applied a triangle wave to the flux feedback coil of the chip, through the SQUID electronics box, with

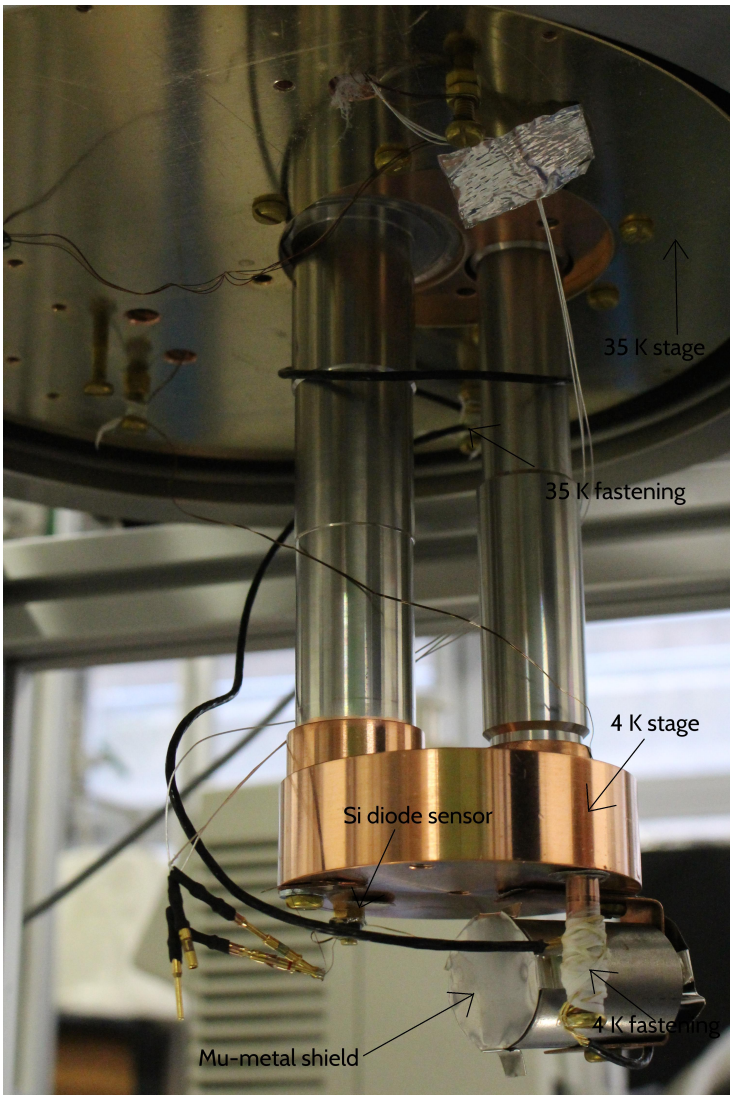

Figure 6.8: Setup for the SQUID test.

an amplitude of 1.5 V. The flux feedback coil turned this voltage into an external magnetic flux applied to the SQUID superconducting ring, so that varying the voltage corresponds to varying the range of Φ/Φ_0 probed. We observed that, for this SQUID and this readout electronics, one flux quantum Φ_0 corresponds to an applied voltage of roughly 600 mV. This correlation can only be made a posteriori, since we do not know exactly how the factory readout electronics manipulates the applied signal before supplying it to the

coil coupled with the SQUID.

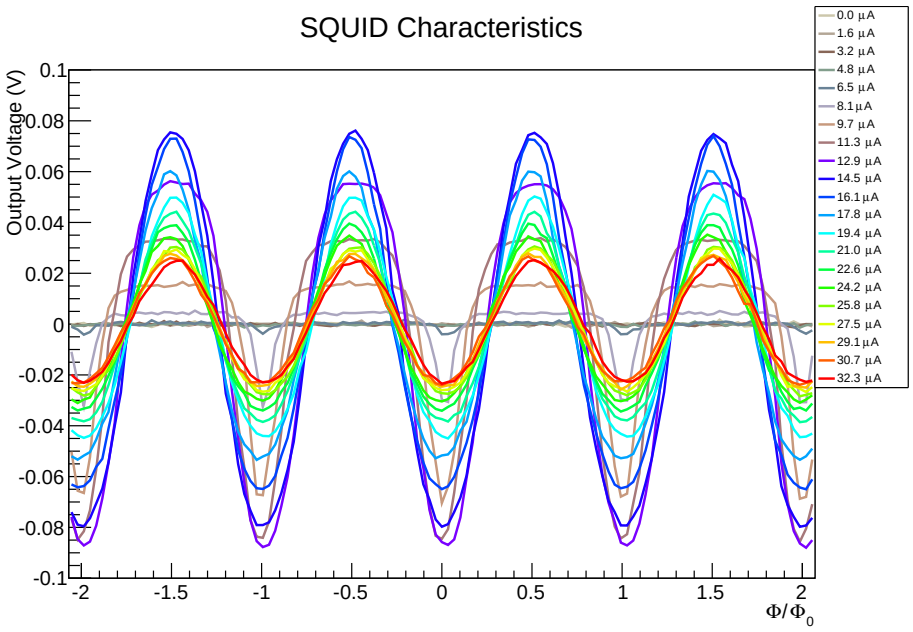

Figure 6.9: V-Φ characteristic of the SQUID. Each curve corresponds to a different bias current.

The triangle wave and the output voltage of the SQUID were then sent to two different channels of a digital oscilloscope, plotting the output voltage on the y-axis and the triangle wave on the x-axis. The oscilloscope coupling was set to AC, so that each constant contribute to the output voltage was removed, thus making it oscillate around zero (Figure 6.9). We repeated the measure for 21 bias currents, from 0 μA to 32.3 μA, in steps of roughly 1.6 μA. The results are plotted in Figure 6.10. From the period of oscillation, one can deduce the voltage value corresponding to one flux quantum, which in this case resulted to be $\simeq 0.58$ V. Figures 6.9 and 6.10 x-axis are renormalized to the ratio Φ/Φ_0.

6.2.2 V-I characteristic

We performed the same kind of measurement, applying 1 V to the flux feedback coil and setting the oscilloscope coupling to DC, so that the constant

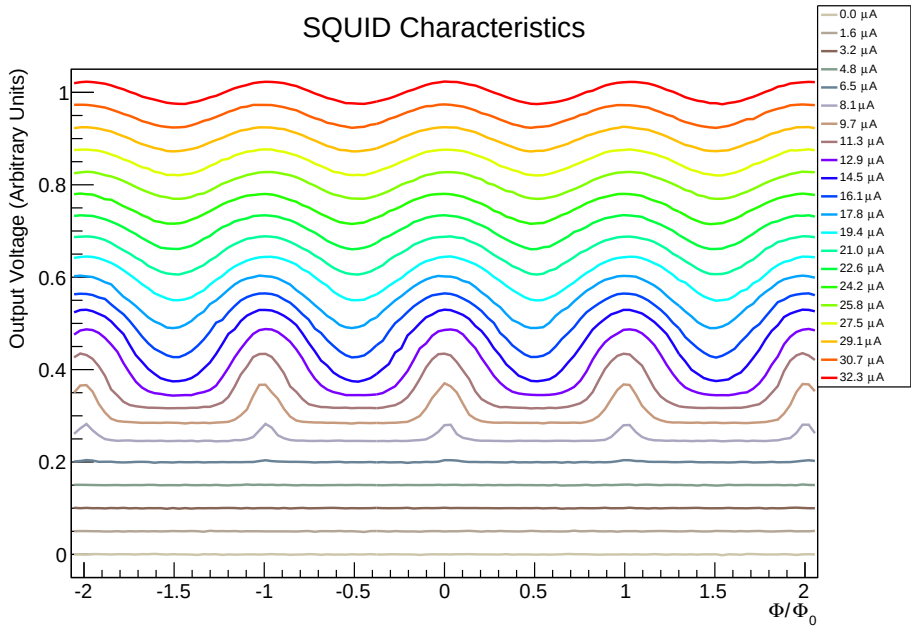

Figure 6.10: V-Φ characteristic of the SQUID. A constant on the ordinate axis has been added to each curve, so that they are more clearly visible.

contributes to the voltage output were maintained, to observe the V-I characteristic (Figure 6.1b).

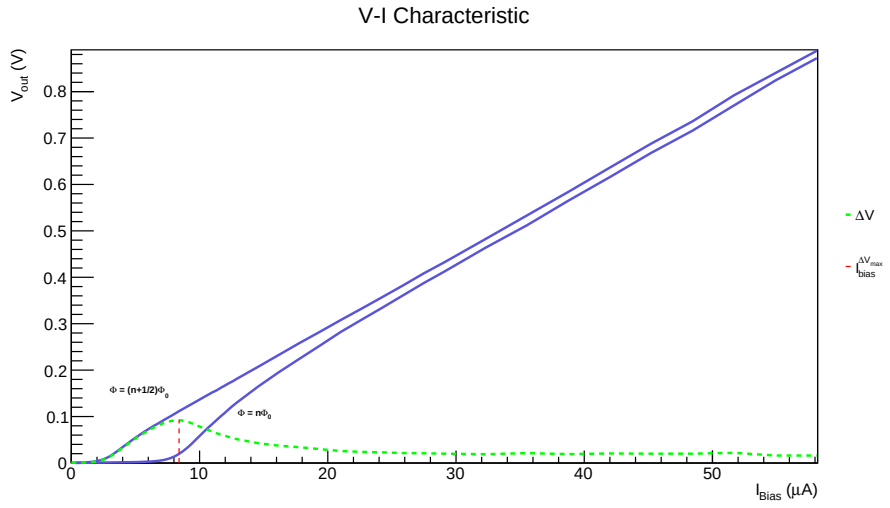

Figure 6.11: Measured V-I characteristic.

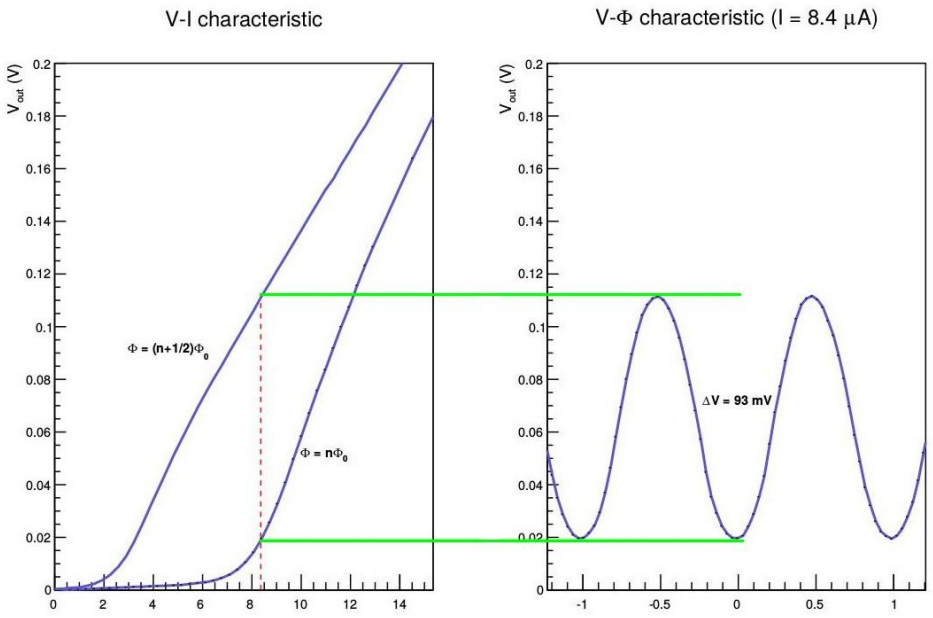

Figure 6.12: Correspondence between the measured V-I characteristic and the V-Φ characteristic with maximum amplitude.

The results are reported in Figures 6.11 and 6.12. The green dashed line is the subtraction of the two blue lines, i.e. the amplitude of the SQUID response. In correspondence of its maximum (red vertical dashed line) there is the V-Φ characteristic with maximum amplitude.
The operating point for the SQUID hence is chosen finding the current $I_{bias}^{\Delta V_{max}}$ corresponding to the maximum oscillation ΔV_{max} in output voltage, then applying an external magnetic flux $\Phi_a = (n + 1/4)\Phi_0$ such that the transfer coefficient $V_\Phi \equiv \left|\frac{\partial V}{\partial \Phi}\right|_{I_{bias}^{\Delta V_{max}}}$ is maximum. This operating point is the one exploited to amplify the multiplexed signal of the sensors.
From the V-Φ characteristic of Figure 6.12 we can measure the transimpedance of the SQUID, defined as:

$$G = \left(\frac{1}{M}\right)^{-1} \frac{\partial V}{\partial \Phi}, \tag{6.10}$$

where $\frac{1}{M}$ is the coupling to the SQUID coil expressed in $\mu A/\Phi_0$ units, as in Figure 6.7. Measuring the derivative of the V-Φ characteristic in $\Phi/\Phi_0 = 0.25$ (where it has a maximum), we found a transimpedance of ~ 191 V/A.

This value is comparable with typical values reported in literature [55, 56]. Further tests to characterize the flux noise are currently being performed.

Chapter 7

Conclusions

A detection of $B-$mode polarization in the CMB would be a smocking gun for inflation, giving a tremendous hint of the possible GUT energy scale. To perform such a delicate measurement, it is necessary to precisely evaluate the foregrounds (interstellar dust and galactic synchrotron) which contaminate the CMB polarization signal. The LSPE experiment has the goal of constrain the $B-$modes of CMB at large angular scales. The SWIPE instrument has the target of accurately measuring the polarization of the galactic dust foreground and of the CMB. The development of innovative techniques of detection, such the one described in this thesis, is fundamental to obtain such progresses in cosmology. Moreover, the success of the LSPE initiative would be a step towards a space-based experiment in the next future.
The SWIPE instrument will exploit an array of ~ 300 TES bolometers with a frequency-domain multiplexing readout.
TES bolometers are the most competitive CMB detector technology available. As I showed in Chapter 4, thanks to ETF they easily allow the measurement of temperature variations down to a level of 10^{-7} K, which correspond to a variation in the current output down to a level of 10^{-9} A. Furthermore, the spider-web geometry minimizes the interaction with cosmic rays, facilitating the task to remove such events from the data stream.
The readout of small current signals produced by the TESs is realized using

a SQUID, which amplifies the signal and converts it into a voltage signal. As I showed in Chapter 6, the choice of the operation point is made with the characterization of the V-Φ characteristic, choosing a value of bias current such that the amplitude of the voltage oscillations is maximum: the transimpedance is maximum for $\Phi = (n + 1/4)\Phi_0$, where is maximal the derivative of the voltage with respect to the applied magnetic flux. The measurement of the transimpedance of the SQUID I tested resulted in a value comparable with typical values reported in literature.

The noise contribution achieved with a single TES bolometer, operated at sub-Kelvin temperatures, is comparable to or less than the expected photon noise limit. To increase the noise performance and achieve the necessary sensitivity to detect such small cosmological signals, the sensors are multiplexed. Frequency domain multiplexing is obtained placing in series with each sensor a superconducting LC filter. In Chapter 5 I explained why the superconducting coil design for the inductor is chosen.

The R&D activity pursued to design and fabricate such devices exploited photolithography and sputtering processes. Such research activities, aimed at realizing devices for CMB detectors, are unique in Europe.

The process of production of superconducting inductors has been finalized and optimized, and the superconducting transition of a test structure has been observed. The experimental setup is currently being improved to perform the characterization of the inductors and a test of a multiplexed array of devices, whose results are expected in the next few weeks.

Appendices

Appendix A

Cosmology fundamentals

A.1 General relativity

For a geodesics in a generic gravitational field we can write:

$$\frac{d^2x^\mu}{d\tau^2} + \Gamma^\mu_{\sigma\rho}\frac{dx^\sigma}{d\tau}\frac{dx^\rho}{d\tau} = 0, \tag{A.1}$$

where

$$\Gamma^\mu_{\sigma\rho} = \frac{1}{2}g^{\mu\nu}\left(\frac{\partial g_{\sigma\nu}}{\partial x^\rho} + \frac{\partial g_{\rho\nu}}{\partial x^\sigma} - \frac{\partial g_{\sigma\rho}}{\partial x^\nu}\right) \tag{A.2}$$

is the metric connection (also known as Christoffel symbol), and $g^{\mu\nu}$ is the metric tensor, which in an inertial reference frame reduces to the Minkowski metric tensor. On scales for which the cosmological principle is valid, it is possible to treat galaxies as point particles, with coordinates $x^\mu = (t, \vec{x})$. We can choose a reference frame, said comoving, such that each x^μ does not change with time. What changes is a scale factor $a(t)$, which rescales the distances.

After some mathematical cunning it is possibile to obtain the Robertson-Walker metric:

$$ds^2 = dt^2 - a^2(t)\left(\frac{1}{1-kr^2}dr^2 + r^2 d\Omega^2\right) \tag{A.3}$$

which is derived using just the expansion of the universe and the isotropy and homogeneity postulated by the cosmological principle. (1.6) is obtained using

spherical coordinates, so that $d\Omega^2 = d\theta^2 + sin^2\theta d\phi^2$. k is a parameter which describes the space-time curvature. We can redefine the r coordinate so that the possible cases $k = 0,\ k > 0,\ k < 0$ reduce to $k = 0,\ k = 1,\ k = -1$: $k = 0$ means flat universe, $k = 1$ and $k = -1$ mean, respectively, open and closed universe.

The metric tensor for (1.6) is:

$$g^{\mu\nu} = \begin{bmatrix} 1 & 0 & 0 & 0 \\ 0 & -\frac{a^2}{1-kr^2} & 0 & 0 \\ 0 & 0 & -a^2r^2 & 0 \\ 0 & 0 & 0 & -a^2r^2sin^2\theta \end{bmatrix}. \tag{A.4}$$

It is then possible to calculate the metric connection using (1.5) and solve (1.4) for the geodesics of any point in the universe.

To take into account the energy and momentum of the material point, we define the energy-momentum tensor $T^{\mu\nu}$ as follows:

$$T^{\mu\nu} = (\rho + P)\, u^\mu u^\nu - g^{\mu\nu} P \tag{A.5a}$$

$$T^{\mu\nu}{}_{;\nu} = 0 \tag{A.5b}$$

where:

$$T^{\mu\nu}{}_{;\nu} = \frac{\partial T^{\mu\nu}}{\partial x^\mu} + \Gamma^\mu_{\alpha\nu} T^{\alpha\nu} + \Gamma^\nu_{\alpha\nu} T^{\mu\alpha} \tag{A.6}$$

is the partial covariant derivative of $T^{\mu\nu}$, u^μ is the 4-dimensional velocity and ρ and P are respectively energy density and pressure. This definition is valid in a generic reference frame and gravitational field.

Equation (1.8b) is the generalization in presence of a gravitational field of the energy and momentum conservation law. However, (1.8b) does not express any conservation law of physical quantities, because in a gravitational field what must be conserved is not the 4-momentum of matter only, but the 4-momentum of matter *and* gravitational field, which is not included in (1.8a). Landau and Lifshitz first derived in 1947 the expression of a quantity, $t^{\mu\nu}$, which added to $T^{\mu\nu}$ resulted in a conservative energy-momentum tensor for the gravitational field. $t^{\mu\nu}$ is a pseudotensor because it contains ordinary,

not covariant, derivatives; however it contains also Christoffel symbols, which behave like tensors under linear transformations of the coordinates. It follows that the 4-divergence of the sum $T^{\mu\nu} + t^{\mu\nu}$ is zero. $t^{\mu\nu}$ is derived solely from the metric tensor, it is symmetric under indices permutations and vanishes in a locally inertial reference frame (because it contains only first derivatives of the metric). These features ensure that $T^{\mu\nu} + t^{\mu\nu}$ is the correct energy-momentum tensor for the gravitational field.

The metric and the energy content of the universe are related by Einstein equations:

$$G_{\mu\nu} \equiv R_{\mu\nu} - \frac{1}{2} g_{\mu\nu} R = 8\pi G T_{\mu\nu}, \tag{A.7}$$

where $G_{\mu\nu}$ is the Einstein tensor, $R_{\mu\nu}$ is the Ricci tensor, R is the Ricci scalar, given by the contraction of the Ricci tensor ($R \equiv g^{\mu\nu} R_{\mu\nu}$), G is Newton's constant and $T_{\mu\nu}$ is the energy-momentum tensor. Note that the left side of (1.10) depends only on the metric, the right side only on the energy.

The Ricci tensor is expressed in terms of the metric connection:

$$R_{\mu\nu} = \Gamma^{\alpha}_{\ \mu\nu;\alpha} - \Gamma^{\alpha}_{\ \mu\alpha;\nu} + \Gamma^{\alpha}_{\ \beta\alpha}\Gamma^{\beta}_{\ \mu\nu} - \Gamma^{\alpha}_{\ \beta\nu}\Gamma^{\beta}_{\ \mu\alpha}. \tag{A.8}$$

Due to its tensorial nature, (1.10) is actually a system of 16 coupled, non-linear, partial differential equations; their number reduces to 10 because the $0i$ components are null, for the isotropy of the universe. The nonlinearity implies that the superposition principle is not valid for gravitational fields. This principle is valid only in the case of weak field, in which Einstein equations can be linear.

Einstein originally added a $\Lambda g_{\mu\nu}$ term to his equation; since Λ is a constant and the 4-divergence of the metric tensor is zero, this unaffected the conservation laws. The cosmological constant term was introduced to allow a stationary solution for the evolution of the universe. Hubble's observations of an expanding universe however made Einstein abandon the idea of a cosmological constant. Despite the reasons, there is nothing inconsistent in such a term in the equations, so Λ was considered to be zero until recent astronomical observations have found that a positive cosmological constant is needed

to explain the acceleration of the universe: this cosmological constant is now called *dark energy*. Adding the cosmological constant, Einstein equations become:

$$R^{\mu\nu} - \frac{1}{2}g^{\mu\nu}R = 8\pi G T^{\mu\nu} + \Lambda g^{\mu\nu}. \tag{A.9}$$

Expliciting $T^{\mu\nu}$ in the comoving reference frame, we can define a new energy-momentum tensor which accounts of the cosmological constant:

$$\widetilde{T}^{\mu\nu} = \begin{bmatrix} \rho + \frac{\Lambda}{8\pi G} & 0 & 0 & 0 \\ 0 & P - \frac{\Lambda}{8\pi G} & 0 & 0 \\ 0 & 0 & P - \frac{\Lambda}{8\pi G} & 0 \\ 0 & 0 & 0 & P - \frac{\Lambda}{8\pi G} \end{bmatrix} = \begin{bmatrix} \widetilde{\rho} & 0 & 0 & 0 \\ 0 & \widetilde{P} & 0 & 0 \\ 0 & 0 & \widetilde{P} & 0 \\ 0 & 0 & 0 & \widetilde{P} \end{bmatrix} \tag{A.10}$$

redefining energy density and pressure. Note that if Λ is positive, $\widetilde{\rho} > 0$ and $\widetilde{P} < 0$. From now on I omit for simplicity the tilde symbols.
The definition of the components of the energy-momentum tensor is:

$$T^{00} = \sum_n E_n \delta^3 \left(\vec{x} - \vec{x}_n(t)\right) = \rho(t) \tag{A.11a}$$

$$T^{0i} = \sum_n P_n^1 \delta^3 \left(\vec{x} - \vec{x}_n(t)\right) = 0 \tag{A.11b}$$

$$T^{ij} = \sum_n \frac{P_n^i P_n^j}{E_n} \delta^3 \left(\vec{x} - \vec{x}_n(t)\right) = P(t)\delta^{ij} \tag{A.11c}$$

From (1.14c) it follows that pressure can be written as:

$$P = \frac{T^{11} + T^{22} + T^{33}}{3} = \frac{1}{3}\sum_n \sum_{m=1}^{3} \frac{P_n^m P_n^m}{E_n} \delta^3 \left(\vec{x} - \vec{x}_n(t)\right) = \frac{1}{3}\frac{\vec{P}_n^2}{E_n} \delta^3 \left(\vec{x} - \vec{x}_n(t)\right) \tag{A.12}$$

There are 3 limit cases in which (1.15) simplifies:

- Radiation domination, in which matter is a relativistic fluid, so that $P_n \simeq E_n$ and (1.15) becomes:

$$P = \frac{1}{3}\rho; \tag{A.13}$$

- Matter domination, in which cold matter dominates and so (1.15) becomes:

$$P \simeq 0 \tag{A.14}$$

- Λ domination, in which as follows from (1.13):

$$P = -\rho \tag{A.15}$$

These 3 situations can be summarized writing:

$$P = \alpha\rho \qquad \text{with} \qquad \alpha = \begin{cases} 0, & \text{matter domination} \\ -1, & \Lambda \text{ domination} \\ \frac{1}{3}, & \text{radiation domination} \end{cases} . \tag{A.16}$$

A.2 Friedmann-Lemaitre equations

These equations can be obtained solving the 00 component of Einstein equations (solving the other components would lead to non-independent equations). After some lengthy calculations we obtain:

$$\frac{k}{a^2} + H^2(t) = \frac{8\pi G}{3}\rho + \frac{\Lambda}{3}. \tag{A.17}$$

It can be shown that this can be rewritten as:

$$\frac{\ddot{a}}{a} = -\frac{4}{3}\pi G(\rho + 3P). \tag{A.18}$$

Another useful equation is the continuity equation:

$$\frac{\partial\left(\rho a^3\right)}{\partial t} = -P\frac{\partial a^3}{\partial t} \tag{A.19}$$

which is obtained solving (1.8b) with $\mu = 0$. (1.20) and (1.22) are the fundamental equations which govern the evolution of the universe. Using (1.19) in (1.22) and solving we obtain:

$$\rho \propto a^{-3(1+\alpha)}. \tag{A.20}$$

This result allows us to evaluate how the energy density evolves with the scale factor.

Considering nonrelativistic particles (matter domination), we find $\rho a^3 = constant$. We would expect this, because the energy density of nonrelativistic particles is the rest mass energy times the number density; since the number density is inversely proportional to the (comoving) volume and the densities were necessarily larger when the scale factor was smaller, the energy density of matter should scale, as it does, as a^{-3}.

In case of radiation domination we get $\rho a^4 = constant$. This means that the energy density of CMB feels the effect of the expansion of the universe by a factor a^{-1}, so the increase of the scale factor causes a decrease of the energy density, i.e. of the temperature.

In Λ domination we simply get $\rho = constant$. These 3 different evolutions are summarized in Figure 1.3.

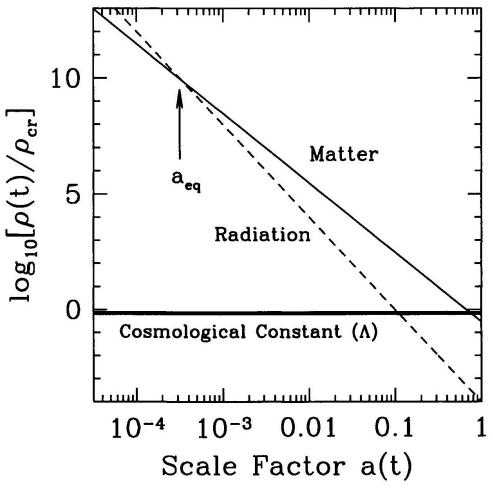

Figure A.1: Energy density vs scale factor for different constituents considering a flat universe. Energy density is expressed in critical density units. a_{eq} is the matter-radiation equality epoch. [4]

Solving (1.21) leads to solutions for the scale factor as a function of time: for matter domination we get $a(t) \propto t^{2/3}$; for radiation domination we get $a(t) \propto t^{1/2}$; for Λ domination we get $a(t) \propto e^{\sqrt{\Lambda/3}t}$. The evolution of $a(t)$ is

depicted in Figure 1.4.

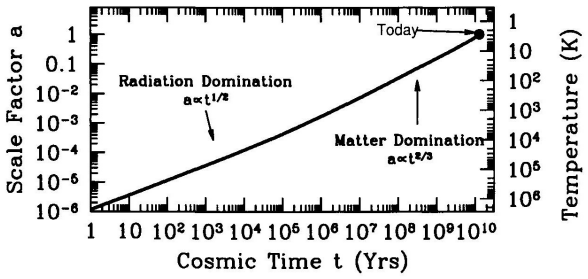

Figure A.2: Evolution of scale factor and temperature of the universe with time. [4]

The Friedmann-Lemaitre equation predicts therefore an exponential expansion of the scale factor if a positive cosmological constant dominates the energy density.

Let's now consider the most general case, without making assumptions on the energy domination. If r is the comoving distance, the physical distance d is at first order $d(t) \simeq a(t)r$, so we are allowed to write $v = \dot{d} = \dot{a}r = Hd$ and (1.20) becomes:

$$1 = \Omega_M + \Omega_k + \Omega_\Lambda, \tag{A.21}$$

where $\Omega_M = \rho/\rho_{crit}$, $\Omega_k = -k/a^2H^2$ and $\Omega_\Lambda = \Lambda/3H^2$. From (1.24) it follows that $\Omega_k = 1 - \Omega_M - \Omega_\Lambda$, that is the curvature of the universe is determined by the content of the cosmological constant (or dark energy) and by the matter (both ordinary and dark) and radiation content. ρ_{crit} is the critical density. A simple way do obtain the expression for ρ_{crit} is assuming Λ to be zero (that is, considering a classical, newtonian universe) and setting the normalised spatial curvature, k, equal to zero. Applying these substitutions in (1.20), we find:

$$\rho_{crit} = \frac{3H^2}{8\pi G}. \tag{A.22}$$

Using H_0, we find that today $\rho_{crit} \simeq 10^{-29} g/cm^3$, which corresponds roughly to 6 hydrogen atoms per cubic metre.

Appendix B

Slow roll inflation

For this brief introduction to inflationary theory we follow the arguments of D. Baumann, *The Physics of Inflation*, Subsection 1.4.
The fundamental condition for inflation is the decreasing of the Hubble radius:

$$\frac{d}{dt}(aH)^{-1} < 0. \tag{B.1}$$

After some mathematics, it can be shown [7] that (1.60) can be rewritten as:

$$\varepsilon = -\frac{\dot{H}}{H^2} = -\frac{d\ln H}{dN} < 1, \tag{B.2}$$

where dN measures the number of e-folds N of inflationary expansion. (1.61) implies that, to have inflation, the fractional change of the Hubble parameter per e-fold must be small. Since we want inflation to last for about 60 e-folds of expansion, this requires ε to remain small for a sufficiently large number of Hubble times. Defining:

$$\kappa = \frac{\dot{\varepsilon}}{H\varepsilon} = \frac{d\ln\varepsilon}{dN} \tag{B.3}$$

this condition is expressed requiring $|\kappa| \ll 1$. In inflationary theories, this parameter is often written as η, but here I used a different letter to avoid confusion with the conformal time.
The first theory of inflation was proposed by Guth in 1980 [6]. He considered a universe dominated by the constant energy density of a metastable false

vacuum. This leads to an exponentially expanding de Sitter space with $H = const$, i.e. $\varepsilon = \kappa = 0$. However, classicaly, false vacuum inflation never ends: quantum-mechanical tunnelling from the false vacuum to the true vacuum ends inflation locally, but the post-inflationary universe looks nothing like ours [7].

One of the simplest models which solves the false vacuum problem is the *slow roll inflation*. This model uses a scalar field ϕ, the *inflaton*, minimally coupled to Einstein gravity, whose action is:

$$S = \int d^4x\sqrt{-g}\left[\frac{M_{pl}^2}{2}R - \frac{1}{2}g^{\mu\nu}\partial_\mu\phi\partial_\nu\phi - V(\phi)\right], \tag{B.4}$$

where R is the Ricci scalar and $V(\phi)$ is so far an arbitrary function, shown in Figure 1.11.

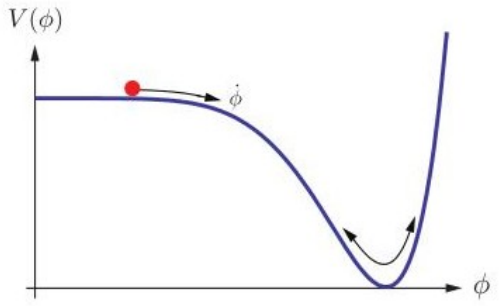

Figure B.1: Potential energy of the inflaton. [7]

The time evolution of $\phi(t)$ is governed by the Klein-Gordon equation:

$$\ddot{\phi} + 3H\dot{\phi} + V' = 0. \tag{B.5}$$

Here the Hubble constant H has in this case the role of a friction parameter, and is given by the Friedmann equation:

$$H^2 = \frac{1}{3M_{pl}^2}\left[\frac{1}{2}\dot{\phi}^2 + V\right]. \tag{B.6}$$

From (1.64) and (1.65) we derive:

$$\dot{H} = -\frac{1}{2}\frac{\dot{\phi}^2}{M_{pl}^2}. \tag{B.7}$$

So in this model ε becomes:

$$\varepsilon = \frac{\frac{1}{2}\dot{\phi}^2}{M_{pl}^2 H^2} = \frac{\frac{1}{2}\dot{\phi}^2}{\frac{1}{3}\left(\frac{1}{2}\dot{\phi}^2 + V\right)}. \tag{B.8}$$

Hence the condition $\varepsilon < 1$ occurs if the potential energy, V, dominates over the kinetic energy, $\frac{1}{2}\dot{\phi}^2$. For this condition to persist the acceleration of the scalar field has to be small. To assess this it is useful to define the dimensionless acceleration per Hubble time:

$$\delta = -\frac{\ddot{\phi}}{H\dot{\phi}}. \tag{B.9}$$

Using (1.62) we find:

$$\kappa = 2(\varepsilon - \delta). \tag{B.10}$$

Therefore, the conditions for inflation to happen and to sufficiently persist are ε and $|\delta|$ to be much smaller than unity, so that $\{\varepsilon, |\kappa|\} \ll 1$. These conditions can be used to simplify the equation of motion (*slow roll approximation*). It can be demonstrated that under this approximation, ε and κ (*slow roll parameters*) become:

$$\epsilon_V = \frac{M_{pl}^2}{2}\left(\frac{V'}{V}\right)^2 \quad \text{and} \quad |\kappa_V| = M_{pl}^2 \frac{|V''|}{V}. \tag{B.11}$$

The amount of inflation is measured by the number of e-folds of accelerated expansion:

$$N = \int_{a_i}^{a_f} d\ln a = \int_{t_i}^{t_f} H(t)dt, \tag{B.12}$$

where t_i and t_f are defined as the times when $\varepsilon(t_i) = \varepsilon(t_f) = 1$. In the slow roll approximation, (1.71) can be rewritten as:

$$N = \int_{\phi_i}^{\phi_f} \frac{d\phi}{M_{pl}\sqrt{2\epsilon_V}}, \tag{B.13}$$

where ϕ_i and ϕ_f are defined as the boundaries of the interval where $\epsilon_V < 1$. The anisotropies on largest scale observed in the CMB are produced at about 60 e-folds before the end of inflation:

$$N_{CMB} = \int_{\phi_{CMB}}^{\phi_f} \frac{d\phi}{M_{pl}\sqrt{2\epsilon_V}} \simeq 60. \tag{B.14}$$

A successful solution to the horizon problem requires at least N_{CMB} e-folds of inflation. Knowing this, and specifying a model for $V(\phi)$ (a simple example is a term of the type $m^2\phi^2$), one can deduce the energy scale of the inflaton field.

Appendix C

Inductor production receipts

In this appendix I report the receipts I optimized for the production of the spiral inductors.

C.1 INFN Section of Genoa

Spiral

- MicroResist ma-N 405 spin coating for 30 sec at 1500 rpm.
- Soft-baking at 95°C for 90 sec.
- Exposure with MJB4 mask aligner with 4 cycles of 1 sec.
- Development in ma-D 331S for 70 sec.
- Cleaning in Oxygen plasma (optional).
- Niobium sputtering, deposition rate 30 nm/min, thickness deposited $\sim$ 200 nm.
- Lift-off in Acetone.

Via

- MicroResist ma-N 440 spin coating for 30 sec at 1500 rpm.
- Soft-baking at 95°C for 90 sec.
- Exposure with MJB4 mask aligner with 4 cycles of 1 sec.
- Development in ma-D 331S for 70 sec.
- Cleaning in Oxygen plasma (optional).
- SiO_2 evaporation, deposition rate 1 nm/sec, thickness deposited $\sim$ 400 nm.
- Lift-off in Acetone.

Washer

- MicroResist ma-N 440 spin coating for 30 sec at 1500 rpm.
- Soft-baking at 95°C for 90 sec.
- Exposure with MJB4 mask aligner with 4 cycles of 1 sec.
- Development in ma-D 331S for 70 sec.
- Cleaning in Oxygen plasma (optional).
- Via cleaning through ion gun.
- Ti sticking layer deposition, thickness deposited $\sim$ 10 nm.
- Niobium sputtering, deposition rate 30 nm/min, thickness deposited $\sim$ 600 nm.
- Lift-off in Acetone.

C.2 NEST

Spiral

- AllResist AR-N 4340 spin coating for 5 sec at 500 rpm, then for 60 sec at 6000 rpm.
- Soft-baking at 90°C for 60 sec.
- Exposure with MJB4 mask aligner with 1 cycle of 10 sec.
- Post-baking at 95°C for 120 sec.
- Development in AR 300 475 for 70 sec.
- Cleaning in Oxygen plasma (optional).
- Niobium sputtering, deposition rate 30 nm/min, thickness deposited $\sim$ 150 nm.
- Lift-off in Acetone.

Acknowledgements

First of all, my deepest gratitude and thanks are for my supervisor Alessandro Baldini, who has always been present to guide me, assist me, teach me and correct my errors, with patience and attention from the beginning of my work to the very end of it.
I am as well profoundly thankful to Giovanni Signorelli, for his essential sustain and inevitable funniness which accompanied me with during my work.
My thanks also go to all the people of LSPE Collaboration: Carlo Bemporad, Fabrizio Cei, Luca Galli, Giovanni Gallucci (our laboratory discussion have been fantastically illuminating), Marco Incagli, Marco Grassi, Donato Nicoló , Franco Spinella and Marco Venturini. Each and everyone of you during this year helped me sharing with me his own knowledge and experience, and for this I am grateful. I owe gratitude also to the people of the High Technology division of INFN - Section of Pisa, for their helpfulness and assistance.
I would also like to thank: Pasqualantonio Pingue, Francesco Giazotto, Giorgio de Simoni, Franco Carillo, Elia Strambini, Daniele Ercolani, Antonio Fornieri and Stefano Guiducci of the National Enterprise for nanoScience and nanoTechnology for their assistance during my work at NEST; Flavio Gatti, Dario Corsini and Michele Biasotti of INFN - Section of Genoa, for their help and advices on the fabrication of inductors; Paolo de Bernardis of University of Rome - La Sapienza for his explanations on the simulated CMB data I used for the TES simulation.
To my companions of the graduand room Adele, Marco C., Marco M. and Milene, to my colleagues and most of all dear friends Andrea and Francesco,

to all my friends in Pisa and Messina (you are too many to name!): just simply thanks for being there and for tolerating my awful character. You are the best and I couldn't wish for a better company.
And finally, last but sure as hell not least, my greatest and profoundest thanks are for my parents and all my family. I wouldn't be here if it weren't for you, and if I was able of going on and biting the bullet when things were hard to reach the finish line, it was just because of you.
To those who are here no more
Wherever, whatever now you are,
This is also dedicated to you, for
your memory is unharmed and pure.

Bibliography

[1] A. McKellar. Molecular lines from the lowest states of diatomic molecules composed of atoms probably present in interstellar space. *Publications of the Dominion Astrophysical Observatory (Victoria, BC)*, 7, 1941.

[2] A.A. Penzias and W. Wilson. A measurement of excess antenna temperature at 4080 mc/s. *Astrophysical Journal*, 142:419–421, 1965.

[3] J. C. Mather et al. Measurement of the cosmic microwave background spectrum by the cobe firas instrument. *Astrophysical Journal Part 1*, 420:439–444, 1994.

[4] J. Delabrouille et al. The pre-launch planck sky model: a model of sky emission at submillimetre to centimetre wavelengths. *arXiv:1207.3675*, 2012.

[5] W.H. McMaster. Polarization and the Stokes parameters. *American Journal of Physics*, 22, 1954.

[6] W. Hu et al. Benchmark parameters for cmb polarization experiments. *Physical Review D*, 67, 2003.

[7] S. Lee et al. Voltage-biased superconducting transition-edge bolometer with strong electrothermal feedback operated at 370 mK. *Applied Optics*, 37:3391–3397, 1998.

[8] P. L. Richards. Bolometers for infrared and millimeter waves. *Journal of Applied Physics*, 76, 1994.

[9] T. Lanting. Multiplexed readout of superconducting bolometers for cosmological observations. *Ph.D. thesis*, 2006.

[10] A. Lee. Squid readout multiplexers for transition-edge sensor arrays. *Nuclear Instruments and Methods in Physics Research A*, 559:786–789, 2006.

[11] P. de Bernardis et al. The large-scale polarization explorer (LSPE). *arXiv:1208.0281*, 2012.

[12] R. Adam et al. Planck 2015 results. I. Overview of products and scientific results. *arXiv:1502.01582*, 2015.

[13] E. Hubble. A relation between distance and radial velocity among extra-galactic nebulae. *Proceedings of the National Academy of Science*, 15:168–173, 1929.

[14] Stompor et al. Cosmological implications of the MAXIMA-1 high resolution cosmic microwave background anisotropy measurement. *The Astrophysical Journal*, 561, 2001.

[15] D. N. Spergel et al. Wilkinson microwave anisotropy probe (WMAP) three year results: implications for cosmology. *Astrophysical Journal Supplement*, 170:337–408, 2007.

[16] S. Dodelson. *Modern Cosmology*. Academic Press, 2003.

[17] A. Guth. Inflationary universe: a possible solution to the horizon and flatness problems. *Physical Review D*, 23:347–356, 1981.

[18] D. Baumann. The physics of inflation.

[19] U. Seljak and M. Zaldarriaga. A line-of-sight integration approach to cosmic microwave background anisotropies. *Astrophysics Journal*, 469:437–444, 1996.

[20] R.K. Sachs and A.M. Wolfe. Perturbations of a cosmological model and angular variations of the microwave background. *Astrophysical Journal*, 147, 1967.

[21] R.H. Becker et al. Evidence for reionization at z $\sim$ 6: detection of a Gunn-Peterson trough in a z = 6.28 quasar. *arXiv:astro-ph/0108097*, 2001.

[22] F. Cao et al. Quantum slow-roll and quantum fast-roll inflationary initial conditions: CMB quadrupole suppression and further effects on the low cmb multipoles. *Physical Review D*, 78, 2008.

[23] N. Rajguru et al. CMB observations from the CBI and VSA: a comparison of coincident maps and parameter estimation methods. *Monthly Notices of the Royal Astronomical Society*, 363:1125–1135, 2005.

[24] S.L. Glashow H. Georgi. Unity of all elementary particle forces. *Physical Review Letters*, 32:438–441, 1974.

[25] S. Raby. Grand unified theories. In *arXiv:hep-ph/0608183*, 2008.

[26] N.W. Boggess et al. The COBE mission: its design and performance two years after the launch. *Astrophysical Journal*, 397, 1992.

[27] P. de Bernardis et al. Maps of the millimitre sky from the BOOMERanG experiment. *arXiv:astro-ph/0311396*, 2003.

[28] E.M. Leitch et al. Measuring polarization with DASI. *Nature*, 420:763–771, 2002.

[29] C.L. Bennett et al. The microwave anisotropy probe (MAP) mission. *Astrophysics Journal*, 583, 2003.

[30] P.A.R. Ade et al. Planck 2015 results. XIII. Cosmological parameters. *arXiv:1502.01582*, 2015.

[31] S. Prunet and A. Lazarian. Polarized foreground from thermal dust emission. *arXiv:astro-ph/9902314*, 1999.

[32] M.V. Sazhin et al. Galactic synchrotron foreground and the CMB polarization measurements. *arXiv:astro-ph/0209400*, 2002.

[33] R.W. Aikin et al. BICEP2 I: Detection of B-mode polarization at degree angular scales. *Physical Review Letters*, 112, 2014.

[34] R. Adam et al. Planck intermediate results. XXX. The angular power spectrum of polarized dust emission at intemediate and high galactic latitudes. *arXiv:1409.5738*, 2014.

[35] B. P. Crill. SPIDER: A balloon-borne large-scale CMB polarimeter. *arXiv:0807.1548*, 2008.

[36] P. de Bernardis et al. SWIPE: a bolometric polarimeter for the Large-Scale Polarization Explorer. *arXiv:1208.0282*, 2012.

[37] L. Jones. *Handbook of optics*, chapter 18. Reflective and catadioptric objectives. McGraw-Hill, 1978.

[38] A. Lee et al. A superconducting bolometer with strong electrothermal feedback operated at 370 mk. *Applied Physics Letters*, 69:1801–1803, 1996.

[39] T.M. Lanting. *Multiplexed readout of superconducting bolometers for cosmological observations*. PhD thesis, University of California, Berkeley, 2003.

[40] G.A. Bazilevskaya et al. On the stratospheric measurement of cosmic rays, 1998.

[41] K.D. Irwin and G.C. Hilton. *Cryogenic particle detection*, volume 99, chapter Transition-Edge Sensors, pages 63–149. Springer-Verlag, 2005.

[42] W. Meissner and R. Ochsenfeld. Ein neuer Effekt bei Eintritt der Supraleitfähigkeit. *Naturwissenschaften*, 21, 1933.

[43] J.M. Jaycox and M.B. Ketchen. Planar coupling scheme for ultra low noise dc SQUIDs. *IEEE Transactions on Magnetics*, 17:400–403, 1981.

[44] http://www.sonnetsoftware.com/.

[45] ma-N 400 and ma-N 440 - Negative Tone Photoresists data sheet.

[46] /www.radiant.su/files/images/syfer/dielectric˙information.pdf.

[47] /www.avx.com/docs/catalogs/cc0g.pdf.

[48] A. Lee. SQUID readout multiplexers for transition-edge sensor arrays. *Nuclear instruments and methods in physics research A*, 559:786–789, 2006.

[49] M. Peiniger and H. Piel. A superconducting Nb_3Sn coated multicell accelerating cavity. *Nuclear science*, 32, 1985.

[50] J. Clarke and A. I. Braginski. *The SQUID handbook, Vol. I.* WILEY-VCH, 2004.

[51] B.D. Josephson. Possible new effects in superconductive tunnelling. *Physics Letters*, 1, 1962.

[52] R. Kleiner et al. Superconducting quantum interference devices: State of the art and applications. *Proceeding of the IEEE*, 92, 2004.

[53] H. Weinstock. *SQUID sensors: Fundamentals, Fabrication and applications*. Springer, 1996.

[54] http://www.supracon.com/en/ce1blue.html.

[55] T. M. Lanting et al. Linearized SQUID array for high bandwidth frequency-domain readout multiplexing. *arXiv:astro-ph/0901:1919*, 2009.

[56] M. A. Dobbs et al. Frequency multiplexed superconducting quantum interference device readout of large bolometer arrays for cosmic microwave background measurements. *Review of scientific instruments*, 83, 2012.

Cast a cold eye
On life, on death.
Horseman, pass by!

William B. Yeats